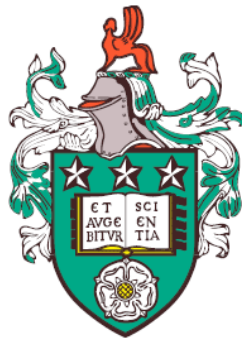


# Extrinsic spin-orbit scattering in thin films



Amy Louise Westerman  
School of Physics and Astronomy  
University of Leeds

Submitted in accordance with the requirements for the degree of

*Doctor of Philosophy*

August 2021

This thesis is dedicated to my parents, for everything  
and  
in loving memory of Phyllis, Dennis, Pauline, Brian and Jim.

## **Intellectual Property Statement**

The candidate confirms that the work submitted is her own, except where work which has formed part of jointly authored publications has been included. The contribution of the candidate and the other authors to this work has been explicitly indicated below. The candidate confirms that appropriate credit has been given within the thesis where reference has been made to the work of others.

This copy has been supplied on the understanding that it is copyright material and that no quotation from the thesis may be published without proper acknowledgement.

The right of Amy Louise Westerman to be identified as Author of this work has been asserted by her in accordance with the Copyright, Designs and Patents Act 1988.

©2021 The University of Leeds and Amy Louise Westerman.

Exceptional support was provided by Prof. Bryan J. Hickey for the calculations and fitting of both the electron-electron interaction and quantum interference effects to the resistivity data as a function of temperature.

## Acknowledgements

The preparation of this thesis could not have been completed without first being given the opportunity to carry out this work. I would like to thank Dr. David Williams, EPSRC and Hitachi Cambridge Laboratory for providing this opportunity and generous financial support. I wish to thank my supervisor, Prof. Bryan J. Hickey; from allowing me the opportunity to volunteer in the condensed matter group as an interested undergraduate, he has nurtured my interest in the field, provided extraordinary support and allowed me a great deal of independence, for which I am truly grateful. I am indebted to Dr. Mannan Ali not only for providing me with the experimental skills required for the preparation of this thesis, but also for his support over the past few years, from aid in building and fixing equipment, to providing advice and moral support. My heartfelt thanks go to Brian Gibbs, John Turton, Luke Bone, Dave Chapman and the late Philip Cale for going the extra mile to keep me in constant supply of cryogenics, and always with a smile. I also wish to thank Dr. Gavin Burnell for his tireless efforts to keep measurements running smoothly with constant revisions to the measurement code that keeps the group running. The group has been a pleasant place to work thanks to the group members, whom I wish to thank for providing such a supportive environment in which to work, and in particular my officemates Shoug, Jamie, Ris and Kowsar. I owe thanks to the many summer, BSc and MPhys students I have had the pleasure of working with, for their eagerness to learn and willingness to provide support has consistently inspired and motivated me; in particular, I'd like to thank Louise, Ben, Connor and Alistair for supporting me and my work as much as I supported them.

I have been privileged to have the support of my friends and family during the preparation of this thesis, to all of whom I owe a large debt of gratitude. In particular, I am very thankful to Ris for providing a great deal of moral support and a good deal of laughter in addition to remote experimental support. I wish to thank Ben for being a great support through difficult times. I am indebted to Shoug, Katharina, Fatma, Adam, Katie,

Wafa and Priya for being such good friends. I wish to thank Lucy for her kind and enthusiastic support along with Freddie, who could never fail to make me smile, and Elouise. I'm also incredibly grateful for the crucial personal support given to me by Gemma, Lisa, Jo, Bankole, Matthew, Helen and Aly which helped to see me through to the end of this PhD. The support, love and encouragement provided by many family members has been pivotal in preparing me to write this thesis; I am particularly indebted to those that didn't make it to see this thesis be submitted: Grandma Phyllis, Auntie Pauline, Grandad Dennis, Uncle Brian and Grandad Jim. I also owe thanks to Wilma and Leo for their support during the preparation of this thesis. Finally, I owe a huge debt of gratitude to my parents, Paul and Lynda Westerman, without whom this thesis could not have been completed; their support, patience, kindness and thoughtfulness has known no bounds, and I could never thank them enough.

## Abstract

Extrinsic spin-orbit scattering is a mechanism which can give rise to, and enhance, both the anomalous and spin Hall effects. In this thesis, it is shown that spin-dependent scattering from extrinsic impurities, localised as a discontinuous  $\delta$ -layer, significantly modifies the ordinary Hall coefficient of thin films of Cu. The position of the impurity  $\delta$ -layer profoundly impacts the magnitude of the Hall coefficient, giving rise to maximum values for positions between the edges and centre of the film consistently for Ir and Ta impurities. For an impurity  $\delta$ -layer of Fe situated between ultrathin Pt and the substrate, a paramagnetic spin Hall magnetoresistance (PSHMR) is discovered which strongly depends upon the concentration of the impurity, the temperature and the magnitude of the applied magnetic field. This has implications for measurements of the spin Hall magnetoresistance (SHMR) in bilayers of the ferrimagnetic insulator yttrium iron garnet ( $\text{Y}_3\text{Fe}_5\text{O}_{12}$ , YIG) and Pt, where the magnetic proximity effect (MPE) may play a role. To investigate this, YIG/Pt bilayers with various interfaces are prepared and magnetotransport phenomena studied. Through measurements of the resistivity as a function of temperature, the conventional magnetoresistance, the angle-dependent magnetoresistance and the Hall effect, it is shown that a strong dependence upon the interface exists. Etching the YIG surface with piranha solution is found to enhance the spin mixing conductance, giving rise to the spin Hall-anomalous Hall effect and a significant increase in the SHMR in comparison to a film without this treatment. An enhanced MPE is also found after the etching process, giving rise to a PSHMR and a Hall effect reflecting a larger concentration of magnetic impurities. Interface preparation methods hence need to be improved to observe a pure SHMR from an enhanced spin mixing conductance.

# CONTENTS

<b>1</b>	<b>Introduction</b>	<b>1</b>
<b>2</b>	<b>Background</b>	<b>5</b>
2.1	Introduction . . . . .	6
2.2	Thin film transport . . . . .	6
2.2.1	Magnetoresistance in thin films . . . . .	8
2.3	Extrinsic spin-orbit scattering . . . . .	9
2.4	The ordinary, anomalous and spin Hall effects . . . . .	13
2.4.1	The ordinary Hall effect . . . . .	13
2.4.1.1	The spin effect . . . . .	18
2.4.2	The anomalous Hall effect . . . . .	19
2.4.3	The spin Hall effect . . . . .	22
2.5	Spin Hall magnetoresistance . . . . .	24
2.6	Quantum interference . . . . .	27
2.6.1	Temperature dependence . . . . .	27
2.6.2	Field dependence . . . . .	32
2.7	Magnetic proximity effect . . . . .	34
2.8	The Kondo effect . . . . .	35
2.9	Magnetotransport in YIG/metal bilayers . . . . .	37
<b>3</b>	<b>Experimental methods</b>	<b>43</b>
3.1	Introduction . . . . .	44
3.2	Material fabrication . . . . .	44
3.2.1	Direct current magnetron sputtering . . . . .	44

3.2.2	Y <sub>3</sub> Fe <sub>5</sub> O <sub>12</sub> Preparation . . . . .	47
3.2.2.1	Radio frequency magnetron sputtering . . . . .	48
3.2.2.2	Annealing of YIG . . . . .	49
3.2.2.3	Etching of YIG . . . . .	50
3.3	Surface and structural characterisation . . . . .	51
3.3.1	X-ray reflectivity . . . . .	51
3.3.2	X-ray diffraction . . . . .	53
3.4	Vibrating sample magnetometry . . . . .	55
3.5	Low temperature electron transport . . . . .	56
3.5.1	Electrical measurements . . . . .	58
3.5.2	Magnetoresistance measurements . . . . .	60
3.5.3	Hall effect measurements . . . . .	62
<b>4</b>	<b>Non-magnetic impurity delta layers in the Hall effect</b>	<b>65</b>
4.1	Introduction . . . . .	66
4.2	Transport properties of Cu thin films . . . . .	66
4.3	Resistivity of thin films with $\delta$ -layers . . . . .	68
4.4	The Hall effect in thin films with impurity $\delta$ -layers . . . . .	71
4.4.1	The anomalous Hall effect in Cu( $\delta$ Fe) . . . . .	72
4.4.2	The ordinary Hall effect in Cu with impurity $\delta$ -layers . . . . .	75
4.5	Summary . . . . .	78
<b>5</b>	<b>The effect of localised Fe impurities on the magnetotransport of thin Pt films</b>	<b>80</b>
5.1	Introduction . . . . .	81
5.2	Magnetotransport of thin and ultrathin Pt films . . . . .	81
5.2.1	Resistivity as a function of temperature . . . . .	82
5.2.2	Conventional magnetoresistance . . . . .	86
5.2.3	Angle-dependent magnetoresistance . . . . .	87
5.2.4	The Hall effect . . . . .	90
5.3	Interfacial Fe doping in the magnetotransport of ultrathin Pt films . . . . .	93
5.3.1	Resistivity as a function of temperature . . . . .	94
5.3.2	Conventional magnetoresistance . . . . .	95
5.3.3	Angle-dependent magnetoresistance . . . . .	98

5.3.4	The Hall effect . . . . .	101
5.4	Thickness dependence of the magnetotransport of Pt thin films with a discontinuous interfacial layer of Fe . . . . .	107
5.5	Summary . . . . .	108
<b>6</b>	<b>Interfacial dependence of magnetotransport in YIG/Pt bilayers</b>	<b>111</b>
6.1	Introduction . . . . .	112
6.2	Characterisation of YIG . . . . .	112
6.2.1	Magnetometry . . . . .	112
6.2.2	X-ray diffraction . . . . .	114
6.3	Resistivity and its temperature dependence in YIG/metal bilayers . . .	116
6.3.1	Resistivity of YIG/Cu bilayers . . . . .	121
6.4	Angle-dependent magnetoresistance in YIG/Pt bilayers . . . . .	123
6.4.1	Field dependence of the spin Hall magnetoresistance . . . . .	123
6.4.2	Temperature dependence of the ADMR . . . . .	126
6.5	Conventional magnetoresistance and its temperature dependence in YIG/Pt bilayers . . . . .	130
6.6	The interfacial Hall effect . . . . .	134
6.6.1	The spin Hall-anomalous Hall effect . . . . .	139
6.7	Summary . . . . .	141
<b>7</b>	<b>Conclusions and future work</b>	<b>143</b>
<b>A</b>	<b>X-ray Reflectivity of YIG</b>	<b>147</b>
	<b>References</b>	<b>151</b>

## Abbreviations

MPE	magnetic proximity effect	PSHMR	paramagnetic spin Hall magnetoresistance
SHMR	spin Hall magnetoresistance	YIG	yttrium iron garnet
LPE	liquid phase epitaxy	PLD	pulsed laser deposition
GGG	gadolinium gallium garnet	YAG	yttrium aluminium garnet
AHE	anomalous Hall effect	SHE	spin Hall effect
SH-AHE	spin Hall-anomalous Hall effect	AMR	anisotropic magnetoresistance
dc	direct current	rf	radio frequency
SCCM	standard cubic centimetres per minute	VSM	vibrating sample magnetometer
EMF	electromotive force	VTI	variable temperature insert
DAQ	data acquisition	ac	alternating current
MR	magnetoresistance	ADMR	angle-dependent magnetoresistance
SHA	spin Hall angle	ML	monolayer
OHE	ordinary Hall effect	SOC	spin-orbit coupling

---

# CHAPTER 1

---

Introduction

---

Spintronics is a field which makes use of the quantum mechanical property of spin in order to harness the full potential of electrons and pave the way for devices which exceed the capabilities of microelectronics alone [1; 2]. It is an area of research which has expanded greatly over the last few decades, deepening our knowledge of the fundamental mechanisms of physical phenomena known long before its germination, whilst promising a future of higher functionality devices with lower power consumption than currently provided by conventional microelectronics [1–3]. Whilst there are many avenues through which to explore the potential of spintronics, spin currents in metallic devices [4; 5] and spin waves in metal/insulator systems [6] are two promising candidates. A spin current involves the movement of electrons in a bidirectional manner such that there is no net charge flow, yet a net flow of spin occurs. This is simply produced within some metals by the application of a charge current through the spin Hall effect [7; 8]. In order to exploit this effect for spintronic applications, particular device designs must be used [5]. The inverse of this effect causes the conversion from a spin current to a charge current, allowing detection of a spin current through conventional electronic methods [9]. This method can also be used to detect spin waves, also known as magnons, which can travel through magnetic insulators with very low dissipation [6].

Over the last few years, there has been a great deal of interest placed in improving the efficiency of spin Hall effect devices, with promise shown for the inclusion of dilute amounts of impurities to produce a large extrinsic spin Hall effect [10–15]. Localised discontinuous layers of impurities, known as  $\delta$ -layers, have been predicted to produce an even greater enhancement to the extrinsic spin Hall effect [16]. The potential for using such alloy systems in spintronic devices involving a magnetic insulator raises questions regarding interfacial phenomena. A great deal of research has taken place in the realm of insulating magnet/normal metal bilayer structures, with the discovery of the spin Hall magnetoresistance, where the magnetisation direction of the magnetic layer changes the resistance of the metal layer through the spin Hall effect, leading to further potential device applications [17]. The quality of the interface between the two materials has proven of paramount importance in producing a large effect [18; 19], though conflicting data have emerged regarding the possibility of a magnetic proximity effect at the interface [20–23]. In the body of work presented in this thesis,

---

extrinsic spin-orbit scattering phenomena are probed via magnetotransport measurements of thin films doped with extrinsic impurities and of insulating magnet/normal metal bilayers with various interface preparation methods.

In chapter 2, the fundamental theory from the extrinsic spin-orbit interaction, the spin Hall effect and the spin Hall magnetoresistance are discussed. This is in addition to a discussion of other phenomena necessary for a thorough physical understanding of the devices in use, including quantum interference effects and the magnetic proximity effect. An overview is given of the current research landscape in magnetic insulator/normal metal bilayers with a focus on the emergence of interface-related phenomena in the observed magnetotransport.

The experimental techniques required for the fabrication and characterisation of thin films with localised impurity  $\delta$ -layers and insulating magnet/normal metal bilayers are outlined in chapter 3. The magnetotransport phenomena of these films are measured over a wide temperature range in gas flow liquid He cryostats, whose principles of operation are outlined in chapter 3 along with a definition of the measurement geometry.

The resistivity and ordinary Hall effect of non-magnetic thin films with an impurity  $\delta$ -layer are investigated in chapter 4. The dependence on the position of  $\delta$ -layers of materials with high spin-orbit coupling Ta, W, Bi and Ir are investigated within a Cu host layer to determine their contribution to the ordinary Hall effect. Magnetic impurities in the form of Fe  $\delta$ -layers are introduced and investigated for the position-dependent effect on the ordinary and anomalous Hall coefficients.

The magnetotransport of both thin and ultrathin films of Pt are investigated at the start of chapter 5 before a discontinuous  $\delta$ -layer of Fe impurities are introduced for ultrathin Pt at the interface with an  $\text{Al}_2\text{O}_3$  substrate. A thorough investigation of the magnetoresistance in fixed orientations and with a rotating field is applied for films with two different Fe concentrations as a function of temperature. The anomalous Hall effect observed in these films is then explored, with the temperature dependence of its coefficients presented. The presence of weak (anti-)localisation and the enhanced

---

electron-electron interaction is explored in these films.

The magnetotransport work on interfacial magnetic impurities in ultrathin Pt presented in chapter 5 forms a basis for comparison of results in magnetic insulator/metal bilayers which are presented in chapter 6. The same measurement types are explored for samples of yttrium iron garnet ( $\text{Y}_3\text{Fe}_5\text{O}_{12}$ , YIG) with ultrathin Pt deposited on top. The YIG/Pt bilayers are prepared four different ways: with amorphous YIG, ordered YIG, etched YIG and with a  $\delta$ -layer of Fe between the YIG and Pt layers. The relative contributions to the magnetotransport from the spin mixing conductance and also from the magnetic proximity effect or an interfacial intermixing of material is discussed. The spin Hall-anomalous Hall effect, observed exclusively in insulating magnet/normal metal bilayers, is presented as a function of temperature for the first time.

In chapter 7, the data from the preceding three chapters are summarised and consolidated into a cohesive conclusion. Suggestions of future work are given in order for the fundamental phenomena at play in the systems studied within this thesis to be further characterised and better understood. A roadmap for future applications of the information presented in this thesis is also presented.

---

# CHAPTER 2

---

Background

## 2.1 Introduction

The work presented in this thesis builds upon many of the fundamental concepts in condensed matter physics. Its title reflects the exceptional importance of the extrinsic spin-orbit scattering in the phenomena here reported. Indeed, this scattering process is fundamental to many areas of spintronics and has been shown to play a leading role in the enhancement of spin Hall device efficiency [10–12; 14–16; 24–27]. Electrical transport measurements are performed on thin metallic films which exhibit phenomena such as weak anti-localisation due to spin-orbit effects and spin Hall magnetoresistance. In this chapter, the background physics will be discussed along with an overview of the current state of extrinsic spin-orbit scattering and its related phenomena within condensed matter physics.

## 2.2 Thin film transport

Metallic thin films are used throughout this project with varying thicknesses, ranging from ultrathin films, where the mean free path is larger than the thickness of the metal, leading to a two-dimensional sample, to those thick enough to possess some bulk-like transport properties. Here, the essential concepts which govern the effects of geometry and impurities on thin film resistivity are explored. The free electron theory of metals was used to discuss the conductivity of thin films by Fuchs in 1938 [28]. Later, this was combined with the ideas of Sondheimer on the mean free path of electrons in real metals [29] to form the Fuchs-Sondheimer theory for thin film resistivity, which is widely employed and applicable to most thin film systems [30]. Simply from classical physics, the resistivity of a thin film is expected to be higher than for a bulk sample. If the film thickness becomes comparable to the mean free path of the conduction electrons, then scattering from the film surfaces will dominate the resistivity [31]. Matthiesen’s rule states that if each scattering process is independent, its contribution to the resistivity can be calculated and combined using the relaxation time [32; 33]. This can be given by

$$\frac{1}{\tau} = \sum_n \frac{1}{\tau_n} \quad (2.1)$$

where  $1/\tau$  is the total scattering rate and  $\tau$  the total relaxation time, while the sum over all  $\tau_n$  represents any and all independent scattering types present in the system. This includes, but is not limited to,  $\tau_{\text{ph}}$  for electron-phonon scattering and  $\tau_0$  for scattering from inherent defects within the film. Deviations from Matthiessen's rule often indicate new physics. Fuchs found that the conductivity of thin films can be described by

$$\sigma_t = \frac{\sigma_0 \kappa}{\Phi(\kappa)} \quad (2.2)$$

where  $\sigma_t$  is the conductivity of a film of thickness  $t$ ,  $\sigma_0$  is the bulk conductivity found from the Drude formula,  $\kappa = t/\lambda$  where  $\lambda$  is the mean free path of the conduction electrons and the function  $\Phi(\kappa)$  is given by

$$\frac{1}{\Phi(\kappa)} = \frac{1}{\kappa} - \frac{3}{4} \left(1 - \frac{1}{12}\kappa^2\right) Ei(-\kappa) - \frac{3}{8\kappa^2} (1 - e^{-\kappa}) - \left(\frac{5}{8\kappa} + \frac{1}{16} + \frac{\kappa}{16}\right) e^{-\kappa} \quad (2.3)$$

involving the integral

$$-Ei(-\kappa) = \int_{\kappa}^{\infty} \frac{e^{-t}}{t} dt \quad (2.4)$$

and the Drude formula for the bulk conductivity is

$$\sigma_0 = \frac{ne^2\tau}{m_e} \quad (2.5)$$

where  $n$  is the number density of electrons,  $e$  the charge of an electron,  $\tau$  the relaxation time of the conduction electrons and  $m_e$  the electronic mass. Sondheimer created an approximate equation which simplifies the Fuchs-Sondheimer theory to allow for a simple determination of the effects of film thickness on the resistivity [28–30], namely

$$\rho(t) \approx \rho_0 + \frac{3}{8}\rho_0\lambda_0\frac{1}{t}(1-p) \quad (2.6)$$

where  $\rho(t)$  is the resistivity of a thin metal film of thickness  $t$ ,  $\rho_0$  is the resistivity of a bulk sample of the same composition,  $\lambda_0$  is the mean free path of the conduction electrons in the bulk and  $p$  is the parameter governing surface scattering. The film surfaces are assumed to be smooth and parallel [28–30]. This simplification is valid when  $t \gg \lambda$  but has been found to be valid for much thinner films also [30; 34; 35]. Grain boundary scattering is also a source of resistivity in thin films [36], but is not studied in this thesis due to a lack of transmission electron microscopy (TEM) data and hence an inability to accurately determine grain size.

### 2.2.1 Magnetoresistance in thin films

The application of a magnetic field is known to affect the resistance of a thin film and is measured using

$$\frac{\Delta\rho}{\rho_0} = \frac{\rho(H) - \rho(H=0)}{\rho(H=0)} \quad (2.7)$$

where  $\rho(H)$  is the sample resistivity at an applied field  $H$  while  $\rho_0 = \rho(H=0)$  is the resistivity in zero field. In most cases, a magnetic field acts to increase the resistance, but in some cases can reduce it [37]. In the free electron model, the magnetoresistance is predicted to be zero but in the case of transition metals and the application of a two-band model for  $s$ - $d$  scattering, the observed magnetoresistance can be explained [37]. There are three orientations for the measurement of thin film magnetoresistance (MR): longitudinal, where the field is applied parallel to the applied current; transverse, where the field is applied perpendicular to the applied current but in the plane of the sample and perpendicular, where the field is applied out of the plane of the sample. These are illustrated as being along the  $x$ ,  $y$  and  $z$  axes respectively in fig. 3.6. For normal MR Köhler's rule is valid, namely

$$\frac{\Delta\rho}{\rho_0} = F\left(\frac{H}{\rho_0}\right) \quad (2.8)$$

where  $\rho_0$  is the zero-field resistivity,  $\Delta\rho = \rho(H) - \rho_0$ ,  $H$  is the applied field and  $F$  is a function for a particular type of material. For perpendicular MR in a non-magnetic normal metal, this becomes

$$\frac{\Delta\rho}{\rho_0} = (\omega_c\tau)^2 = \left(\frac{eB}{m_e}\tau\right)^2 = \left(\frac{ne^2\tau}{m_e} \frac{1}{ne} B\right)^2 = \left(\frac{R_H}{\rho_0}\right)^2 B^2 \quad (2.9)$$

where  $\omega_c = eB/m_e$  the cyclotron frequency,  $\tau$  the relaxation time,  $e$  the electronic charge with value  $-1.6 \times 10^{-19}$  C,  $B = \mu_0 H$  is the magnetic flux density from the applied field  $H$ ,  $m_e$  the electronic mass and  $R_H = 1/ne$  is the free electron ordinary Hall coefficient [37; 38]. This magnetoresistance is positive and proportional to  $B^2$ . For a normal metal, one can estimate the magnitude of this magnetoresistance by considering a typical  $R_H \approx -10^{-10} \Omega\text{m T}^{-1}$  with  $\rho_0 \approx 10^{-8} \Omega\text{m}$  giving  $\Delta\rho/\rho_0 \approx 10^{-4} B^2$ .

The theory of Fuchs discussed in section 2.2 was used to describe how the thickness of a thin film affects its resistivity, but this also has implications for the MR, leading to

the phenomenon known as thin film MR [28; 39]. This is applicable to the longitudinal MR in a thin film given by

$$\frac{\sigma}{\sigma_0} = 1 - \frac{3}{16\kappa} \left[ 2 - \frac{\beta^2}{4\kappa^2 + \beta^2} (1 + e^{-2\pi\kappa/\beta}) \right] \quad (2.10)$$

where  $\sigma$  is the conductivity,  $\sigma_0$  the bulk conductivity and  $\kappa = t/\lambda$  as for equation 2.2. Here  $\beta = t/r_0$  where  $t$  is the sample thickness and  $r_0 = m_e v/eB$  is the radius of curvature where  $m_e$  is the electron mass,  $v$  the electron drift velocity, and  $B$  the flux density from the applied magnetic field [39]. This relation holds true for  $\beta \geq 2$  [39]. In the limit  $\kappa/\beta \gg 1$  equation 2.10 reduces to equation 2.6 for a thin film in the absence of a magnetic field [28–30; 39]. Electrons with drift velocity  $v$  which form the angle  $\delta$  with the applied field  $B$  traverse a helical path around the axis of the applied field with radius  $r = r_0 \sin \delta$  where  $\delta$  is the angle between the electron velocity and the field direction. As  $B$  is increased, the surface scattering is reduced which means this effect produces a negative MR [39].

Anisotropic magnetoresistance (AMR) is a phenomenon observed in ferromagnetic metals, where the longitudinal and perpendicular MRs have different magnitudes, causing an angle-dependent change in resistance at a constant applied field [40]. The effect is caused by the spin-orbit interaction and hence more scattering occurs when the current and orbital moment are in the same plane, leading to the following angle dependence:

$$\rho(\theta) = \rho_{\perp} + (\rho_{\parallel} - \rho_{\perp}) \cos^2(\theta) \quad (2.11)$$

where  $\theta$  represents the angle between the current density  $\vec{j}$  and the magnetisation  $\vec{M}$ , which is defined by the direction of  $B$  [40]. For  $\vec{j} \parallel \vec{M}$  the resistivity is  $\rho_{\parallel}$  and for  $\vec{j} \perp \vec{M}$  the resistivity is  $\rho_{\perp}$  [40].

## 2.3 Extrinsic spin-orbit scattering

An intrinsic effect plays a role in the anomalous and spin Hall effects which is a consequence of the band structure, and this is discussed further in section 2.4.2, while extrinsic phenomena refer to effects resulting from the addition of impurities and/or

## 2.3 Extrinsic spin-orbit scattering

---

defects. Extrinsic spin-orbit scattering is a phenomenon which has garnered much interest in recent years due to its potential to enhance the efficiency of spin Hall effect devices [10; 24; 26]. It is one of the central mechanisms in both the anomalous and spin Hall effects, as will be discussed in sections 2.4 and 2.5, and here we discuss the mechanics of it. First, we discuss the spin-orbit interaction, a fundamental quantum mechanical interaction which is responsible for so much of the phenomena observed in condensed matter physics, and the cause of spin-orbit scattering. The spin-orbit interaction is the interaction between an electron's spin and its orbital angular momentum. The spin-orbit Hamiltonian is

$$H_{\text{so}} = \lambda_{\text{so}} \hat{l} \cdot \hat{s} \quad (2.12)$$

where  $\lambda_{\text{so}}$  is the spin-orbit coupling energy,  $\hat{l}$  is the orbital angular momentum operator and  $\hat{s}$  is the spin angular momentum operator. From the rest frame of the electron, the Lorentz transformation of the impurity potential means that the electron experiences a magnetic field. The impurity ion appears to orbit the electron with velocity  $v$  and radius  $r$ , and if the charge on the impurity ion is  $Ze$ , the effective magnetic field experienced by the electron has the magnitude

$$B_{\text{so}} = \frac{\mu_0 Z e v}{4\pi r^2} \quad (2.13)$$

where  $Z$  represents the number of protons present in the impurity ion [41]. The motion of the electron then reacts to the effective magnetic field in a spin-dependent manner. The interaction energy  $\epsilon_{\text{so}}$  is given by

$$\epsilon_{\text{so}} = -\mu_{\text{B}} B_{\text{so}} \approx -\frac{\mu_0 \mu_{\text{B}} Z e v}{4\pi r^2} \quad (2.14)$$

where  $\mu_{\text{B}}$  is the Bohr magneton [41]. Here, the effective magnetic field is caused by a scattering centre, which may be an impurity ion or defect in the sample. For real-world metals, the actual power of  $Z$  varies between one and four [41]. This is the extrinsic spin-orbit interaction. There are two types of spin-dependent scattering relevant to this work which arise from the extrinsic spin-orbit interaction; these are skew scattering and scattering with side jump, illustrated in fig. 2.1.

Skew scattering is depicted in fig. 2.1b) at a single impurity site. Incident electrons of opposite spin are deflected on their path either toward the scattering centre or away

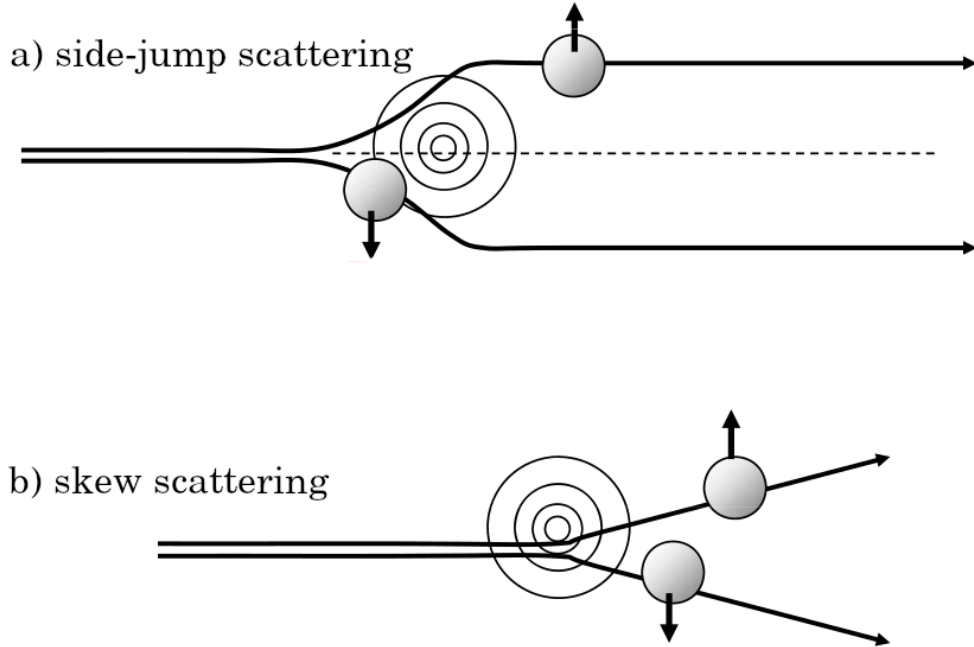


Figure 2.1: *Extrinsic spin-orbit scattering causes a conduction electron to experience an effective magnetic field at a scattering centre and leads to spin-dependent scattering. Shown are a) side-jump scattering and b) skew scattering. Image taken from [3] and modified for simplicity.*

from it, dependent upon their spin. The model for this mechanism of scattering was first proposed in the 1950s by J. Smit, in order to explain the anomalous Hall effect observed in ferromagnets [42; 43]. In the case of impurities, the extent of the deflection depends upon the contrast in spin-orbit coupling between the impurity and host. Heavier metals tend to produce larger spin-orbit effects than their lighter counterparts, as shown in equation 2.14 [41; 44]. It is for this reason that heavier metals have been chosen as impurities in lighter hosts for studies on phenomena resulting from extrinsic skew scattering [10; 12; 14; 15]. This asymmetric scattering can be modelled by the Boltzmann transport equation and yields a contribution to the anomalous Hall resistivity  $\rho_{xy}^{\text{AHE}}$  which is directly proportional to the longitudinal charge resistivity  $\rho_{xx}$  [3; 42; 43; 45; 46].

Scattering with side-jump is a more complex phenomenon which remains a topic of

## 2.3 Extrinsic spin-orbit scattering

---

controversy, and is illustrated in fig. 2.1a). This model of scattering was first proposed by L. Berger in 1970, once again to improve understanding of the anomalous Hall effect [47; 48]. This type of scattering generally occurs for larger concentrations of impurities, or under specific resonance conditions [14; 15; 49]. Initially, it was thought the phenomenon was present for systems where the relaxation time of the itinerant electron was relatively small; typically at high temperatures and in more concentrated alloys [47; 48]. This was later doubted, and it has been posited that the phenomenon is independent of the electron relaxation time [3; 45; 50]. To summarise, an itinerant electron experiences a field gradient through its deflection, causing it to accelerate or decelerate. This results in a transverse displacement of the electron, i.e. a side jump, whose magnitude is typically of the order  $10^{-11}$  m [47; 48]. Asymmetric skew scattering is usually superimposed with this side jump, causing the trajectory of the scattered electron to deflect to the left or the right in a spin-dependent manner [47; 48]. The side-jump mechanism contributes to the anomalous Hall resistivity  $\rho_{xy}^{\text{AHE}}$  a term directly proportional to square of the longitudinal charge resistivity,  $\rho_{xx}^2$ , and cannot be described by the Boltzmann transport equation without additional terms [46–48]. Its contribution to the anomalous Hall resistivity and how this can be measured is discussed further in section 2.4.2.

Skew scattering and scattering with side-jump are both examples of spin-flip scattering, where there is a non-zero probability that the electron spin is flipped during the scattering event. The mechanism which facilitates this type of spin-flip scattering is the Elliott-Yafet mechanism, as the spin relaxes during the scattering event [51; 52]. At temperatures greater than around 20 K, spin-flip scattering is mediated by phonons. At each scattering event, there is a finite probability the spin will flip and hence the scattering rate is proportional to the phonon scattering rate. Another form of scattering is that governed by the D'yakonov-Perel mechanism, where spin relaxation occurs between scattering events [53; 54]. The types of extrinsic spin-orbit scattering can be distinguished experimentally through analysis of the anomalous and spin Hall effects; these methods are described in the following section.

## 2.4 The ordinary, anomalous and spin Hall effects

The three Hall effects which are studied within this thesis are the ordinary, anomalous and spin Hall effects. Here, an overview of all three is given.

### 2.4.1 The ordinary Hall effect

The ordinary Hall effect (OHE) was first discovered by Hall in 1879 [55] and is caused by the Lorentz force acting on the conduction electrons. The Lorentz force is described by

$$\vec{F} = e \left( \vec{E} + \vec{v} \times \vec{B} \right) \quad (2.15)$$

where  $\vec{F}$  is the force acting on the conduction electron,  $e$  is its charge,  $\vec{E}$  is the electric field driving the current,  $\vec{v}$  is the electronic drift velocity and  $\vec{B}$  is the magnitude of the applied magnetic field. The Hall effect manifests when a magnetic field is applied perpendicular to the plane of a sample, causing the electrons to deflect to one side of the conductor, resulting in a build-up of charge. This leads to a Hall potential along the transverse direction of the conductor. This can be measured as a Hall voltage with probes at the sides of the sample. The Hall voltage for a free electron system can be calculated as follows

$$V_H = \frac{IB}{net} \quad (2.16)$$

where  $V_H$  is the Hall voltage,  $I$  is the magnitude of the charge current,  $B$  of the magnetic field,  $n$  is the density of charge carriers,  $e$  the charge on an electron and  $t$  the thickness of the sample. The Hall effect in these systems is characterised by the free electron ordinary Hall coefficient, found from

$$R_{fe} = \frac{E_H}{j_x B} = \frac{V_H t}{IB} = \frac{1}{ne} \quad (2.17)$$

where  $R_{fe}$  is the free electron ordinary Hall coefficient,  $E_H = V_H/w$  the electric field in the transverse direction, where  $w$  is the width of the sample, and  $j_x$  the current density along the current direction. This quantity is independent of sample geometry, making it an ideal candidate for a standard coefficient [32; 55–57]. Another quantity which is useful to define is the Hall resistivity, defined as

$$\rho_{xy} = \frac{V_H t}{I} = R_{fe} B \quad (2.18)$$

## 2.4 The ordinary, anomalous and spin Hall effects

where  $\rho_{xy}$  is the Hall resistivity. This quantity is plotted against the applied field,  $B$ , to form a linear gradient which is equal to the free electron Hall coefficient,  $R_{fe}$ . A typical way of measuring the Hall voltage involves use of a Hall bar shape, as depicted in fig. 2.2a), with the field applied along the  $n$ -axis, current applied along  $j$  and the Hall voltage measured across  $V_{trans}$ . A typical response of the Hall resistivity is shown in fig. 2.2c) for a clean Cu sample.

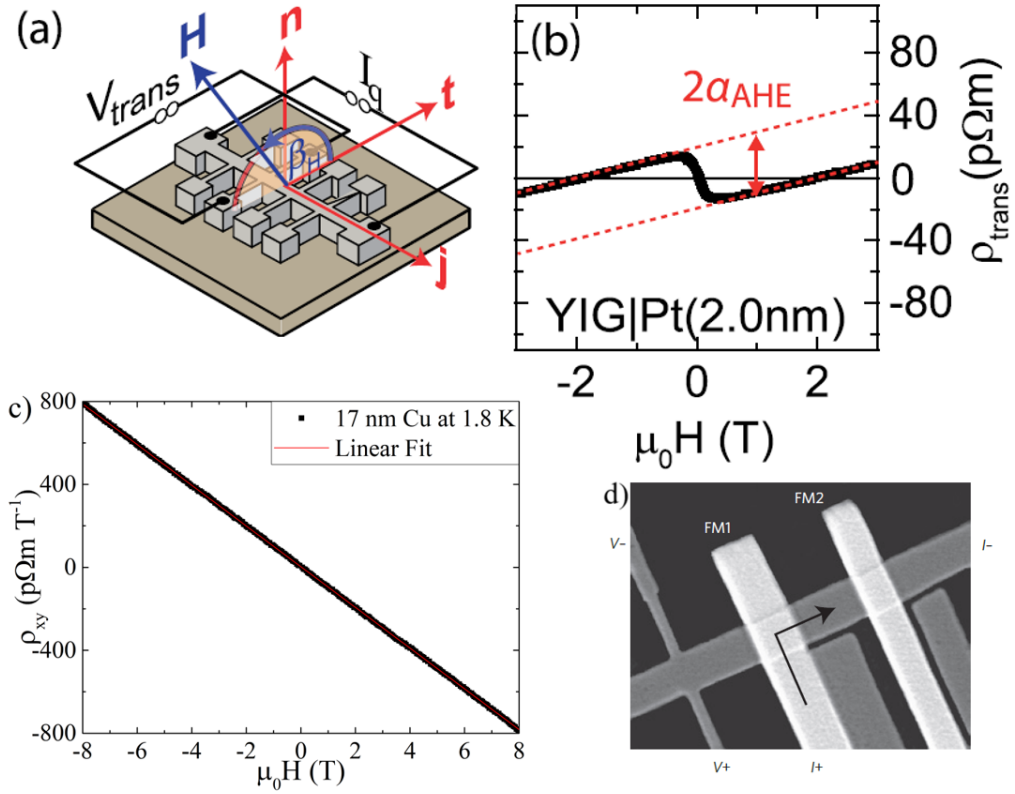


Figure 2.2: The ordinary and anomalous Hall effects are measured for a) a Hall bar shape, with b) showing the output for an anomalous Hall system with spontaneous Hall coefficient  $\alpha_{AHE} \equiv R_S$ . The output for the ordinary Hall effect of pure Cu is shown in c) whilst d) shows a lateral spin valve device used to measure the inverse spin Hall effect. Images a) and b) are taken from [58], while d) is taken from [59].

The conventional Hall angle  $\phi$  is shown in fig. 2.3. With a current applied to a conducting metal, free electrons flow parallel to the current density  $\vec{j}$  and are accelerated by  $m_e d\vec{v}/dt = e\vec{E}$  where  $m_e$  is the effective mass of the electrons,  $\vec{v}$  their

## 2.4 The ordinary, anomalous and spin Hall effects

---

drift velocity and  $\vec{E}$  the resultant electric field. In the steady state,  $d\vec{j}/dt = 0$  and has two components: a general rise in current density from the acceleration of electrons, and a reduction in current density due to scattering. The momentum density  $\vec{P} = \sum m_e \vec{v} = m_e \vec{j}/e$  must also lead to  $d\vec{P}/dt = 0$  in the steady state as follows

$$\frac{d\vec{P}}{dt} = ne\vec{E} - \frac{\vec{P}}{\tau} \quad (2.19)$$

where  $n$  is the number density of electrons and  $\tau$  is the scattering time of the electrons. In the case of an applied magnetic field perpendicular to the current density  $\vec{j}$ , as illustrated in fig. 2.3, the Lorentz force is exerted on the electrons  $e\vec{v} \times \vec{B}$  individually and  $\vec{j} \times \vec{B}$  across the ensemble [60]. In the steady state, therefore

$$0 = ne\vec{E} - \frac{\vec{P}}{\tau} + \vec{j} \times \vec{B} = ne\vec{E} - \frac{m_e \vec{j}}{e\tau} + \vec{j} \times \vec{B} \quad (2.20)$$

as shown by Pippard [60]. The Lorentz force hence causes a transverse component of the electric field with magnitude  $jB/ne$  which is the Hall field [55; 60], while  $\phi$  is the Hall angle, representing the angle between the applied current and the total resultant electric field in the presence of a magnetic field, which can be expressed as

$$\tan(\phi) = \frac{eB\tau}{m_e} = \omega_c \tau \quad (2.21)$$

where  $\omega_c = eB/m_e$  is the cyclotron frequency [60].

Whilst the free electron Hall coefficient remains prevalent in modern literature, it is not applicable when scattering sites are introduced or in the case of transition metals such as Fe where the topology of the Fermi surface becomes an important factor [49; 57; 61–68]. More generally

$$R_H = \frac{\sigma_H}{\sigma_0^2} \quad (2.22)$$

where  $R_H$  is the Hall coefficient,  $\sigma_H$  is the Hall conductivity and  $\sigma_0 = \sigma_{xx}$  the linear conductivity in the low field limit [57]. For a spherical Fermi surface, where  $\tau$  is isotropic in  $k$ -space,  $\sigma_H$  does not depend upon the magnitude of  $\tau$  but  $R_H$  is still altered by the presence of impurities. For the case where  $\tau$  is not isotropic,  $\sigma_H$  becomes a function of  $\tau$  [57; 62]. This means that scattering from impurities, both magnetic and non-magnetic, can change the value of the Hall coefficient and can even cause it to

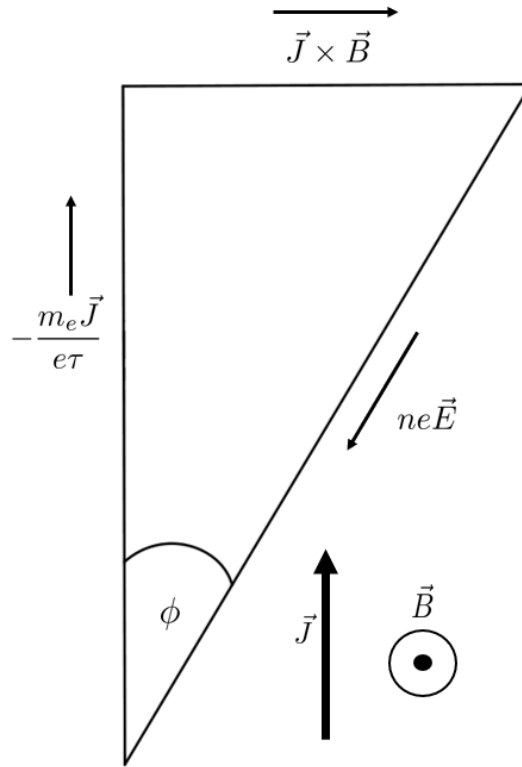


Figure 2.3: The Hall angle  $\phi$  in a metallic conductor with applied current density  $\vec{J}$  and applied field  $\vec{B}$ . Figure inspired by [60].

become a function of field; this is illustrated in fig. 2.4. An example of the temperature and field dependence of the Hall resistivity is shown in fig. 2.5.

Curves A and B from fig. 2.4b) show a point 'x' where a transition occurs from the low to high field regimes. For curve A, there is no difference in the Hall resistivity compared to the undoped sample in the low field regime; this corresponds to a very low concentration of impurities with very little scattering present. For curve B, there is a marked difference in the low field regime behaviour due to the spin effect, and at higher fields linear behaviour resumes; this would indicate a greater concentration of magnetic scattering sites. For curve C in fig. 2.4b), the sample does not leave the low field regime; this indicates that scattering from impurities dominates the Hall response and generally applies for the highest concentrations of dilute magnetic impurities [57].

## 2.4 The ordinary, anomalous and spin Hall effects

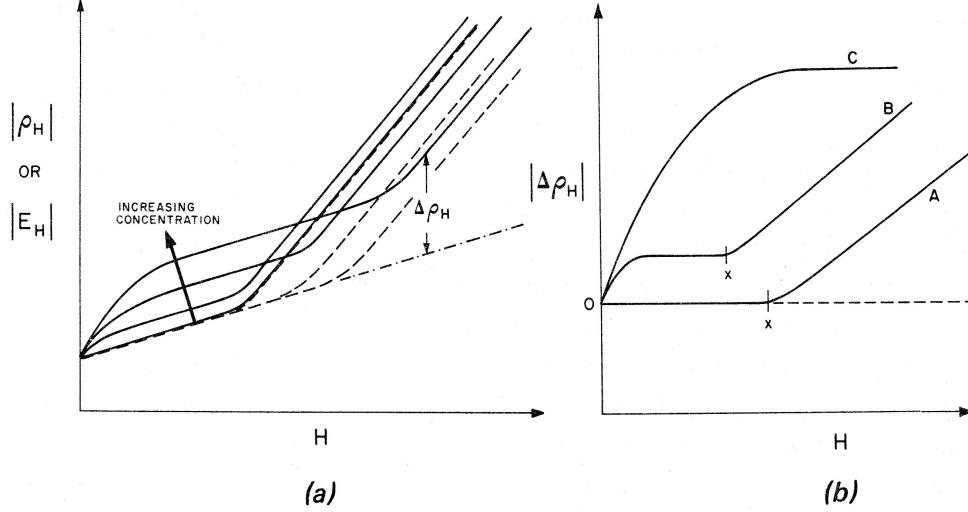


Figure 2.4: The change in the magnitude of a) the Hall resistivity for a non-magnetic host with magnetic impurities (solid lines) and non-magnetic impurities (dashed lines) when undergoing the low-high field transition and b) the various forms the change in the Hall resistivity, as illustrated in a), can take as a function of applied field. This figure is taken from [57].

Scattering from impurities, be they magnetic or non-magnetic, produces a concentration-dependent change in the ordinary Hall coefficient in the intermediate field region, as depicted in fig. 2.4a), but can also in reality modify the Hall coefficient in the low field regime [57]. In this regime, the Lorentz force is a small perturbation compared to the scattering. The reduced Hall coefficient  $r$  can be defined, as given by Dugdale, Firth and Hurd [33; 57; 62], which is the ratio of the ordinary Hall coefficient of the alloy system  $R_H$  to the free electron value  $R_{fe}$ , expressed as

$$r = \frac{R_H}{R_{fe}} = 4\pi \frac{\tau_B^2 \int_B \overline{(1/\varrho)} v^2 d\vec{S} + \tau_N^2 \int_N \overline{(1/\varrho)} v^2 d\vec{S}}{\left( \tau_B \int_B v d\vec{S} + \tau_N \int_N v d\vec{S} \right)^2} \quad (2.23)$$

where  $\overline{(1/\varrho)}$  is the mean curvature of the Fermi surface at point  $\vec{k}$  with drift velocity  $v$  and  $d\vec{S}$  is the surface element of the Fermi surface. This expression assumes a two-band model for conduction, with the bands represented by subscripts B and N such that  $\tau_B$  and  $\tau_N$  are the scattering times for each band.

## 2.4 The ordinary, anomalous and spin Hall effects

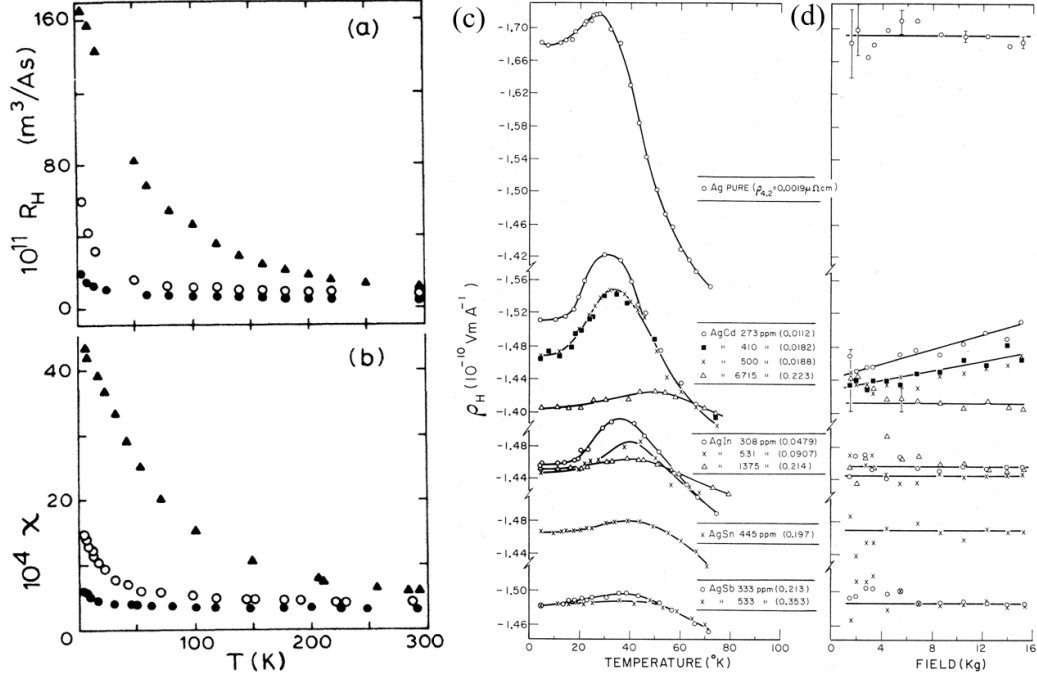


Figure 2.5: The (a) ordinary Hall coefficient and (b) paramagnetic susceptibility are shown as a function of temperature for amorphous paramagnetic  $\text{Zr}_{1-x}\text{Fe}_x$  alloys with  $x = 33$  (filled circle),  $x = 35$  (open circle) and  $x = 37.5$  (filled triangle), taken from [69]. The Hall resistivity  $\rho_H$  for silver, in its pure form, and doped with non-magnetic impurities cadmium, indium, tin and antimony at various concentrations is shown varying as a function of (c) temperature and (d) applied magnetic field, taken from [57; 66].

### 2.4.1.1 The spin effect

One effect which can be seen to enhance the ordinary Hall effect as a function of field is the spin effect. This effect arises from the exchange interaction between localised spins and conduction electrons ( $\approx s \cdot S$ ) in dilute magnetic alloys [49]. The spin scattering which results, in the absence of skew scattering, leads to

$$\rho_{xy} = \left[ 1 + \left( \frac{i_+ - i_-}{i_+ + i_-} \right)^2 \right] R_H H \quad (2.24)$$

where  $i_+$  and  $i_-$  represent the spin-up and spin-down currents, respectively. This difference in the currents for differing spins is caused only by the difference in relaxation times and is not a consequence of skew scattering [49]. Experimentally, the enhance-

ment factor is generally only slightly above unity [49] but can be observed as a field-dependent increase in the Hall resistivity on top of the linear Hall signal.

### 2.4.2 The anomalous Hall effect

The anomalous Hall effect (AHE) was also discovered by Edwin H. Hall two years after his publication on the ordinary Hall effect, in 1881 [70]. In ferromagnets, the Hall effect is seen to evolve differently in an applied field, with a large contribution to the Hall potential at lower fields. At higher fields, this contribution is found to remain constant and a linear dependence on the field from the ordinary Hall effect results [3; 70]. The anomalous Hall effect is characterised by the anomalous Hall coefficient,  $R_{\text{AHE}}$ , which is defined via the empirical relation

$$\rho_{xy} = \mu_0(R_{\text{H}}H + R_{\text{AHE}}M) \quad (2.25)$$

found by Pugh and Lippert in the early 1930s [71; 72] where  $\rho_{xy}$  is the total Hall resistivity,  $\mu_0$  is the permeability of free space,  $H$  is the applied magnetic field,  $R_{\text{H}}$  is the ordinary Hall coefficient,  $R_{\text{AHE}}$  is the conventional anomalous Hall coefficient and  $M$  is the magnetisation of the sample [3; 70]. The origin of the anomalous Hall effect was debated for over a century, but has been found to have a number of factors which contribute to it [3; 45; 50; 73]. An intrinsic contribution occurs, which causes a transverse separation of spin along the current channel as follows

$$\frac{d\langle\vec{r}\rangle}{dt} = \frac{1}{\hbar} \frac{\partial E}{\partial \vec{k}} + \frac{e}{\hbar} E \times b_n \quad (2.26)$$

where  $d\langle\vec{r}\rangle/dt$  is the transverse spin-dependent velocity,  $E$  is the magnitude of the applied electric field,  $\vec{k}$  is the electronic wavevector and  $b_n$  is the electron Berry's phase curvature [3]. This separation of spin causes a transverse potential, as conduction electrons in ferromagnets possess a preferred spin [3; 45; 74–76]. This potential forms part of the anomalous Hall resistivity. Extrinsic spin-orbit scattering was first proposed to play a role in the anomalous Hall effect by Karplus and Luttinger [77; 78], and models of these scattering phenomena followed. Skew scattering [42; 43] and scattering with side jump [47; 48] contribute to the anomalous Hall resistivity, and can have the same or opposite sign, depending upon the material and alloy; this is true for their

## 2.4 The ordinary, anomalous and spin Hall effects

---

contribution to both the anomalous and spin Hall effects [14; 57; 63; 68; 79]. The total anomalous Hall resistivity  $\rho_{xy}^{\text{AHE}} = \mu_0 R_{\text{AHE}} M$  can also be expressed as

$$\rho_{xy}^{\text{AHE}} = \Phi_{\text{sk}} \rho_0 + \left( \kappa^{\text{sj}} - \frac{e^2}{8\pi^3 \hbar} \int_{\text{BZ}} \Omega(\vec{k}) d^3 k \right) \rho_0^2 \quad (2.27)$$

where  $\Phi_{\text{sk}}$  represents a skew scattering coefficient,  $\rho_0$  is the value of the longitudinal resistivity  $\rho_{xx}$  at zero applied field and  $\kappa^{\text{sj}}$  a side-jump scattering coefficient. The final term which is multiplied by  $\rho_0^2$  represents the contribution from the intrinsic AHE;  $\Omega(\vec{k})$  is the Berry curvature at wave vector  $\vec{k}$  for the electronic band structure of a perfect crystal, which is integrated over the Brillouin zone [46]. Seemann *et. al.* used this form of the anomalous Hall resistivity to successfully separate contributions to the AHE in FePt alloys [46]. In order to measure this experimentally, a Hall bar design is employed which allows simultaneous measurement of  $\rho_{xx}$  and  $\rho_{xy}$  under the influence of applied electric and magnetic fields; the magnetic field strength is varied and the linear contribution above  $\mu_0 M$  is subtracted to leave  $\rho_{xy}^{\text{AHE}}$  as in equation 2.27. Fig. 2.2a) shows a typical Hall bar, with  $H$  applied along  $n$ , the current applied along  $j$  and the Hall voltage measured along  $V_{\text{trans}}$ . Further detail on measuring the anomalous Hall effect is provided in chapter 3. The intrinsic contribution cannot be directly measured using dc techniques, but can be calculated then extracted. This is because the side-jump and intrinsic contributions do not have separate distinct identifiers in dc measurements; the side-jump term is independent of impurity concentration [76]. In ac measurements, the interband Hall resistivity can be extrapolated to zero frequency to give the intrinsic Hall resistivity. The scaling relation given in equation 2.27 is not always valid, however, and controversy remains over how to reliably separate the two extrinsic contributions; the quadratic dependence on the longitudinal charge resistivity is not always observed for systems where extrinsic spin-orbit scattering is expected; particularly in the case of disordered and/or dilute alloys [3; 45; 50; 56; 73; 80]. Though a new scaling has been proposed by Tian *et. al.* [50], this is dependent upon the use of a ferromagnetic system which allows for fabrication and measurement of a single crystal, leaving limitations for its applicability to non-magnetic systems doped with dilute amounts of impurities [45].

Within this thesis, dilute magnetic alloys will be considered, and these systems provide a method of studying in particular extrinsic scattering phenomena [49]. Dilute

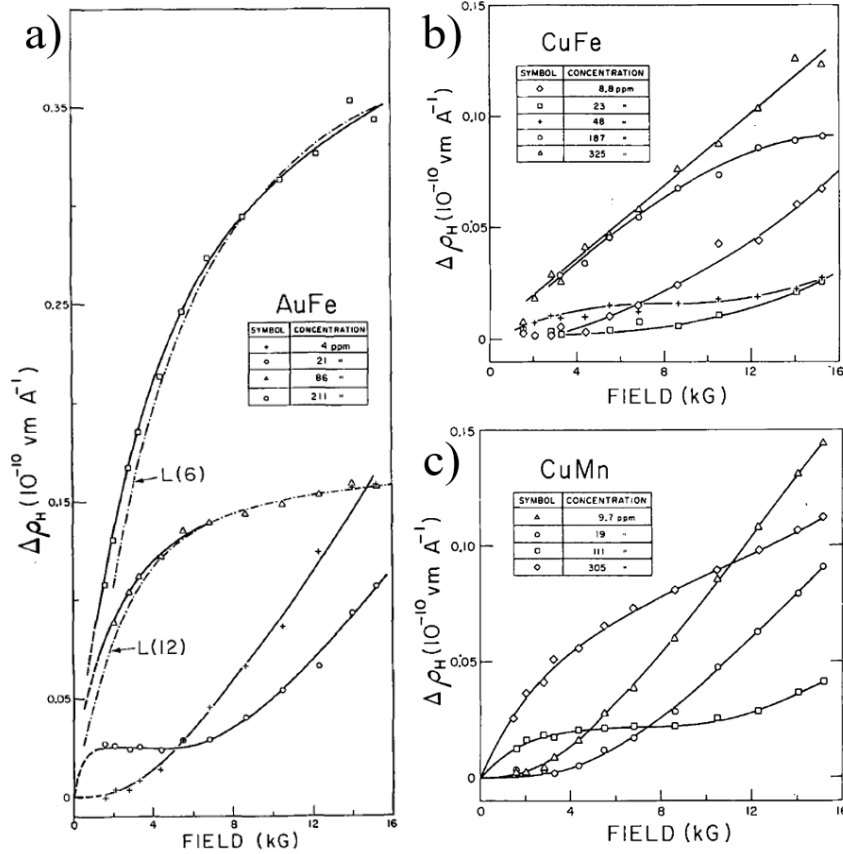


Figure 2.6: The change in Hall resistivity from the ordinary Hall resistivity for a) Au films with impurities of Fe, b) Cu films with impurities of Fe and c) Cu films with impurities of Mn in varying concentrations. The forms of Hall effect are comparable with types A, B and C shown in fig. 2.4b). Figure taken from [81].

magnetic impurities in Cu and Au have been shown to cause an anomalous Hall effect to appear, as shown in fig. 2.6, which is ascribed to skew scattering from impurity sites [68; 81]. An extensive experimental and theoretical study of the Hall effect in dilute magnetic alloys showed that only small amounts of magnetic impurities are required to produce an anomalous Hall response in non-magnetic metals, including in Pt [49; 79]. This is due to the large contribution of skew scattering and scattering with side jump to this phenomenon [3; 49; 63; 68; 79; 82–85]. These contributions can have the same or opposite signs, depending upon the choice of host and impurity. In systems like these, there is often no net magnetisation and so equation 2.25 with the conventional

---

## 2.4 The ordinary, anomalous and spin Hall effects

anomalous Hall coefficient  $R_{\text{AHE}}$  becomes inappropriate. Often an anomalous Hall angle  $\phi_{\text{AHE}} = \rho_{\text{AHE}}/\rho_0$  is discussed to avoid this issue, particularly in theoretical discussions [68; 82–84]. In this thesis, the concept used by Goennenwein *et. al.* for an AHE within a non-magnetic metal nominally free of impurities is used, as shown in fig. 2.2b) [58]. This is applicable for proximity effects and the spin Hall-anomalous Hall effect observed in YIG/Pt bilayers [58; 86]. We define a spontaneous Hall coefficient  $R_{\text{S}}$  which encompasses the magnetisation

$$\rho_{xy}(|H| > |H_{\text{sat}}|) = \mu_0 R_{\text{H}} H \pm R_{\text{S}} \quad (2.28)$$

where the Hall resistivity here defined is for fields where  $R_{\text{S}}$  is no longer varying with field. A positive sign is used for positive  $H$  and a negative sign for negative  $H$ . In fig. 2.2b) the label  $\alpha_{\text{AHE}}$  is shown for the anomalous Hall coefficient in a YIG/Pt bilayer; linear fits are used where  $\alpha_{\text{AHE}}$  becomes constant in field and the difference between their intercepts is halved to find the coefficient. The value of  $\alpha_{\text{AHE}}$  and its method of extraction is identical to that of  $R_{\text{S}}$  defined in equation 2.28. Spin glasses also exhibit spin-dependent scattering behaviour, known as spin scattering or the spin effect, which is not related to the spin-orbit interaction, but is due to the differing relaxation times for electrons with opposite spin [49; 65; 87–89].

### 2.4.3 The spin Hall effect

The spin Hall effect (SHE) was first theorised by D'yakonov and Perel in 1971 [7], but not given its popular name until 1999, when Hirsch coined the term [8]. In this Hall effect, a charge current is converted into a transverse spin current. A pure spin current involves electrons flowing in both directions, so there is no net flow of charge; however, opposite spins move in opposite directions, resulting in a net flow of spin. This concept is central to the field of spintronics [1], and much research is focused on the search for highly efficient spin Hall devices [4; 5; 10; 12; 14; 24–26; 90].

The inverse spin Hall effect was first observed in 1984 in a semiconductor [9]. In this effect, a spin current is converted into a transverse charge current, making this the main mechanism through which spin waves and spin currents are electrically detected,

## 2.4 The ordinary, anomalous and spin Hall effects

---

although optical methods are surfacing [91]. Fig. 2.2d) shows a lateral spin valve device which enables electrical detection of the inverse spin Hall effect. A spin current is injected into the normal metal channel by driving a current through a ferromagnetic spin injector (FM1) into the normal metal channel. The result of the inverse spin Hall effect is detected electrically via the voltage contacts displayed [5; 59]. The mechanisms governing both the spin Hall effect and its inverse are the same, consisting of an intrinsic contribution [92–97] and an extrinsic one [10–14; 16; 24–27; 44; 98–101]. Spin-orbit coupling is at the heart of this effect, and indeed the mechanics are the same as for the anomalous Hall effect: an intrinsic separation of spin, skew scattering and scattering with side jump. Spin Hall effects are observed in non-magnetic metals, where conduction electrons have no preferred spin. This means that no transverse voltage is detected from these effects, but a spin accumulation does occur. The efficiency of charge to spin current conversion in the spin Hall effect is characterised by the spin Hall angle, defined as

$$\theta_{\text{SH}} = \frac{\sigma_{yx}^s}{\sigma_{xx}} = \frac{\rho_{xy}^s}{\rho_{xx}} \quad (2.29)$$

where  $\theta_{\text{SH}}$  is the spin Hall angle,  $\sigma_{yx}^s$  is the spin Hall conductivity,  $\sigma_{xx}$  is the longitudinal charge conductivity  $\rho_{xy}^s$  is the off-diagonal element of the spin Hall resistivity tensor and  $\rho_{xx}$  is the charge resistivity [4; 14; 16]. Note that unlike the ordinary Hall angle, the spin Hall angle does not refer to a physical angle. Metals which exhibit large spin-orbit coupling, such as Au and Pt, exhibit larger spin Hall angles although typically only of a few percent [90; 93; 94; 102; 103]. In 2011, it was found that doping Cu, which has a low spin-orbit coupling, with dilute amounts of Ir impurities produces an extrinsic spin Hall effect [10]. This has led to a great deal of interest in extrinsic systems, with a number of theoretical and experimental studies to determine the optimum impurity system, showing impurity-dependent changes in sign of the spin Hall angle [10–12; 14; 16; 24–27]. It is of note that quantum confinement appears to enhance the effect of extrinsic impurities when they are positioned at the film surface, as found from experiment [27]. A discontinuous layer at a specific position within the device has been predicted to also affect the spin Hall angle in a position-dependent manner [16]. Fig. 2.7 shows the results from calculations for a discontinuous layer of Pt placed at varying positions within a gold spin Hall device. Here quantum confinement can also result from a transport effect and does not rely on thin layers. The

spin-dependent reflection of electron from an interface confines electrons to a particular layer, as in, for example, Fe/MgO tunnel junctions (an example of electronic confinement), as demonstrated by Dekadjevi *et. al.* in electron channelling in Fe/Au multilayers [104]. In the case of Pt confined within Au, scattering is reduced in the centre of the film, because there is a node where the antisymmetric wavefunctions cancel. At the edges of the film, there exists no solution and as such the scattering is once again reduced. The maximum scattering hence occurs for positions of delta layers in between the surface states and the centre of the film, as illustrated in fig. 2.7 [16]. The quantum confinement effect persists even for samples of 32 ML thickness; this equates to a film thickness of several nanometres. This lengthscale is much larger than for quantum wells used in semiconductor electronics, which are typically only a 2-5 nm in size [105]. Although the effect is small at this thickness, with  $\Delta\theta_{SH} \simeq 1\%$ , it was decided to explore the position dependence of high- $Z$  impurities within Cu; previous work had shown that such small changes could be measured for similarly  $\delta$ -doped samples in the giant magnetoresistance, with an interfacial lengthscale of around 25 Å for a variety of dopants [106]. A collaboration began with Dr. Martin Gradhand, who performed calculations to explain the results in the study on  $\delta$ -doping in the giant magnetoresistance, and agreed to calculate the changes for various impurities within a Cu host in the ordinary Hall effect. There has also been concern that effects such as the magnetic proximity effect, outlined in section 2.7, and the introduction of impurities and defects can actually suppress the spin Hall effect [98; 101; 107–109].

## 2.5 Spin Hall magnetoresistance

The seminal work on the spin Hall magnetoresistance (SHMR) was published in 2013 [17] and since then the phenomenon has attracted a lot of research interest [23; 110–119]. The system originally used to characterise the SHMR is a bilayer of a ferrimagnetic insulator, yttrium iron garnet ( $\text{Y}_3\text{Fe}_5\text{O}_{12}$ , YIG) and Pt, a metal known to possess high spin-orbit coupling [17]. Within non-magnetic metals, the conduction electrons experience a spin-dependent deflection in their motion due to spin-orbit coupling; this is the intrinsic spin Hall effect, as discussed in section 2.4.3. For very thin films, where the thickness is less than the spin diffusion length,  $\lambda_{sd}$ , this spin current persists to

## 2.5 Spin Hall magnetoresistance

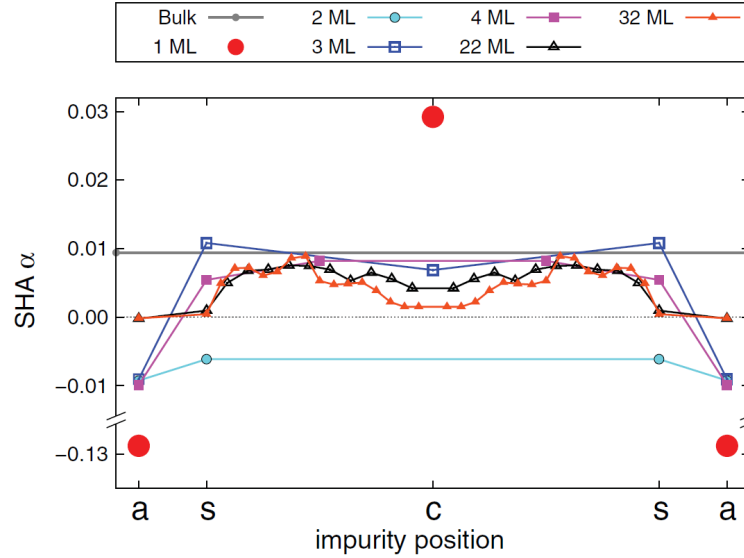


Figure 2.7: The calculated spin Hall angle as a function of position for a delta layer of Pt within a gold spin Hall device. This figure is taken from [16].

the edges of the film in the perpendicular orientation, as shown in fig. 2.8a). At the edges, the spin current is reflected back into the film, causing a spin current in the opposite direction to that generated; see fig. 2.8b). This spin current then generates a charge current through the inverse spin Hall effect, as shown in fig. 2.8c), which in turn generates a charge current parallel to that which is applied. In normal transport experiments, this cannot be verified, and it was unknown whether the spin Hall effect and its inverse did work together in this manner. Placing an insulating magnet at one of the film surfaces allows for control over the degree of spin current reflection at this interface, without complications from the charge current passing through the magnet. The mechanism of the SHMR is illustrated in such a bilayer system in fig. 2.8.

The insulating ferrimagnet possesses a net magnetisation  $\vec{M}$  which is aligned by the application of a magnetic field higher than the coercivity of the film. If  $\vec{M}$  is aligned perpendicular to the charge current, it is in parallel/antiparallel alignment with the spin polarisation of the electrons incident upon it from the generated spin current. The electrons with spin quantisation axes in other directions produce a negligible contribution to the conductivity of the material due to the sample geometry, since the width of the film is much greater than the depth [17]. In this scenario, the majority of the spin current is reflected from the interface and back into the metal, an example of confine-

## 2.5 Spin Hall magnetoresistance

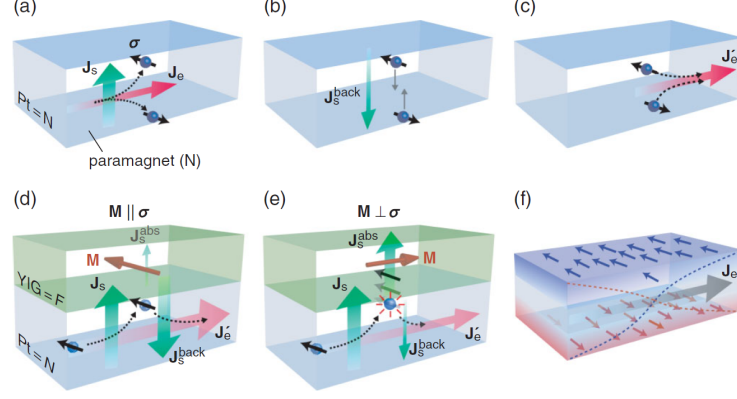


Figure 2.8: The mechanism of the spin Hall magnetoresistance is shown in a figure taken from [17]. In a), a spin current  $\mathbf{J}_s$  is generated via the spin Hall effect from an applied charge current  $\mathbf{J}_e$ . In b), this spin current is reflected at the film surfaces and converted into a parallel charge current in c). In d), the YIG layer has magnetisation  $\vec{M}$  parallel to the spin polarisation  $\sigma$ , which causes a large reflected spin current. In e),  $\vec{M}$  is perpendicular to  $\sigma$  and hence much of the spin current is absorbed as a spin wave. The accumulation of spins from the spin Hall effect in the metal is shown in f).

ment, as would be the case for a non-magnetic substrate. For the scenario where  $\vec{M}$  is parallel to the charge current and hence perpendicular to the spin polarisation, the result is quite different. In this case, the spin current is able to pass into the insulator via a transfer of spin angular momentum and continue as a spin wave. This results in the minimum reflection of the spin current back into the metal. This effect gives rise to the SHMR: the resistance of the metal is found to be higher when  $\vec{M}$  is parallel to the charge current than when it is perpendicular [17]. The magnitude of the SHMR is calculated as follows

$$\frac{\Delta\rho_1}{\rho_0} = \theta_{\text{SH}}^2 \frac{\lambda_{\text{sd}}}{d_N} \frac{2\lambda_{\text{sd}}G_r \tanh^2 \frac{d_N}{2\lambda_{\text{sd}}}}{\sigma + 2\lambda_{\text{sd}}G_r \coth \frac{d_N}{\lambda_{\text{sd}}}} \quad (2.30)$$

where  $\Delta\rho_1$  is the change in resistivity between the two magnetisation orientations,  $\rho$  is the resistivity of the film while  $\sigma$  is its conductivity,  $\rho_0$  is the resistivity in zero field,  $\theta_{\text{SH}}$  is the spin Hall angle,  $\lambda_{\text{sd}}$  is the spin diffusion length,  $d_N$  is the thickness of the film, and  $G_r$  is the real part of the spin mixing conductance [17; 113]. The spin mixing conductance represents the number of spin transport channels per unit area at the interface between the metal and insulator. It is strongly dependent upon the quality of

the interface and of the YIG film. This concept will be explored further in section 2.9.

Another phenomenon has been predicted to arise as a consequence of the spin mixing conductance between the magnetic insulator and normal metal layer; this is the spin Hall-anomalous Hall effect (SHAHE), shown in fig. 2.2b) [58; 113]. Unlike the SHMR, which depends only on the real part of the spin mixing conductance  $G_r$ , this is thought to originate from the imaginary part of the spin mixing conductance  $G_i$ . The spin accumulation discussed in section 2.5 contains a small component which scales with the magnetisation out of the plane of the magnetic insulator. This component leads to a transverse charge current and hence the SHAHE, which saturates when the magnetic layer of the YIG saturates out of the plane [113].

## 2.6 Quantum interference

Quantum interference in disordered conductors results in corrections to the resistivity as a function of both temperature and applied magnetic field. In this thesis, quantum interference and electron-electron interaction effects are considered in a two dimensional disordered conductor. The relative change in conductivity has two contributions

$$\frac{\Delta\sigma}{\sigma} = \frac{\Delta D}{D} + \frac{\Delta g(E)}{g(E)} \quad (2.31)$$

where  $D$  is the diffusion constant and  $g(E)$  the density of states [120]. The first term is a result of localisation while the second is from the electron-electron interaction [120].

### 2.6.1 Temperature dependence

Quantum interference is a phenomenon which can increase or decrease the resistivity of disordered conductors at low temperatures. An electron in state  $k$  undergoes a scattering event at  $t = 0$ ; multiple scattering events occur with intermediate states  $k'_i$  until the state  $k'$  is reached. There is a finite probability that the state  $k'$  has the same physical coordinates as the state  $k$ , in which case the electron is said to have

undergone back-scattering to its original position and the partial wavefunctions are superimposed. Constructive interference relies on phase coherence which can only occur when the scattering is elastic since

$$\phi = \frac{Et}{\hbar} \quad (2.32)$$

where  $\phi$  is the phase change and  $E$  is the associated energy change of the electron wave for a scattering event lasting time  $t$ . Elastic scattering must therefore be more prevalent than inelastic scattering within the conductor for quantum interference to have a measurable effect on the conductivity of the sample. This typically occurs at low temperatures, where the elastic scattering lifetime  $\tau_0$ , which tends to govern scattering events from static sites, can be much shorter than the inelastic lifetime  $\tau_i$ . Inelastic collisions are prevalent at higher temperatures where electron-phonon scattering dominates the resistivity and  $\tau_i$  is hence much shorter. Phase coherence is lost between the partial waves after a phase breaking time  $\tau_\phi$  which can be defined as being equivalent to  $\tau_i$  [121–123].

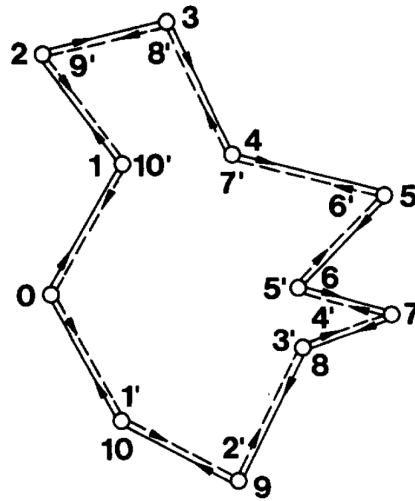


Figure 2.9: Two paths of a single electron, as partial waves, are illustrated by full and dashed lines; the electron traverses both of these paths and constructive interference occurs at the origin, labelled 0. Each open circle represents a scattering site in real space in a disordered conductor. Figure taken from [123].

Weak localisation is a phenomenon where the probability of coherent back-scattering is increased by a factor of two. Considering the scattering sequence illustrated in fig. 2.9, the incoming electron has initial wavefunction  $\psi$  with amplitude  $A$  and wavevector  $\vec{k}$ . Two paths are illustrated for the electron to return to the origin, with amplitudes  $A'$  and  $A''$  and wavefunctions  $\psi_1$  and  $\psi_2$  respectively. In the case where the electron returns to the origin,  $A = A' = A''$  and the probability of back-scattering is given by

$$P = \psi_1^2 + \psi_2^2 + \psi_1^* \psi_2 + \psi_1 \psi_2^* = |A'|^2 + |A''|^2 + A'^* A'' + A' A''^* = 4|A|^2 \quad (2.33)$$

where the cross terms represent the interference terms. Without constructive interference, therefore, the intensity would be  $2|A|^2$ , as the interference terms vanish, meaning that back-scattering is twice as probable when the scattered waves are coherent with probability  $4|A|^2$ . It is of note that this enhancement of the probability only applies for the electron scattering back to the origin; scattering to states further away from this have incoherent superposition leading to an average intensity of  $|A|^2$ . This enhanced probability of finding the electron at the origin of a scattering sequence leads to a quantum correction to the classical Boltzmann conductivity, observed as an increase in the resistivity at low temperatures [124] as well as an additional contribution to the magnetoresistance [125; 126]. The quantum correction to the conductance per square for a two dimensional metal at low temperatures, when electron-electron scattering is not the dominant scattering mechanism, has been found to be

$$\sigma = \sigma_0 - \Delta\sigma_{\text{WL}} + \Delta\sigma_{\text{so}} = \frac{ne^2\tau_0}{m_e} - \left(\frac{e^2}{2\pi^2\hbar}\right) \ln\left(\frac{\tau_1}{\tau_0}\right) + \frac{\alpha e^2}{2\pi^2\hbar} \frac{3}{2} \ln\left(1 + \frac{4\tau_1}{3\tau_{\text{so}}}\right) \quad (2.34)$$

by Anderson *et. al.* [127] and Gorkov *et. al.* [128] for  $\Delta\sigma_{\text{WL}}$  and by Maekawa *et. al.* [129] and Abraham *et. al.* [130] for  $\Delta\sigma_{\text{so}}$  where  $\sigma$  is the total conductance per square,  $\sigma_0 = ne^2\tau_0/m_e$  is the free electron conductance per square for a sample of the same thickness as  $\Delta\sigma$ , with  $\tau_0$  being the electron lifetime for potential scattering and  $n = 2\pi k_{\text{F}}^2/(2\pi)^2$ .  $\Delta\sigma_{\text{WL}}$  represents the quantum correction to the conductance per square for weak localisation without the contribution from spin-orbit coupling, and this relies upon the inelastic scattering lifetime  $\tau_1$ . The parameter  $\alpha$  describes the interaction between electrons; it is found to have a value of unity in the limit of strong spin-orbit scattering [129; 130]. The term  $\Delta\sigma_{\text{so}}$  comes from strong spin-orbit coupling and generates a positive correction to the conductance per square, with  $\tau_{\text{so}}$  being the

lifetime for spin-orbit scattering. The only temperature dependent term in the conductance per square correction is  $\tau_i$  with  $\tau_0$  and  $\tau_{so}$  remaining independent of temperature [123; 127–130].

In the case of very strong spin-orbit coupling, and hence a very small value of  $\tau_{so}$ , the phenomenon of weak anti-localisation occurs [121; 123]. During spin-orbit scattering, the spin is altered during each scattering event, breaking the phase coherence between partial scattered waves and resulting in destructive interference at the origin. This results in a positive correction to the conductivity at very low temperatures [123]. The differences in the magnetoresistance between weak localisation and weak anti-localisation are displayed in fig. 2.10 and discussed below.

Another correction to the low temperature resistivity in disordered metals can come from an enhanced electron-electron interaction. Below a temperature  $T_0$ , a reduction in conductivity has been observed, deviating from the expected Drude conductivity [121; 123; 124; 127; 128; 131; 132]. This is the limit where  $\tau_0 \ll \tau_i$  and quantum interference effects are observed. Inelastic scattering can take many forms, but in relatively clean metals below liquid helium temperatures the electron-electron interaction is a contributor. In disordered metals where the transport is more diffusive, electron-electron interactions are enhanced [123; 131–133]. The lifetime associated with the electron-electron interaction can be expressed as

$$\frac{1}{\tau_{ee}} \simeq v_F K_S \left( \frac{k_B T}{E_F} \right)^2 \quad (2.35)$$

where  $\tau_{ee}$  is the electron-electron lifetime,  $v_F$  is the Fermi velocity,  $K_S$  is the magnitude of the Thomas-Fermi screening wave-vector,  $k_B$  the Boltzmann constant,  $T$  the temperature and  $E_F$  the Fermi energy [133]. The electron-electron interaction is described by the Landau theory of Fermi liquids [120; 134]. When an electron is excited above the Fermi energy, it takes the time  $\tau_{ee}$  to relax to its original state. This is true even in clean metals, and equation 2.35 represents the general case where an electron excited by  $k_B T$  above the Fermi energy is returned to  $E_F$  after  $\tau_{ee}$  [120]. In a disordered system, the transport is diffusive and  $\tau_{ee}$  is reduced; the scattering rate is larger and hence its contribution to the conductivity larger, as per Matthiesen's rule, equation 2.1. This

is the enhanced electron-electron interaction. More generally, the inelastic lifetime has a power law dependence on the temperature

$$\tau_i \propto T^{-P} \quad (2.36)$$

where  $P \approx 1$  for weakly localised electrons in a two-dimensional metal and  $P \approx 2$  for transport dominated by the electron-electron interaction in a clean metal in two dimensions or for a three dimensional sample in the dirty regime [120; 121; 123; 133; 135; 136]. Generally,  $\tau_i$  can be said to depend on temperature as follows

$$\frac{1}{\tau_i} = A_1 T + A_2 T^2 \quad (2.37)$$

where  $A_1$  and  $A_2$  are constants.

When the electron-electron interaction is the dominant mechanism contributing to  $\tau_i$  and spin-orbit scattering is absent, a correction to the conductance per square, as calculated by Altshuler *et. al.* [125; 131] is observed as follows

$$\Delta\sigma = \frac{e^2}{2\pi^2\hbar} (1 - F) \ln\left(\frac{T}{T_0}\right) \quad (2.38)$$

where  $T_0$  is the temperature where minimum resistivity occurs,  $F$  is a screening factor such that  $0 \leq F \leq 1$  and the total conductance per square is given by  $\sigma = \sigma_0 + \Delta\sigma$ . The temperature-dependent conductance per square corrections for both weak (anti-)localisation and enhanced electron-electron interaction are hence both logarithmic in temperature.

In the region where these effects play a role in the resistivity, they are also expected to play a role in the Hall coefficient, with

$$\frac{\Delta R_H}{R_H} = -2 \frac{\Delta\sigma_{\text{int}}}{\sigma} = 2 \frac{\Delta\rho_{\text{int}}}{\rho} \quad (2.39)$$

where  $\Delta\sigma_{\text{int}}$  and  $\Delta\rho_{\text{int}}$  are the changes in conductivity and resistivity due to interaction effects [33].

### 2.6.2 Field dependence

In a sample with magnetic impurities, the phase coherence is destroyed during each scattering event, which in turn weakens or destroys the observable resistivity phenomena. Application of a magnetic field also has the same effect, to the extent that both weak localisation and weak anti-localisation are destroyed with the application of large magnetic fields [121]. This is demonstrated by the data in fig. 2.10.

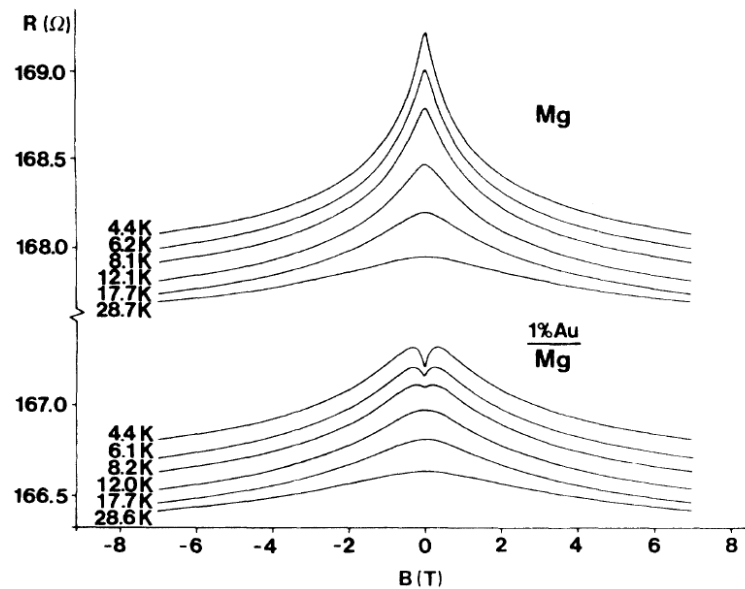


Figure 2.10: The perpendicular magnetoresistance for a disordered film of Mg exhibits weak localisation at low temperatures, while below the inclusion of 1 % of a monolayer of Au impurities produces weak anti-localisation. This figure is taken from [121].

As can be seen in fig. 2.10, weak localisation causes a sharp negative magnetoresistance at low fields and low temperatures. Over a relatively small temperature range, this feature is seen to reduce before disappearing above the weak localisation regime. The sample in question consists of a highly disordered film of Mg, which exhibits low spin-orbit coupling. In the lower portion of the figure, a similar Mg film is considered, but doped with 1 % of a monolayer (ML) of Au, which has a high spin-orbit coupling. In this sample, weak localisation is destroyed to be replaced by weak anti-localisation, which manifests as a sharp positive magnetoresistance at low fields. This effect is also

observed to reduce in magnitude before the magnetoresistance becomes normal above the regime of quantum corrections, in both temperature and applied magnetic field [121; 122]. The magnetoresistance due to weak (anti-)localisation is given by

$$\Delta\sigma(B) = -\frac{e^2}{2\pi^2\hbar} \left[ \Psi\left(\frac{1}{2} + \frac{B_1}{B}\right) - \Psi\left(\frac{1}{2} + \frac{B_2}{B}\right) + \frac{1}{2}\Psi\left(\frac{1}{2} + \frac{B_3}{B}\right) - \frac{1}{2}\Psi\left(\frac{1}{2} + \frac{B_4}{B}\right) \right] \quad (2.40)$$

where  $\Delta\sigma(B)$  is the change in conductivity at applied field  $B$ ,  $\Psi$  is the digamma function and the fields  $B_n$  are given by

$$B_1 = B_0 + B_{so} + B_s \quad (2.41)$$

$$B_2 = \frac{4}{3}B_{so} + \frac{2}{3}B_s + B_i \quad (2.42)$$

$$B_3 = 2B_s + B_i \quad (2.43)$$

$$B_4 = \frac{4}{3}B_{so} + \frac{2}{3}B_s + B_i \quad (2.44)$$

where  $B_0$  is the characteristic field for potential scattering,  $B_{so}$  for spin-orbit scattering,  $B_s$  for magnetic scattering and  $B_i$  for inelastic scattering. These characteristic fields are related to the characteristic lifetimes  $\tau_n$  via

$$B_n\tau_n = \frac{\hbar}{4eD} \quad (2.45)$$

where  $D$  is the elastic diffusion constant [123].

The electron-electron interaction also has an impact on the observed magnetoresistance, although it is typically much smaller than for weak (anti-)localisation [123; 137]. The relative change in conductivity was calculated by Lee and Ramakrishnan [137] in the limit of exceptionally small spin-orbit coupling. Two limits were found

$$\frac{\Delta\sigma}{\sigma_0} = \begin{cases} \frac{l}{A} \frac{F}{2} 0.084h^2 & \text{for } h \ll 1 \\ \frac{l}{A} \frac{F}{2} \ln\left(\frac{h}{1.3}\right) & \text{for } h \gg 1 \end{cases} \quad (2.46)$$

where  $l$  is the length measured,  $A$  the cross-sectional area,  $F$  the screening factor and  $h = g\mu_B H / (k_B T)$ . For strong spin-orbit coupling, the magnetoresistance is found to vanish [137].

Quantum interference is thought to have an effect on the ordinary and anomalous Hall effects, although this is not always the case experimentally [45; 138–140]. For the ordinary Hall effect, the electronic relaxation time develops a logarithmic dependence on the temperature, leading to the relative change in the Hall conductivity

$$\frac{\Delta\sigma_{xy}}{\sigma_{xy}} = 2 \frac{\Delta\sigma_{xx}}{\sigma_{xx}} \quad (2.47)$$

where  $\sigma_{xy}$  is the Hall conductivity,  $\sigma_{xx}$  the longitudinal conductivity and  $\Delta\sigma$  is the change in each respective conductivity at low temperatures due to quantum interference [138; 140]. This scaling has been shown to break down in a number of cases, however; whilst high resistivity was initially thought to be the cause [140], it has been shown to be true where this is not the case [45; 139]. The enhanced electron-electron interaction is not thought to have an effect on the ordinary Hall resistivity [125]. For the anomalous Hall effect, a similar change has been observed in the literature, where

$$\Delta^N \sigma_{xy}^{\text{WL}} = \frac{\sigma_{xy}^{\text{SSM}} \ln(T/T_0)}{(\sigma_{xy}^{\text{SSM}} + \sigma_{xy}^{\text{SJM}})} \quad (2.48)$$

is the correction, which is hence also logarithmic in nature [45; 138; 139]. In equation 2.48  $\Delta^N$  represents the normalised change in  $\sigma_{xy}^{\text{WL}}$  the Hall conductivity due to quantum interference.  $T$  is the temperature, whilst  $T_0$  is the highest temperature where quantum interference begins to take effect. The labels SSM and SJM represent the Hall conductivity due to skew scattering and side-jump, respectively. This has also later been shown to be non-universal, however [45; 139].

## 2.7 Magnetic proximity effect

The magnetic proximity effect (MPE) is known to enhance magnetic moments for some dilute alloy and multilayer systems [141–143]. The Stoner criterion outlines what is required for spontaneous ferromagnetic ordering, and thus the emergence of ferromagnetism within a metal [144; 145], and is formulated as

$$Ug(E_{\text{F}}) \geq 1 \quad (2.49)$$

where  $U$  is the exchange integral,  $g(E_F)$  is the density of states at the Fermi level and  $E_F$  is the Fermi energy. The transition metals iron, cobalt and nickel satisfy this criterion at room temperature, making them ferromagnetic. Some metals come close to satisfying this criterion, but do not exhibit ferromagnetic phenomena in isolation; Pt is one such candidate [143]. Through the mechanism of exchange coupling, a ferromagnet adjacent to platinum can induce ferromagnetism over a short range in the non-magnetic metal, as has been found for multilayers of Ni and Pt [143]. The effect was first found in 1960 for alloys of palladium and iron, where a larger than expected magnetic moment was discovered for the dilute amount of magnetic impurities present [141]. Exchange coupling between electrons in the ferromagnet and in the normal metal enhance the exchange integral and cause the local Pd atoms to obtain ferromagnetic order; this is the essence of the MPE [141–143]. In section 2.9 the possibility of an MPE between the oxide YIG and Pt is discussed.

## 2.8 The Kondo effect

It has already been discussed that an increase in resistivity can be observed at very low temperatures in disordered or confined systems due to quantum interference [121]. Another cause of a low temperature increase in resistivity is the Kondo effect [146]. This increase in the resistivity is a consequence of dilute amounts of magnetic impurities being present within a non-magnetic film, making this a useful phenomenon for experimentally testing the purity of certain metals. A magnetic impurity has a localised magnetic moment which interacts with the spin of the conduction electrons via the exchange interaction [146–149]. This results in a scattering of the itinerant conduction electron which changes its spin. At low temperatures, where phonon scattering is negligible, this becomes the dominant contribution to the resistivity in dilute magnetic alloys, resulting in the increased resistivity observed. An example of some resistivity minimum data is shown in fig. 2.11.

The position of the minimum is strongly dependent upon the concentration of mag-

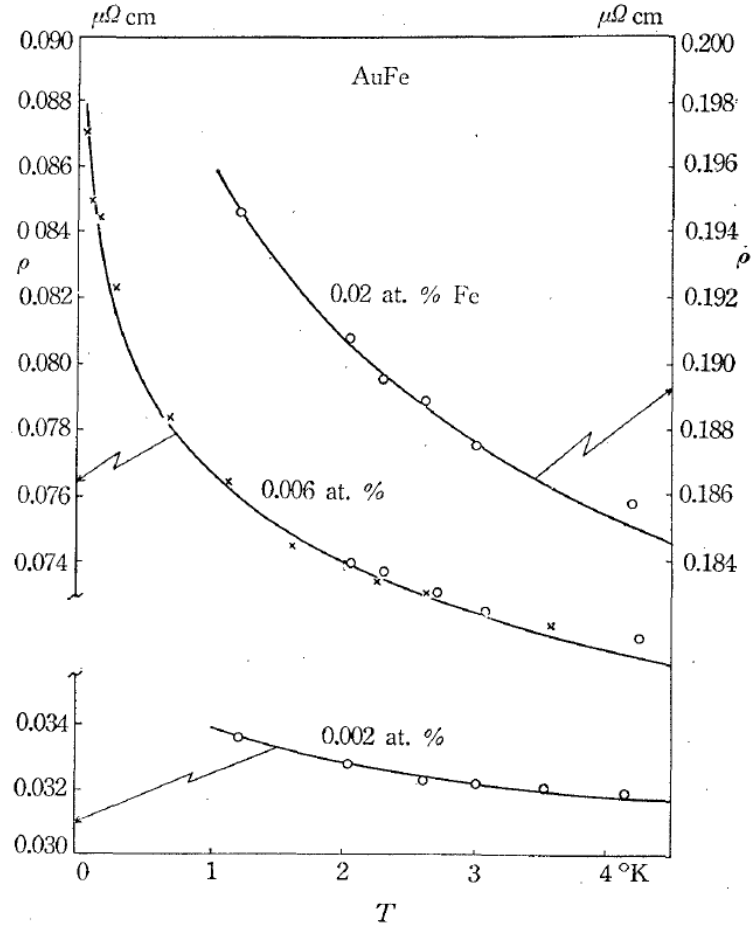


Figure 2.11: The resistivity as a function of temperature for varying concentrations of Fe within Au, to illustrate the change in the resistivity minimum with concentration. The points represent the experimental data while the lines represent the theory. This figure is taken from [146].

netic impurities, and is described by the relation found by Kondo [146] as

$$\rho = aT^5 + c\rho_0 - c\rho_1 \ln T \quad (2.50)$$

where  $\rho$  is the resistivity at temperature  $T$ ,  $a$  is a phenomenological constant found from experiment,  $\rho_0$  and  $\rho_1$  are components of the resistivity from intrinsic and extrinsic sources respectively, and  $c$  is the concentration of magnetic impurities [146; 150]. This logarithmic dependence can be observed in fig. 2.11; although the actual position of  $T_{\min}$  is not shown, the strong change in gradient between the three curves shows

## 2.9 Magnetotransport in YIG/metal bilayers

---

a strong concentration dependence. The temperature of the resistance minimum is dependent upon the concentration of impurities as follows

$$T_{\min} = \left(\frac{\rho_1}{5a}\right)^{\frac{1}{5}} c^{\frac{1}{5}} \quad (2.51)$$

where  $T_{\min}$  is the temperature at which the resistivity minimum occurs [146; 147; 150]. In practice, it is often difficult to extract a concentration from experimental data of the resistivity as a function of temperature, and further phenomenological relations for particular systems are often employed [98; 148; 151–153]. An example of this is some of the recent Kondo research in lateral spin valves consisting of Cu with Fe impurities by O’Brien *et. al.* [153] which uses another form of phenomenological relation found by Goldhaber-Gordon *et. al.* [152], while Batley *et. al.* [98] used a simpler relation found by NASA scientists to be applicable for the CuFe system [151]. Another approach to the problem exists in theoretical models which utilise different approaches for resistivities below and above  $T_{\min}$  with varying success [154–158]. Another important parameter is the Kondo temperature  $T_K$  which for some systems can be above room temperature; below this temperature the Kondo effect is screened [146; 147; 149; 159].

## 2.9 Magnetotransport in YIG/metal bilayers

Bilayers of YIG and metals with high spin-orbit coupling have proved systems of great interest since the discovery of the SHMR and the promise of the spin Seebeck effect, but conflicting results have emerged in the literature regarding interfacial phenomena. YIG is a material which can be fabricated in many different ways, the most common being liquid phase epitaxy (LPE), pulsed laser deposition (PLD) and radio frequency magnetron sputtering. The production of a bilayer of YIG and a metal can be facilitated in different ways, with some groups opting for a clean *in-situ* method of metal deposition immediately after YIG deposition [20; 58; 160]. Not all YIG growth facilities possess this functionality, and so the YIG surface can be cleaned prior to the deposition of further material [21; 110; 112; 161]. Studies have been performed which show that etching the YIG surface with argon ions or with an etching solution improves the spin mixing conductance for metals later deposited on top [18; 19]. However, bombardment

## 2.9 Magnetotransport in YIG/metal bilayers

---

of a YIG film with ions prior to the deposition of Pt has been shown to increase MPE-related magnetotransport effects [23], raising questions about the validity of etching as a process which solely increases the spin mixing conductance [162].

Since the seminal work on the SHMR [17], care has been taken to separate the phenomenon from a potential MPE from the magnetic insulator, which may contribute to the observed phenomenon. X-ray magnetic circular dichroism (XMCD) measurements are able to resolve the magnetic polarisation in individual layers and thus detect any MPE [143]. Various groups have performed these measurements in YIG/Pt bilayers, with varying results. Some data show a magnetic polarisation in Pt [21; 163] whilst other data show an absence of this magnetic signal [20]. The magnetotransport phenomena measured also show discrepancies, with some data showing phenomena which can only be explained by interfacial magnetism [21–23; 112] and other data showing otherwise [58].

The anomalous Hall effect is a particularly sensitive mechanism of detecting moments from dilute amounts of magnetic impurities [49; 85; 88]. In YIG/Pt bilayers, an anomalous Hall effect manifests with drastically different field dependence observed by different groups [23; 58; 112]. Some representative data are shown in fig. 2.12. In fig. 2.12a), a non-linear Hall effect is observed which changes sign as a function of temperature. The curvature extends to fields higher than typical YIG saturation in an out of plane field. The magnitude of the anomalous Hall resistivity increases if the YIG has been bombarded with ions, indicating the strong effect of interface preparation on the observed AHE. Qualitatively, a very similar trend is observed for the same thickness of Pt deposited on Fe-doped SiO<sub>2</sub>, and this is not quantitatively dissimilar from that observed for ion bombarded YIG. It is reported that x-ray photoelectron spectroscopy (XPS) measurements of the ion bombarded YIG show a metallic Fe state at the surface [23]. Fig. 2.12b) shows the anomalous Hall effect observed by another group for YIG/Pt bilayers [112]. In this case, the Pt is of thickness 2 nm rather than the 3 nm reported upon in fig. 2.12a). High field curvature is also observed in this case, with a change in sign and a shape not dissimilar to that observed in fig. 2.12a). The magnitude of the Hall resistance is an order of magnitude smaller, however. At 300

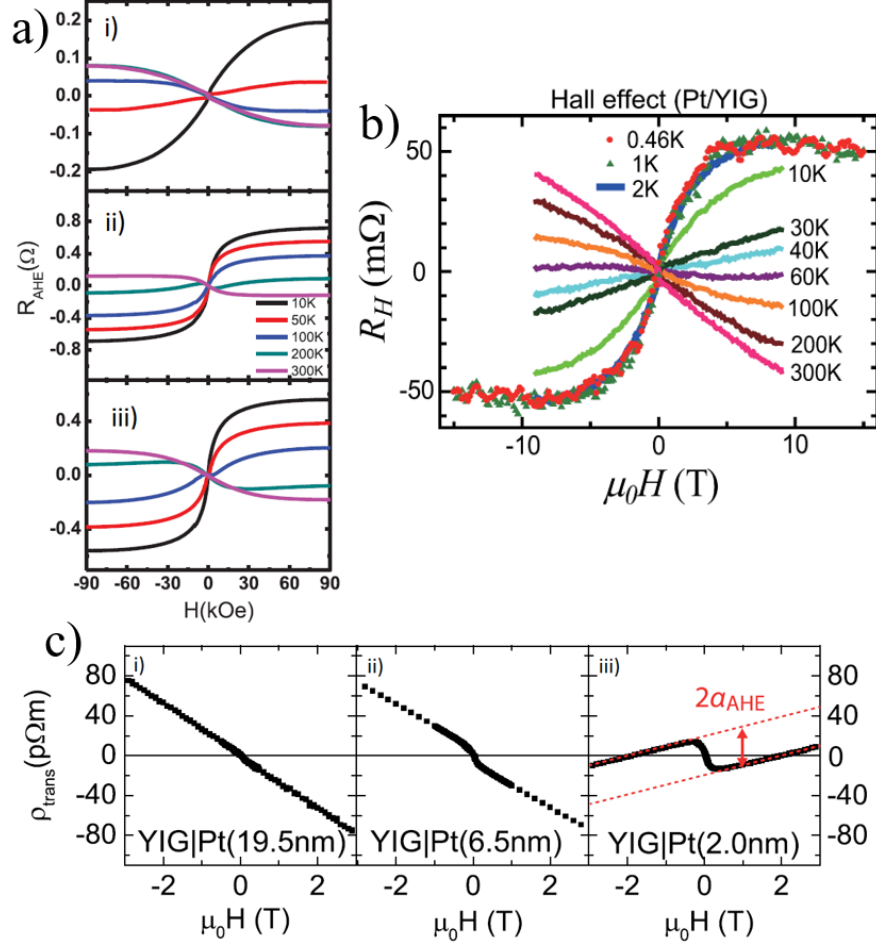


Figure 2.12: Examples of the Hall effect in YIG/Pt bilayers observed in the literature. The data in a) are taken from [23] and show the anomalous Hall resistance as a function of applied field for i) YIG/3 nm Pt, ii) YIG<sub>BB</sub>/3 nm Pt, where YIG<sub>BB</sub> represents ion bombarded YIG, and iii) SiO<sub>2</sub> (7% Fe)/3 nm Pt. The data in b) are taken from [112] and show the Hall resistance as a function of field for YIG/2 nm Pt. The data in c) are taken from [58] and show the Hall resistivity for YIG/Pt bilayers with Pt of thickness i) 19.5 nm, ii) 6.5 nm and iii) 2.0 nm, all measured at 300 K. Actual figures modified from [23; 58; 112].

K, another phenomenon is observed at low field, with a sharp change in the Hall resistance. A similarly sharp central feature is also observed in fig. 2.12c)iii) for 2 nm Pt deposited on YIG [58]. The two groups show a difference in sign for the gradient of the Hall resistance above this central phenomenon, however. The data at larger thickness of Pt in fig. 2.12c) show a reduced central effect, and a change in sign of the ordinary

## 2.9 Magnetotransport in YIG/metal bilayers

Hall effect at fields above this, returning to a negative normal metallic response. A qualitatively similar AHE is shown in fig. 2.13. This AHE is due to the MPE between a gated ionic liquid and an ultrathin Pt film. By varying the voltage applied to the ionic liquid, varying amounts of MPE are induced in the Pt and hence the AHE can be tuned [86].

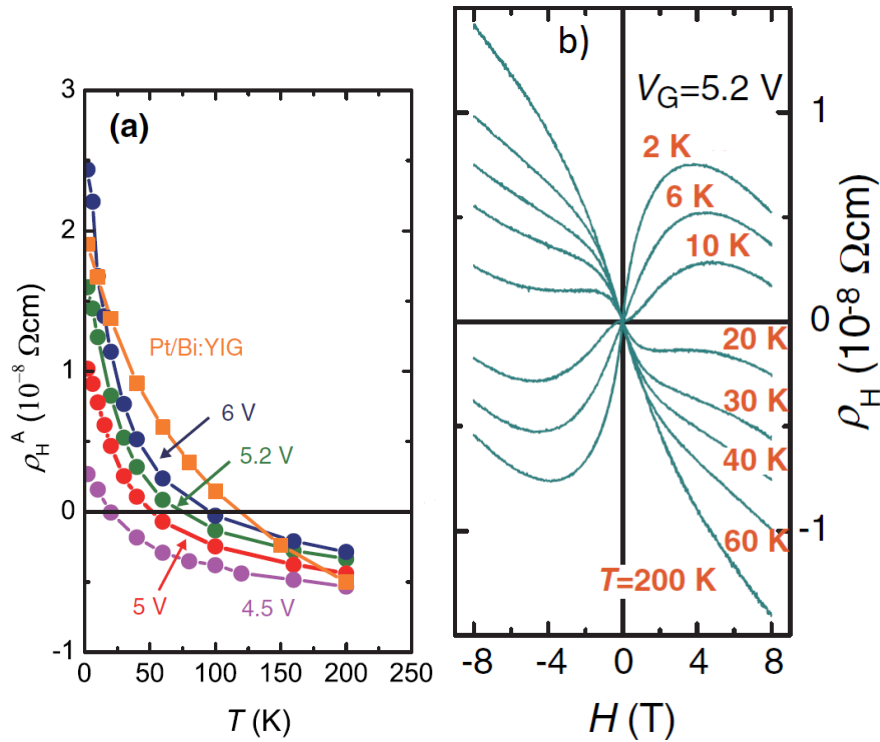


Figure 2.13: *The anomalous Hall effect in Pt induced by the magnetic proximity effect from an adjacent gated ionic liquid. The temperature dependence of the anomalous Hall resistivity at an applied field of 8 T is shown in a), whilst b) shows the Hall resistivity as a function of applied field. Figure taken from [86].*

There are hence two forms of the anomalous Hall effect observed in YIG/Pt bilayers: one shows curvature to high fields and hence has its origins in interfacial phenomena, whilst the other occurs at low fields and owes its origins to the spin mixing conductance and SHMR. This lower field component is known as the spin Hall-anomalous Hall effect (SH-AHE) and has been theoretically predicted as a consequence of the SHMR and the imaginary component of the spin mixing conductance,  $G_i$  [113]. The

## 2.9 Magnetotransport in YIG/metal bilayers

presence of interfacial magnetic phenomena has also been surmised from further magnetotransport measurements, with an anisotropic magnetoresistance (AMR) appearing in some reported data at low temperatures [118; 162]. Some of this data is represented in fig. 2.14.

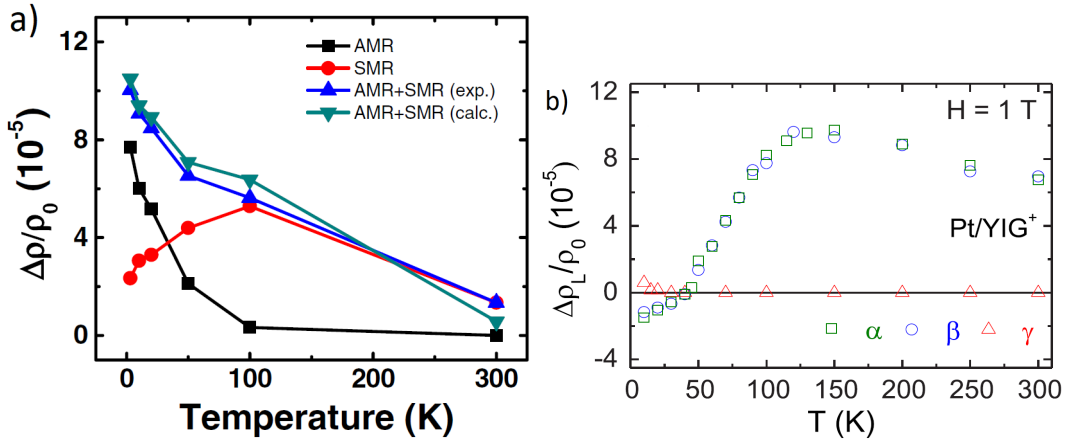


Figure 2.14: Representative angular dependent magnetoresistance data for YIG/metal bilayers from the literature. In a), data are shown for YIG/2 nm Pd in the  $\alpha$  (labelled AMR+SMR),  $\beta$  (labelled SMR) and  $\gamma$  (labelled AMR) planes, taken from [118], whilst in b) data are shown for 7 nm Pt deposited on YIG which has been surface treated with an  $\text{Ar}^+$  ion milling process, taken from [162].

An AMR is found at low temperatures in both Pd and Pt deposited on YIG [118; 162]; both are metals close to satisfying the Stoner criterion and are therefore susceptible to the MPE. The temperature dependence of the SHMR is very different in both cases due to the different metals in use. The data in fig. 2.14b) for Pt agrees with the shape previously shown for YIG/Pt [110]. A similar low temperature AMR has been observed for Ta on YIG [164]. This metal is much further from satisfying the Stoner criterion, however; as can be seen from work in chapter 6 the surface of the YIG plays a large role in magnetotransport. It is the view of the candidate that the observed effect is therefore more likely to be the result of localised interfacial magnetic impurities rather than a bulk MPE. To remove any contribution from the MPE completely, measurements have been taken for systems involving Rh [116] where the

## 2.9 Magnetotransport in YIG/metal bilayers

---

SHMR still persists.

From recent literature, it seems clear that interfacial magnetism in YIG/metal bilayers plays a role in their magnetotransport [23; 112] and that the spin mixing conductance leads to a SH-AHE in some reported systems [58; 112]. The large field effects show similarities to those observed for the MPE within Pt for the AHE [86]. The method of preparation for both the YIG film and any surface treatments applied to it could be the cause of the variation in results reported in the literature.

---

# CHAPTER 3

---

Experimental methods

### 3.1 Introduction

Throughout the course of this work, a variety of experimental methods have been employed, from fabricating samples to measuring their properties under various conditions. Within this chapter, the principles of sample preparation and measurement techniques are described.

### 3.2 Material fabrication

This project has required the fabrication of many samples, consisting of thin films of both metallic elements and of the magnetic insulator YIG. The metallic thin films were fabricated by direct current (dc) magnetron sputtering, while YIG was prepared by radio frequency (rf) magnetron sputtering; in the following subsections, these processes will be discussed in detail.

#### 3.2.1 Direct current magnetron sputtering

Direct current (dc) magnetron sputtering is a relatively inexpensive technique for fabricating thin metallic films of high quality. A metallic target of high purity is placed atop an assembly of magnets, of which a schematic is shown in fig. 3.1. The target is electrically isolated from a surrounding shield and from the substrate. Deposition occurs in a chamber which is first evacuated to become a high vacuum (HV) environment with a base pressure of around  $3 \times 10^{-8}$  Torr. To achieve such a low pressure, the sputtering chamber is first evacuated by a rotary pump from atmospheric pressure to  $10^{-3}$  Torr. Following this, a cryogenic pump is used to lower the pressure to around  $1 \times 10^{-7}$  Torr. At this stage, the majority of molecules forming this pressure are water molecules, as determined by using a residual gas analysis method of mass spectrometry. To reduce the gas pressure to HV levels, liquid nitrogen flows around a coil of copper pipe towards the top of the chamber; this design is known as a Meissner trap and condenses water vapour onto the pipe. Maintaining HV conditions during a growth is essential to provide high quality thin metallic films with a minimum of defects; hence the Meissner

trap is maintained throughout the growth.

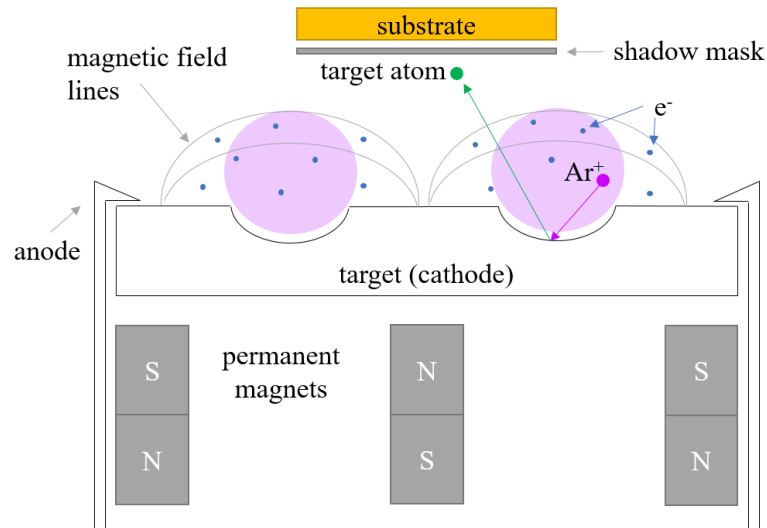


Figure 3.1: A schematic of the mechanism for dc magnetron sputtering. The light purple circles represent the Argon plasma which is confined above the racetrack on the target.

In order to sputter material onto the substrate, an inert gas must be introduced to the system. For the deposition of most metals in this project, solely argon is used, at a flow rate of 24 SCCM (standard cubic centimetres per minute) to a pressure of 2.4 mTorr. A negative dc bias is then applied to the target, making this the cathode and the metal housing the effective anode, as this is electrically grounded. The atoms of argon surrounding the target then become positively charged ions, which bombard the target and eject metal ions from its surface. These metal ions then travel to and deposit onto the substrate. A series of magnets beneath the target confine the plasma to the local area of the target, raising the number of collisions and hence the growth rate of the target material. The design is shown in fig. 3.1. The concerted actions of a confined plasma and very low pressure cause the ejected metal ions to have a longer mean free path than otherwise and ensure a large proportion of the ions will reach the substrate. The resulting films are polycrystalline in nature as they are grown at ambient temperature. A racetrack design is etched into the targets, where material is deposited from a circular region between the magnets; this is where the plasma is mostly confined and

hence is preferentially eroded.

The sputter system employed for the fabrication of these samples has independently rotating shutter and sample wheels with room for two magnetic and five non-magnetic targets to be used at any one time; one of the non-magnetic sources is a dedicated rf magnetron. This allows metallic multilayers to be deposited with ease. The metals used in this study are grown through a mask, for which there is a separate substrate wheel. The design of this mask is shown in fig. 3.2 and was designed by Dr. Mannan Ali specifically for this project. Only one mask is required to deposit a series of samples, as the mask can be moved between substrates due to a motor mechanism which separates the mask wheel from the sample wheel. Multiple masks can be used in this system for applications such as tunnel junctions or for multiple wire thicknesses on one substrate. The mask is pressed flush against the substrate, which is mounted on a stiff spring to ensure good contact, such that the edges of the film are as defined as possible. When using a shadow masking technique, the drawback can be ill-defined film edges if sample-mask contact is poor.

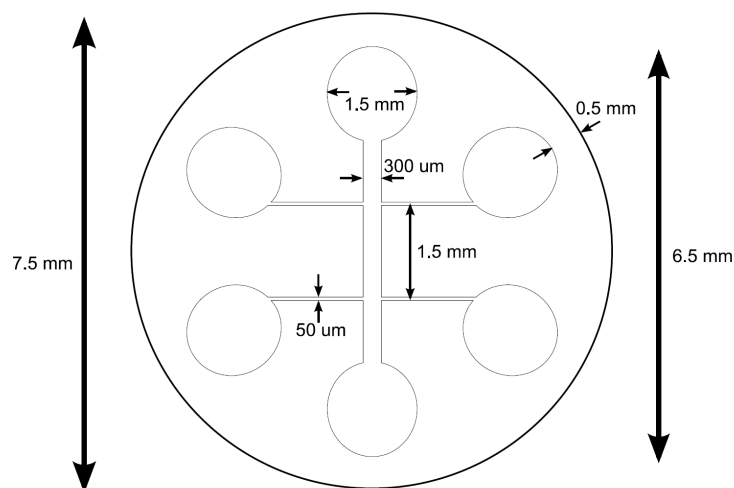


Figure 3.2: Schematic of the shadow mask used for sputter deposition of metals, designed by Dr. Mannan Ali. The design allows for four probe measurements of the longitudinal voltage, as well as transverse measurement of the Hall voltage. The manufacturing tolerance is  $\pm 5 \mu\text{m}$ .

Part of this project involved the investigation of dilute amounts of localised impu-

rities within a thin film. Discontinuous layers of metallic elements were deposited at various points during the growth of a host film, and these layers are referred to as  $\delta$ -layers. In order to ensure as minute an amount as possible was deposited, a technique was employed where the current applied to the magnetron gun, which sets the dc bias on the target, was reduced to a minimum value while the samples were in transit to the appropriate target. Once the sample is in position for the growth, the current is raised to standard growth level, then reduced once more when the required material has been deposited. This ensures that there is little extra deposition as the sample moves over the target, which takes around three seconds. The minimum possible current is determined by testing whether a sustainable plasma is possible at the current. Minimum current values were found to vary by target to be 2-5 mA. In contrast, the current applied during growth is 25-50 mA.

In order to ensure the cleanest and highest quality growth possible, substrates such as silicon, sapphire ( $\text{Al}_2\text{O}_3$ ), gadolinium gallium garnet ( $\text{Gd}_3\text{Ga}_5\text{O}_{12}$ , GGG) and yttrium aluminium garnet ( $\text{Y}_3\text{Al}_5\text{O}_{12}$ , YAG) are first cleaned in a beaker of acetone then isopropanol in an ultrasonic bath for five minutes each. Following this, they are dried with nitrogen or compressed air and then placed within the sample wheel for masked deposition, or taped with small amounts of Kapton tape to the sample wheel for sheet deposition. All sputter targets are first pre-sputtered for around three minutes to remove any oxide layer which may have formed on top when exposed to air.

### 3.2.2 $\text{Y}_3\text{Fe}_5\text{O}_{12}$ Preparation

$\text{Y}_3\text{Fe}_5\text{O}_{12}$  (YIG) is a complex material which can be prepared by, for example, pulsed laser deposition (PLD), liquid phase epitaxy (LPE) or radio frequency (rf) magnetron sputtering. In this project, we use rf magnetron sputtering as the chosen method, since this is by far the cheapest and quickest method of YIG preparation, and hence very desirable for industrial applications. After sputter deposition, additional processing is required in the form of annealing to produce an epitaxial film exhibiting ferrimagnetic ordering. A further step involves etching the top surface of the samples, which isn't

carried out in every case.

### 3.2.2.1 Radio frequency magnetron sputtering

Radio frequency (rf) magnetron sputtering works in a similar manner to dc magnetron sputtering, as described in section 3.2.1, but for insulating or dielectric materials. In these materials, if a dc method were used, a positive charge would build up on the surface of the target; this would inhibit the sputter rate and eventually stop sputtering from occurring altogether, as the argon ions would no longer be attracted to the target material. This can also cause arcing of the target, where large clusters of material are ejected from the target at once, leading to very poor films and potential damage to the sputter system. To prevent this from occurring, rf current is applied to the magnetron. This means the voltage of the cathode is switched at a frequency of 13.56 MHz, removing the positive charge build-up during the positive parts of the cycle, and sputtering material during the negative parts of the cycle. The target still has a negative bias during the positive section of the cycle, as positive ions are repelled from the surface while electrons are attracted to it. In the same way as with dc magnetron sputtering, a magnetic field is used to confine the plasma to the local area of the target, but this area is more widespread due to the nature of rf switching. The racetrack pattern eroded in the target is also wider and shallower, providing a more uniform deposition of materials from composite targets such as YIG. The growth rate of rf sputtering is often lower than that of dc magnetron sputtering since sputtering only occurs during the negative portions of the rf cycle.

To deposit YIG, a target composed of  $Y_3Fe_5O_{12}$  is used, but it has also been found that deposition must occur in an atmosphere of both argon and oxygen to provide optimum results. Much of the optimising work on this process was performed at the University of Leeds [110; 161; 165; 166]. The stoichiometry of YIG films was measured using scanning transmission electron microscopy (STEM) with very high resolution at the UK superSTEM facility [110; 161; 165; 166]. It was found that depositing with an argon flow rate of 22.8 SCCM and an oxygen flow rate of 1.2 SCCM, i.e. providing an atmosphere of 5 % oxygen to a total pressure of 2.4 mTorr, yields the most accurate

YIG stoichiometry.

The standard substrate used in many studies involving YIG is GGG, since it has very close lattice matching to YIG [58; 110; 161; 165; 167]. GGG is a strongly paramagnetic material, which exhibits a large signal in magnetometry measurements. A drawback of this substrate is that previous work by Dr. Arpita Mitra and Dr. Scott R. Marmion show the formation of a magnetically dead layer between the GGG substrate and the YIG when the samples undergo annealing [161; 165]. The annealing process is essential when employing sputtering at ambient temperature as a method to fabricate YIG. Without this step, the material is amorphous and exhibits no net ferrimagnetic behaviour. The formation of the dead layer is undesirable for applications in the propagation of magnons, and is believed to be due to gadolinium diffusing from the substrate into the film at high temperature [165]. An alternative choice of substrate has emerged with YAG, however a non-magnetic dead layer has recently been thought to form due to the diffusion of aluminium or yttrium when a YAG substrate is used, also [168]. YAG has a larger difference in the lattice constant from that of YIG, but has a benefit over GGG in that it has no strong paramagnetic signal. In this study, both substrates have been used, in the (111) orientation.

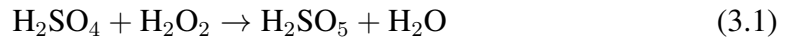
### 3.2.2.2 Annealing of YIG

After sputter deposition, the YIG films are annealed at 850 °C for two hours in air. This crystallises the YIG into an energetically favourable epitaxial state, where ferrimagnetism prevails. The target temperature is reached at a steady ramp rate of 5 K/min to avoid any unnecessary strain to the film and substrate. Once annealing is complete, the sample is cooled at the same rate. After this process, the material forms an ordered crystalline array and exhibits ferrimagnetism when probed by vibrating sample magnetometry.

### 3.2.2.3 Etching of YIG

Of paramount importance for the application of YIG is the quality of the interface between this material and any metal deposited on top; indeed, this is a driving influence in the direction of the research contained in this thesis. A measure of this quality for applications involving transfer of spin between the ferrimagnetic insulator and the normal metal is the spin mixing conductance,  $g_{\uparrow\downarrow}$ . This is, in effect, a measure of the number of spin transport channels per unit area between the two materials. It has been shown that etching the top YIG surface by bombarding it with argon ions yields a factor of five increase in  $g_{\uparrow\downarrow}$  for YIG/Au bilayers [19]. A recent study has shown that a wet etch treatment of the YIG top surface with piranha solution dramatically increases  $g_{\uparrow\downarrow}$ , also [18]. This process has been applied to YIG films grown in the group previously and has resulted in high quality YIG/Pt bilayers with desirable magnetotransport properties [110; 161]. This process has also been employed by other research groups in the preparation of YIG [21; 112].

Piranha etching involves the submersion of a YIG film in freshly prepared piranha solution. This solution is a mixture of seven parts sulphuric acid,  $\text{H}_2\text{SO}_4$ , to three parts hydrogen peroxide,  $\text{H}_2\text{O}_2$ . These reagents are combined in a glass beaker with the use of a magnetic stirrer, and undergo a vigorous exothermic reaction which is carefully monitored. Two reactions take place with different products. One of these is exothermic and produces water as follows



along with  $\text{H}_2\text{SO}_5$ . The other products produced include oxygen in atomic form; this is a volatile element which lends piranha solution its reputation for voracity in the destruction of both organic and metallic material. This is produced as follows



with two other, less volatile, products. When the temperature reaches 87 °C, this solution is poured into a glass beaker atop the YIG samples to be etched. The samples are left in the solution for three minutes before this is poured out. Purified water is poured into the beaker with the samples to dilute any remaining solution to safe levels, before

being dried with dry nitrogen and transported in isopropanol to the sputter deposition chamber.

## 3.3 Surface and structural characterisation

The sample structure and surface are characterised by using x-rays in reflectivity and diffraction experiments. These methods are outlined in this section.

### 3.3.1 X-ray reflectivity

The thickness of films grown by both dc and rf magnetron sputtering are determined via x-ray reflectivity scans. Data acquired using this technique also provide details of the electron density at the surface of the film, allowing for comparative surface characterisation between samples.

X-rays with a wavelength of 1.54 Å are produced via the acceleration of electrons within an x-ray tube assembly. These high energy electrons bombard a copper target and eject electrons from the copper. When an electron from the  $k$  shell is ejected, an electron from the  $l$  or  $m$  shell fills this vacancy, emitting radiation of a specific energy corresponding to the difference between the shells. This gives rise to the characteristic Cu  $K_{\alpha 1}$  and  $K_{\alpha 2}$  x-rays being emitted. Collimating slits are used to reduce the beam width to 100  $\mu\text{m}$ , while a monochromator eliminates Bremsstrahlung radiation which results from the 'braking' of accelerated electrons and other spectral lines including the Cu  $K_{\alpha 2}$  [169–171].

To perform an x-ray reflectivity measurement, the sample is positioned in such a way that the incident x-ray beam forms a low angle with the film surface, resulting in specular reflection. This typically occurs for an incident angle below 15 degrees. The experimental setup for x-ray reflectivity measurements is displayed in fig. 3.3. The various crystal planes provide many surfaces for the diffraction of the x-rays at higher angles, whilst the two film surfaces lead to two reflected waves from specular

### 3.3 Surface and structural characterisation

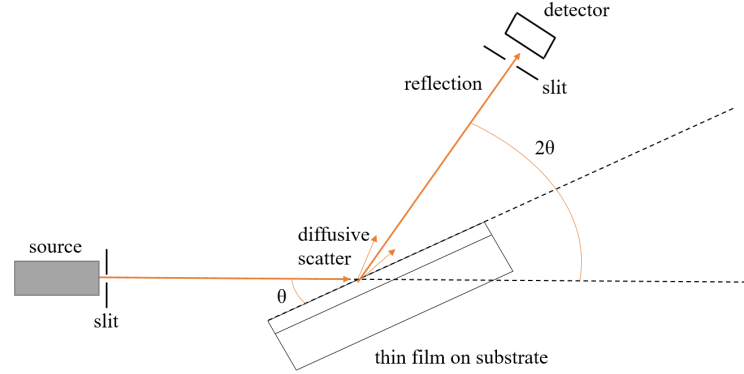


Figure 3.3: The experimental setup for x-ray reflectivity and diffraction measurements is illustrated. The Bragg angle,  $\theta$ , and detector angle,  $2\theta$  are also described. The substrate sits on a rotating stage to enable scanning of  $2\theta$ . Diffusive scatter is caused by surface roughness of the thin film.

reflection at lower angles. These waves interfere constructively as they are reflected specularly, in accordance with Bragg's law in eqn. 3.3. This law was reported in 1913 by William H. Bragg and his son William L. Bragg, following their pioneering work at the University of Leeds on the technique of x-ray reflection [172]. This law is given by

$$n\lambda = 2d \sin \theta \quad (3.3)$$

where  $n$  represents the order of reflection and is a positive integer,  $\lambda$  represents the wavelength of the incident x-rays,  $d$  is the spacing between the reflecting planes and  $\theta$  is the scattering angle, illustrated in fig. 3.3. When  $\theta$  is larger than the critical angle  $\theta_c$ , changes in the angle cause the intensity of the reflected beam to produce peaks known as Kiessig fringes. These are specific to thin films and are caused by interference of reflections from the top and bottom surfaces of the film. Using the small angle approximation, Bragg's law can be used to find the film thickness from the position of the Kiessig fringes in angle. This simple mathematical relation is

$$\frac{(2n + 1) \lambda^2}{4d^2} = \theta_{n+1}^2 - \theta_n^2 \quad (3.4)$$

where  $d$  represents the total film thickness and  $n$  is the index of the Kiessig fringe. A film thickness of 30-50 nm is optimum for producing sufficient Kiessig fringes to

### 3.3 Surface and structural characterisation

---

obtain a good estimate of the film thickness.

X-ray reflectivity measurements are a useful tool in obtaining data about the film surface, in addition to its thickness. The position of the critical edge, which appears below  $\theta_c$  and the manifestation of Kiessig fringes, contains information regarding the electron density at the surface of the film. The depth of Kiessig fringes is an indication of interface quality; a perfectly level film which has a sharp interface with the substrate leads to deep fringes, as the two reflected waves are in phase. If there is intermixing at the interface between the substrate and the film, as has been shown to be the case for YIG on GGG [110; 161; 165; 166], then the bottom interface is less well-defined and the electron density changes gradually in this region. This can result in diffusive scattering, which reduces the constructive interference and causes a reduction in the amplitude of the Kiessig fringes, but can also cause the period of the fringe pattern to be altered. Fringe depth can also be reduced for a thickness imbalance in a film; if the film grows in a wedge shape, the film interface is at a different angle to the top surface and as such constructive interference is reduced, causing a reduction in the observed fringe depth [169; 170]. Finally, the rate at which the intensity reduces as a function of angle can be used to extract data on the roughness of the film, with a rougher film leading to a sharper drop in intensity. A good knowledge of the film structure is required to fit these data and extract parameters [169–171].

#### 3.3.2 X-ray diffraction

Whilst x-ray reflectivity data reveal much about the surface properties of a thin film, x-ray diffraction is the preferred technique for examining the crystal structure of a film. At higher angles, the incident x-ray beam is diffracted through the sample and reflects at the atomic planes due to Rayleigh scattering from ionic sites in the crystal structure. Bragg's law, shown in eqn. 3.3, once again governs the constructive interference of the reflected waves [32; 173]. In this case,  $d$  refers to the separation between the crystal planes, and constructive interference between the diffracted waves only occurs at the angles predicted by Bragg's law. Thus, from analysis of high angle x-ray spectra, the interplanar spacing of a crystalline thin film can be determined, as first demonstrated

### 3.3 Surface and structural characterisation

---

by William L. Bragg in 1914 [173]. The incident angles scanned for high angle x-ray spectra vary depending upon the samples under study, but typically in the region 20-80 degrees. In order to determine the spacing between atomic planes in a cubic structure, the Miller indices are required; this is derived geometrically to give

$$d = \frac{a_0}{\sqrt{(nh)^2 + (nk)^2 + (nl)^2}} \quad (3.5)$$

where  $h$ ,  $k$  and  $l$  are the relevant Miller indices,  $n$  is the order of reflection,  $a_0$  is the lattice parameter and  $d$  is hence the planar spacing [32; 148]. A peak is hence found when scanning  $2\theta$  which corresponds to a particular lattice spacing. For a perfect crystal, this peak would be exceptionally sharp, but in reality a Gaussian peak is observed as the instrument function and imperfections in the crystal, such as defects and impurities, result in the broadening of this peak. The broadening can be used to determine the coherence length of x-rays through thin films; this corresponds to the size of crystallites and in an epitaxial film should correspond to the thickness of the film. The Scherrer equation is used to determine the size of the crystallites as follows

$$B = \frac{K\lambda}{L \cos \theta} \quad (3.6)$$

where  $B$  is a measure of the line broadening, often the full width at half maximum of the peak will suffice,  $K$  is a numerical constant relating to the crystallite shape which Scherrer found to be 0.93 for a cylinder,  $\lambda$  is the wavelength of the incident x-rays,  $L$  is the size of the crystallite and  $\theta$  is the Bragg angle [174; 175]. Thus the technique of x-ray diffraction is applicable to samples formed of many crystallites or particles, extending its reach to the study of powders and, more relevantly for this thesis, to be approximately true for polycrystalline metallic thin films, also [176]. Values of around 0.9 for  $K$  have been found to be applicable to thin films, although this formula provides only an approximate method of determining particular size for thin films [176]. The experimental setup is the same as illustrated in fig. 3.3 for x-ray reflectivity, but with a larger value of  $\theta$ .

### 3.4 Vibrating sample magnetometry

A vibrating sample magnetometer (VSM) is used to measure the net magnetic moment and coercivity of YIG samples prepared by rf magnetron sputtering. A schematic of a typical VSM system is shown in fig. 3.4. The VSM system in use during this project is housed within a gas flow cryostat, the principles of which are described in 3.5. The magnetometry principles alone are described within this section.

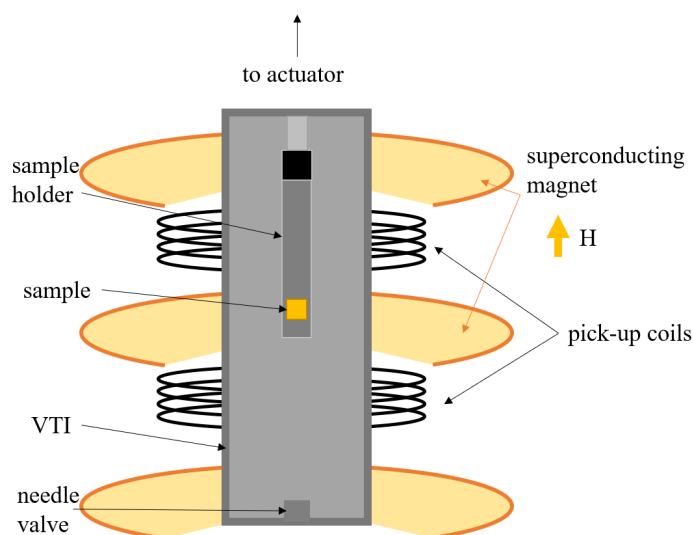


Figure 3.4: A schematic of a typical vibrating sample magnetometer (VSM) system. The large arrow labelled  $H$  indicates the direction of the applied magnetic field. The large coils marked ‘superconducting magnet’ represent a continuous coil of superconducting wire around the whole assembly. The variable temperature insert (VTI) and needle valve are concepts which will be explored in section 3.5.

A magnetic sample is placed upon a non-magnetic holder, composed of polyetheretherketone (PEEK), secured to and suspended from a platform. An actuator induces vertical motion of the sample assembly, causing it to vibrate at a frequency of 55 Hz between two pick-up coils, wound in opposite directions. The sample is aligned to be equidistant between the coils, which are spaced 7 mm apart, and the amplitude of the vibration is 15 mm. From Faraday’s law, the motion of a material possessing a net magnetic moment through the centre of a coil of wire will induce an electromo-

### 3.5 Low temperature electron transport

---

tive force (EMF) within the coil and subsequently a current. The oscillating nature of the sample's motion will hence produce an alternating current within the coils, which can be detected by using a lock-in amplifier. A reference signal is produced by the actuator for the lock-in amplifier to 'lock-in' to and eradicate noise from frequencies other than 55 Hz, and a time constant of 300 ms is chosen to facilitate this. A large superconducting coil is used to apply magnetic fields of up to 9 T from within a liquid He bath. This allows for the measurement of magnetic hysteresis loops which allow for determination of the sample magnetisation, with knowledge of its volume, and the coercive field where the net magnetic moment becomes saturated.

This technique is used to determine the saturation magnetisation,  $M_S$ , and coercivity,  $H_c$ , of YIG samples within this thesis. When a substrate of GGG is used, a strong paramagnetic background signal is observed which is removed in the data presented. This signal is linear and thus simple to remove with a linear fit to the high field data at room temperature. A YAG substrate provides only a very small diamagnetic signal and thus the raw data is displayed for these samples.

### 3.5 Low temperature electron transport

Magnetotransport measurements are taken at low temperatures in gas flow He cryostats. The exception to this is the data shown in chapter 4, where measurements are performed in a liquid helium bath. The principles of operation of the type of cryostat in use are here outlined, with a representative schematic shown in fig. 3.5.

In fig. 3.5, the sample sits within a specifically designed holder at the end of a sample stick. This is housed within a variable temperature insert (VTI) which allows the temperature of the sample to be altered by the flow of helium gas. At the bottom of the VTI, helium gas enters through the use of the needle valve and is heated by the heater located at this site. The needle valve itself is situated within the helium bath which surrounds the VTI, and is operated by a simple screw mechanism. The valve consists of a sharp needle-like point, constructed from steel, which sits within a brass housing which has a pipe leading to the VTI. As the needle tip is raised, helium can

### 3.5 Low temperature electron transport

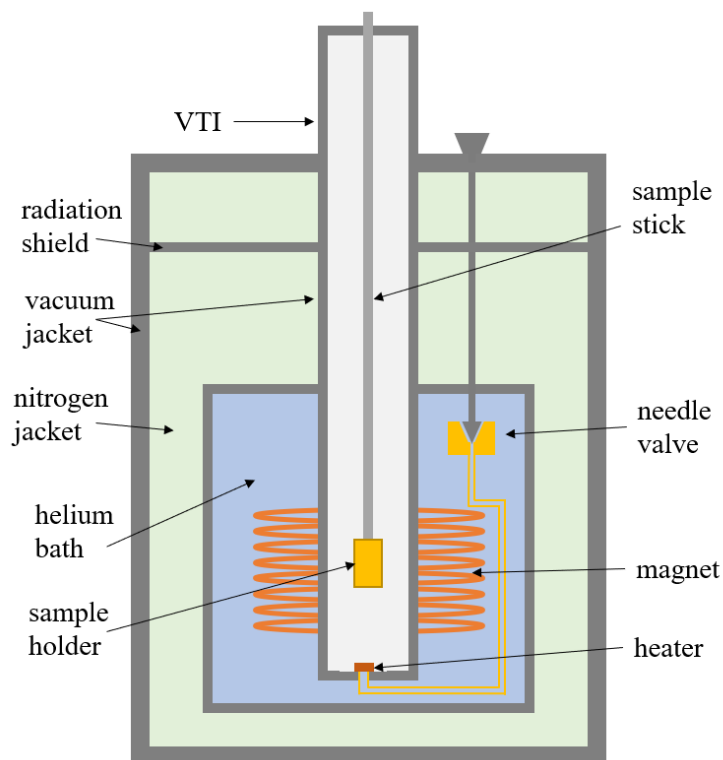


Figure 3.5: A schematic of a typical gas flow cryostat design. Here, VTI stands for variable temperature insert. The sample is ensconced within the sample head in this schematic, though its actual position varies.

flow into this pipe and into the VTI. The actual position for the entry of this gas into the VTI varies for different cryostat manufacturers, and can be placed much closer to the sample site. The heater response is tuned to ensure temperature stability under a variety of conditions. The helium enters the VTI space as this space is constantly being evacuated with the use of a roughing pump. Pumping of this space allows for better convection as the helium gas expands upon heating then is drawn toward the sample.

A magnet consisting of a coil of superconducting wire is used to apply magnetic fields to the sample, which is situated at the centre of this field to ensure uniformity. To prevent excessive waste of resources and insulate the sample, vacuum jackets are used. In particular, a vacuum jacket around the VTI promotes temperature stability and a vacuum jacket around the cryostat's exterior prevents excessive boil-off. A jacket of

## 3.5 Low temperature electron transport

---

liquid nitrogen around the liquid helium bath adds further insulation. Metal plates are placed toward the top of the cryostat to act as a shield from forms of electromagnetic radiation such as cosmic rays.

The magnetotransport data presented in this thesis were collected in two different styles of cryostat. In the first cryostat style, used for measurements of the Hall effect in chapters 4, 5 and 6, the design is much as illustrated in fig. 3.5. In this case, a superconducting solenoid allows for application of magnetic fields of up to 8 T, along the direction of the sample stick, and the VTI allows for measurements to be performed at a variety of temperatures.

The second design of cryostat is used for the collection of the majority of other magnetotransport data, including resistivity as a function of temperature and magnetoresistance measurements. The main feature which differs from the design shown in fig. 3.5 is the type of magnet employed. In this case, a split pair design is used to apply a field laterally, with a maximum magnitude of 3 T. A stepper motor is attached to the housing for the stick on top of the cryostat, which allows the sample to be rotated in the applied magnetic field. Another feature present on this design is the addition of a pressure gauge to allow for consistent conditions within the VTI. A pressure of 5 mbar is achieved at 290 K and the needle valve and pump are not adjusted from these parameters throughout the measurements.

### 3.5.1 Electrical measurements

Different methods are used to make electrical contact to the samples under study, and different pieces of apparatus are used to measure voltages. For measurements taken in chapter 4 and for Hall effect measurements, contact is made to the sample with gold-plated spring-loaded pins. For other measurements, pin contacts are used except in the case of rotations in the  $\beta$ -plane, which is defined in fig. 3.6. Here, the technique of wire bonding is used to make contact to the sample. This is due to the required orientation on the sample head being unavailable on a fixed mount with pin contacts. Aluminium wire, with a thickness of 30  $\mu\text{m}$ , is used to make contact with an ultrasonically formed

### 3.5 Low temperature electron transport

---

bond.

For magnetotransport measurements, a data acquisition (DAQ) card and Bayonet Neill-Concelman (BNC) connector is used to collect data. A 16-bit peripheral component interconnect (PCI) DAQ card is a good solution for measuring small voltages, as the maximum signal set by the user is split into 16 bits of data, providing high resolution measurements. For larger voltages, the resolution is significantly reduced, and the use of a highly sensitive voltmeter, such as a Keithley 2182 Nanovoltmeter, is preferred. Whilst this type of voltmeter has been used for some measurements, the majority utilise the DAQ card acquisition method. The main benefit of this method is the ability to measure multiple channels. Data are set to be acquired for each channel individually, preventing any interference between the channels. This method of data acquisition for sample holders which support the inclusion of multiple samples reduces the time taken to complete measurements dramatically. A noise level of 5 parts per million (ppm) in voltage signal or below is maintained throughout the measurement series, indicating the use of a more traditional voltmeter is not required. Up to three samples are connected in series for the application of 1 mA of direct current, and up to six channels are measured for the longitudinal and transverse voltages within each sample.

In measurements of the Hall effect, the voltage measured is rather small compared to the longitudinal voltage. In order to produce an optimal signal with maximal signal-to-noise ratio, a relatively high current should be applied; this allows for a Hall signal in the region of  $\mu\text{V}$  (for 1 mA) instead of nV (for a few  $\mu\text{A}$ ). A phenomenon to avoid in thin films is that of Joule heating, where the applied current generates heat within the conductor. To test for Joule heating, several measurements of voltage for varying applied currents were taken. If a linear relationship is found, the behaviour is Ohmic and hence Joule heating has not occurred. As a further test, a fixed current was applied for several minutes at liquid Helium temperature and voltage measurements were taken at regular intervals. For a current of 1 mA, no voltage changes were observed above the noise level, and thermometry local to the sample indicated no temperature fluctuations; as such, no Joule heating occurred. It was found that 1 mA was the optimal value

for producing a clean Hall signal whilst avoiding the negative impacts of Joule heating.

Lock-in amplifiers are an excellent method for measuring voltages with room temperature electronics, capable of giving a resolution of 2 nV consistently. Alternating current (ac) measurements were avoided in the preparation of this thesis, however. A DAQ card provided means to measure most efficiently due to the availability of six channels for voltage measurements and allowed for the collection of a complete dataset within the time-frame of a PhD project.

### 3.5.2 Magnetoresistance measurements

Various forms of magnetoresistance (MR) measurements are taken, and the orientations of the measurement planes are shown in fig. 3.6. Conventional MR measurements involve the sweeping of a magnetic field in one particular orientation, generally along the three axes depicted in fig. 3.6. In this figure, the charge current  $j_c$  is applied along the  $x$  axis. The longitudinal MR involves a field applied along the  $x$  axis, parallel to the current, whilst the transverse MR requires a field applied along the  $y$  axis, perpendicular to the current but situated in the plane of the film. The third orientation of conventional MR is the perpendicular MR, where the field is applied along the  $z$  axis, out of the plane of the sample.

Another form of MR measurement employed within this thesis is the angle-dependent MR, or ADMR. This involves a constant field being applied and the sample being rotated so that the field traverses a particular plane, illustrated in fig. 3.6. For a field which rotates in the plane of the  $x$  axis (longitudinal orientation) and  $y$  axis (transverse orientation), this is named the  $\alpha$ -plane magnetoresistance. The  $\beta$ -plane magnetoresistance involves a field being rotated in the plane of the  $y$  and  $z$  axes, i.e. between the transverse and perpendicular orientations. This orientation is used to measure the spin Hall MR (SHMR) as the current and field are always perpendicular, eliminating any anisotropic MR (AMR) from ferromagnetism. The  $\gamma$ -plane magnetoresistance is where solely AMR effects are measured, the the field rotates in the plane of the  $x$  and  $z$  axes, between the longitudinal and perpendicular orientations. In this case, the field

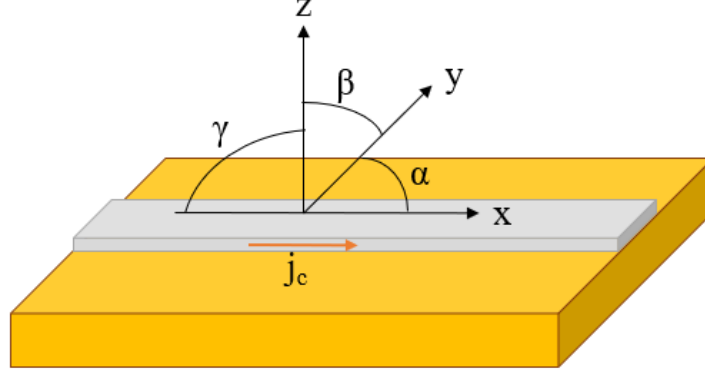


Figure 3.6: The nomenclature for the measurement planes and orientations for the magnetoresistance measurements within this thesis are displayed. The charge current,  $j_c$ , is oriented along the  $x$ -axis. The  $\alpha$ -plane is between the  $x$  and  $y$  axes, the  $\beta$ -plane between the  $y$  and  $z$  axes, and the  $\gamma$ -plane between the  $x$  and  $z$  axes.

is always perpendicular to the spin orientation which leads to the SHMR and as such no SHMR can be observed. The field does rotate with respect to the charge current, however, between parallel and perpendicular orientations, which causes the AMR to manifest if any is present. The  $\alpha$ -plane MR thus represents a sum of the  $\beta$ -plane and  $\gamma$ -plane MRs.

To characterise the MR, the relative change in resistivity is used. For the conventional MR, this is defined as follows

$$\frac{\Delta\rho}{\rho_0} = \frac{\rho(H) - \rho_0}{\rho_0} \quad (3.7)$$

where  $\rho(H)$  is the resistivity at the applied field  $H$ ,  $\rho_0$  is the resistivity at zero applied field and  $\Delta\rho/\rho_0$  is the quantity used to quantify the MR. For the ADMR, the definition depends upon the orientation, as the conventional definitions of the SHMR and AMR are used. For simplicity, the quantity which characterises the ADMR is still labelled  $\Delta\rho/\rho_0$ , but has the following value for the  $\alpha$ -plane MR

$$\frac{\Delta\rho_\alpha}{\rho_0} = \frac{\rho_x - \rho_y}{\rho_y} \quad (3.8)$$

where  $\rho_x$  is the resistivity at the applied field in the longitudinal orientation and  $\rho_y$  in

the transverse orientation. For the  $\beta$ -plane MR, the ADMR value is defined as

$$\frac{\Delta\rho_\beta}{\rho_0} = \frac{\rho_z - \rho_y}{\rho_y} \quad (3.9)$$

where  $\rho_z$  is the resistivity at the applied field in the perpendicular orientation. This definition is consistent with that for the SHMR. Finally, for the  $\gamma$ -plane MR, we define the ADMR as

$$\frac{\Delta\rho_\gamma}{\rho_0} = \frac{\rho_x - \rho_z}{\rho_z} \quad (3.10)$$

where the resistivities are as defined for the other orientations. This coincides with the relation that the AMR has  $\rho_x > \rho_y \approx \rho_z$  while the SHMR has  $\rho_z \approx \rho_x > \rho_y$  [17; 23; 113].

### 3.5.3 Hall effect measurements

The Hall effect has a particular measurement geometry which is adhered to at all times. In the ordinary Hall effect, a field is applied out of the plane of the sample and the Lorentz force causes electrons to deflect their path to one side of the conductor, resulting in a transverse voltage known as the Hall voltage [55]. The sign of the Hall coefficient is determined by understanding the relative orientations of the current and the field, as the Lorentz force is governed by the right-hand rule. In the Hall measurements performed in this thesis, the current is applied in the positive  $x$  direction and the field in the positive  $z$  direction. The electrons are hence deflected in the positive  $y$  direction, causing a voltage in the negative  $y$  direction. The contacts are hence made to satisfy this geometry and result in the correct sign of the Hall coefficient.

The shadow mask illustrated in fig. 3.2 is designed as a Hall bar which means the transverse voltage measured is designed to have no component of the longitudinal voltage within it. To ensure this, the Hall bars across the central electrode are six times thinner than the central electrode and are designed to be exactly opposite one another. In reality, manufacturing tolerances of  $5 \mu\text{m}$  mean that a component of the longitudinal voltage is measured, resulting in a zero field voltage and a component to the signal which is symmetric with respect to the applied field. The data is hence

### 3.5 Low temperature electron transport

processed to remove this component, with the symmetric component corresponding to the perpendicular MR and the antisymmetric component to the Hall effect. The symmetric component is found from

$$V_{\text{sym}} = \frac{V(+\mu_0 H) + V(-\mu_0 H)}{2} \quad (3.11)$$

with the asymmetric component given by

$$V_{\text{asym}} = \frac{V(+\mu_0 H) - V(-\mu_0 H)}{2} \quad (3.12)$$

where  $V_{\text{sym}}$  and  $V_{\text{asym}}$  are the symmetric and antisymmetric voltage components, respectively, and  $V(\pm\mu_0 H)$  represents the voltage at a particular applied field, applied either in the positive or negative  $z$  orientation.

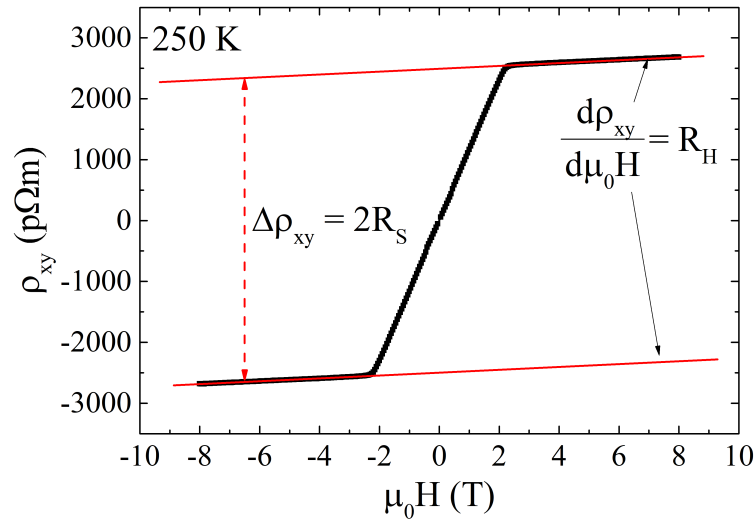


Figure 3.7: The Hall effect observed for 35 nm Fe with a 2 nm Pt cap on an  $Al_2O_3$  substrate is used as an illustrative example for the determination of the ordinary and anomalous Hall coefficients,  $R_H$  and  $R_S$ , respectively.

Once the asymmetric component of the measured voltage has been extracted, this is divided by the applied current and multiplied by the film thickness to provide the Hall resistivity,  $\rho_{xy}$ . For the ordinary Hall effect, this forms a linear relationship with the applied field, of which the gradient is the ordinary Hall coefficient,  $R_H$ . For the anomalous Hall effect, however, the field dependence is less trivial. At low field, there exists

### 3.5 Low temperature electron transport

---

a field-dependent contribution to the Hall resistivity from the anomalous Hall effect, which saturates at the saturation field of the magnet. Beyond this field, the contribution is constant and thus the gradient at high field is equal to  $R_H$  once more [70]. In order to find the anomalous Hall coefficient,  $R_S$ , the difference between the two intercepts of linear fits at large positive and negative fields is halved. This is illustrated in fig. 3.7. This method is appropriate only for samples lacking a magnetisation; the illustrated sample does contain a magnetisation, and as such the conventional scaling proposed in section 2.4.2 is the appropriate one to use in this case. This example is shown for ease of illustration; another example of this is shown in fig. 2.2b) for a sample without a net magnetisation. In the case where the field at which the anomalous Hall component  $R_S$  ceases to change with increasing field is unclear, data at sufficiently high fields must be used to fit the linear relationship and determine both  $R_H$  and  $R_S$  with any accuracy. Throughout this thesis, data are fitted between applied field values of 7-8 T in order to determine the values of the coefficients.

---

# CHAPTER 4

---

Non-magnetic impurity delta layers in  
the Hall effect

## 4.1 Introduction

Impurities have a long history of being used within metals in order to study scattering. In the search for higher yield spin Hall effect devices, dilute alloy systems of a host with low spin-orbit coupling and an impurity with high spin-orbit coupling have proven promising candidates for a large extrinsic spin Hall effect [10–14]. Since these effects are dependent upon extrinsic scattering from impurities, and this scattering is the same for electrons in both charge currents and spin currents, it was decided to study the effects predicted for spin currents within a charge current system. This is a much simpler experiment to perform with a much lower cost than the fabrication of multiple spin Hall devices to probe the position dependent physics. As such, in this chapter the effect on the ordinary Hall effect of a discontinuous delta layer of a metal with high spin-orbit coupling in a non-magnetic system is investigated.

## 4.2 Transport properties of Cu thin films

Copper, although itself possessing low spin-orbit coupling and a negligible intrinsic SHE, has been shown to produce large extrinsic effects when doped with Ir and Bi impurities [10–12]. For this reason, Cu was chosen as the host metal for a study of 5*d* impurity delta layers. It is hence of great importance to first characterise the resistivity and Hall effect of the host metal. This is facilitated through a thickness dependence study. A series of thin films of Cu are grown, shaped as a Hall bar through shadow masked sputter deposition, to various thicknesses. The substrate chosen for this study is polished n-type silicon coated with 100 nm of dry thermal oxide to give a resistivity in the range 5-10 M $\Omega$  cm. The resistivity and ordinary Hall coefficient at 4.2 K of the Cu samples deposited on this substrate are plotted as a function of film thickness in fig. 4.1. Uncertainties are plotted as error bars in this figure, but are smaller than the point size in most cases.

The values of the resistivity are in line with those reported in the literature for thin films of copper, at higher thicknesses approximating to the bulk value [57; 64]. The

## 4.2 Transport properties of Cu thin films

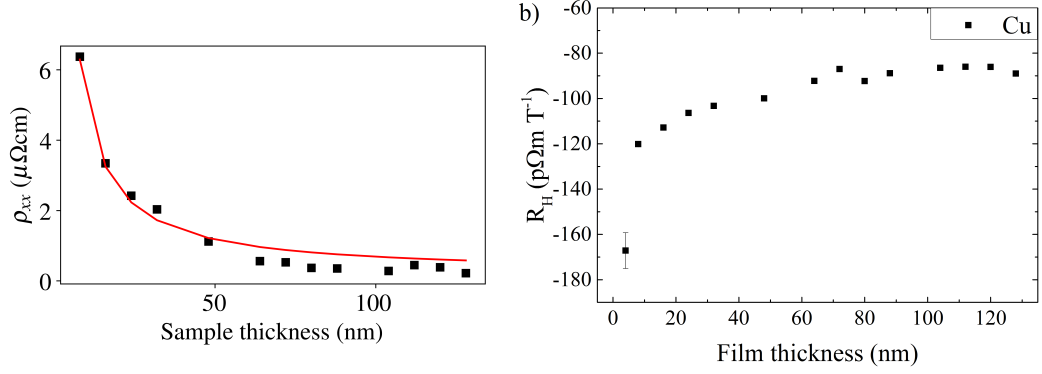


Figure 4.1: The a) resistivity and b) ordinary Hall coefficient for thin films of Cu at a temperature of 4.2 K are displayed as a function of film thickness. Panel a) shows a fit of the Fuchs-Sondheimer relation to the data.

bulk value of the mean free path is found to be  $(0.7 \pm 0.2) \mu\text{m}$  via a fit of the theory of Fuchs and Sondheimer, i.e.

$$\rho(t) \approx \rho_0 + \frac{3}{8} \rho_0 \lambda_0 \frac{1}{t} (1 - p) \quad (4.1)$$

where  $\rho(t)$  is the resistivity of a thin metal film of thickness  $t$ ,  $\rho_0$  is the resistivity of a bulk sample of the same composition,  $\lambda_0$  is the mean free path of the conduction electrons in the bulk and  $p$  is the parameter governing surface scattering, as in equation 2.6. This value of the bulk mean free path is consistent with literature [64]. It is found that  $\sigma_0 = (5 \pm 3) \mu\Omega\text{cm}$  and  $p = (0.003 \pm 0.003)$ . A note on the units of the Hall coefficient is warranted here. Throughout this thesis, units of  $\Omega\text{m T}^{-1}$  are used, which are equivalent to  $\text{m}^3\text{C}^{-1}$ . The other units often employed in the literature are  $\Omega\text{cm G}^{-1}$  which is equivalent to  $10^{-2} \Omega\text{m T}^{-1}$ . The Hall coefficient is varying in the range  $\text{p}\Omega\text{m T}^{-1}$ , having a larger value than previously demonstrated for polycrystalline Cu at this temperature at lower thicknesses, but at higher thicknesses is in line with literature value [57; 64]. Hence the polycrystalline copper films grown by dc magnetron sputtering are of high purity and well-suited to the task of hosting impurity  $\delta$ -layers.

During the growth of samples with discontinuous  $\delta$ -layers, the film is rotated within the growth chamber to another target and then rotated back to the copper target. In order to determine whether this movement and break in growth causes any transport effects, a control experiment was performed. Here, the sample growth was interrupted at

points where a  $\delta$ -layer may be inserted to determine if any dependence on the position of this interruption arises. This acts as a check of whether impurities in the vacuum are significant enough to alter transport properties, and also whether any induced defects are capable of causing some extrinsic scattering phenomena. No trend was observable with position and 71 % of results were within one standard deviation of the average. This data was combined with control samples in each growth cycle to find the Hall coefficient of undoped Cu with a thickness of 40 ML at a temperature of 2 K.

Throughout this chapter, multiple growth runs are employed to study the position dependent effects for various impurities within a Cu host of around 16 nm thickness; the actual thickness varies slightly between datasets, with a standard deviation of 1 nm. Twenty control samples in all were created during this process, with one for each growth run involving impurities, to give seven such samples, along with thirteen in the control experiment with a pause. The solid lines in fig. 4.7 represent the control value for each dataset of the absolute value of the ordinary Hall coefficient,  $|R_H|$ , with the dashed lines representing the standard deviation in this value. The ordinary Hall coefficient for  $(16.67 \pm 0.06)$  nm of copper was found to be  $-(96.2 \pm 0.7) \text{ p}\Omega\text{m T}^{-1}$  with a standard deviation of  $2 \text{ p}\Omega\text{m T}^{-1}$ . These results serve as a basis to determine whether subsequent results for doped samples are statistically significant.

### 4.3 Resistivity of thin films with $\delta$ -layers

In order to investigate the ordinary Hall effect for samples with a discontinuous  $\delta$ -layer of non-magnetic impurities, several films are produced for each dataset with the position of the  $\delta$ -layer changing in each. In order to model the behaviour of the resistivity  $\rho_{xx}$  as a function of this position, a model of parallel conductors is employed.

Considering the theory of Fuchs regarding the effects of film thickness and mean free path upon the resistivity of a thin film, the conductivity of one layer can be expressed as found in equation 2.2 with  $\Phi(k)$  as defined in equation 2.3 with the integral  $Ei(-k)$  shown in equation 2.4 and the Drude conductivity in equation 2.5. In order to apply a parallel conductor model, the films can be considered a tri-layer system;

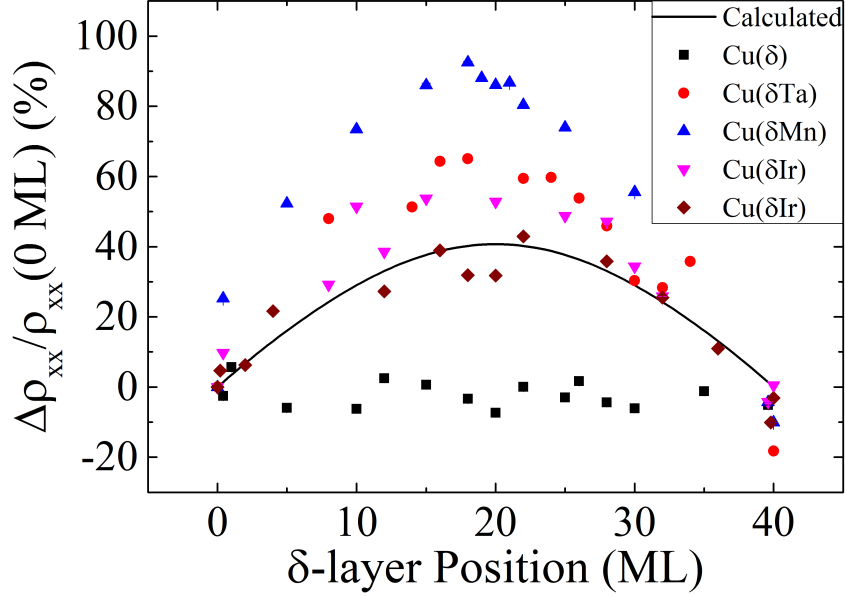


Figure 4.2: The longitudinal resistivity  $\rho_{xx}$  as a function of impurity position in monolayers (ML) of the host metal Cu for Ta, Mn and Ir. The black squares show the results for Cu with an interruption in growth while the black line shows the results of the general parallel conductors model for resistivity. All measurements were taken at a temperature of 2 K.

there are two layers of the host metal, of thickness  $z$  and  $(T - z)$  with an alloyed delta layer between the discontinuous layer of impurities and the host metal, of thickness  $d$ . For impurities at the film surface, this becomes a bilayer system. The theory of Fuchs can hence be employed to find the conductivity of each of these layers. In considering the integral of equation 2.4, there exists no analytical solution and as such numerical methods must be used. Using the substitution  $y = 1/t$ , the integral of equation 2.4 becomes

$$-Ei(-\kappa) = \int_0^{1/\kappa} \frac{1}{y} e^{-1/y} dy \quad (4.2)$$

using the relation  $dt = -y^{-2}dy$  to complete the variable replacement. The integral now has finite limits, allowing the use of Simpson's rule with the form

$$E = \frac{1}{3}h \left( f_0 + f_N + 4 \sum_{\text{odd, m}} f_m + 2 \sum_{\text{even, m}} f_m \right) \quad (4.3)$$

where  $N$  represents the total number of steps which are employed between the limits; this must be an even number. The interval between these steps is  $h$  while  $f_i$  represents

### 4.3 Resistivity of thin films with $\delta$ -layers

---

the value of the function in the integrand when evaluated at  $i$ . In finding the conductivity of each layer, a value of  $N = 10^5$  is used, since values larger than this were still consistent to four significant figures.

In order to combine the conductivities of the layers in a model of parallel conductors, these must be scaled by the relative thicknesses of the layers. To facilitate this, the conductance of the entire sample is found from

$$g = \frac{W}{l}(\sigma_z z + \sigma_{(T-z)}(T - z) + \sigma' d) \quad (4.4)$$

where  $W$  is the width of the sample,  $T$  is the total sample thickness,  $l$  the distance between the voltage probes,  $\sigma_z$  and  $\sigma_{(T-z)}$  are the conductivities of the host metal of thickness  $z$  and  $(T - z)$ , respectively, while  $\sigma'$  is the conductivity of the alloyed  $\delta$ -layer and  $d$  is its thickness. The only adjustable parameter is the fraction of the total conductivity that  $\sigma'$  represents. It is assumed that  $\sigma' \approx \sigma_0/3$  to give the result shown in fig. 4.2. This value for the  $\delta$ -layer conductivity is chosen as it represents well the relative conductivity of Cu alloys with similar metals in the literature [10–13]. The bulk mean free path found from the Fuchs-Sondheimer fit in fig. 4.1a) is used along with  $\sigma_0$  chosen from this fit. The samples have dimensions shown in fig. 3.2.

The general shape observed in the data is recreated by the calculation, affording insight into the origins of the trend. The form of the resistivity as a function of delta layer position is a further manifestation of this phenomenon; additional scattering occurs at the interface between the host and the impurity  $\delta$ -layer. For  $\delta$ -layers in the centre of the film, the resistivity is hence increased the most as both of the host metal layers contribute equally to the resistivity.

Scattering events within the alloyed  $\delta$ -layer are ignored in this model; the coverage of the delta later is around 60 % and hence gives a discontinuous layer of impurities. By neglecting scattering within this discontinuous layer, scattering at impurity sites is modelled more clearly. Assuming a small  $d$  of the  $\delta$ -layer and neglecting finite size effects within this alloyed layer hence better represents the physical picture. The parameters used give good quantitative agreement for a  $\delta$ -layer of iridium with copper. A small change in thickness between the two iridium-doped datasets leads to a change in

#### 4.4 The Hall effect in thin films with impurity $\delta$ -layers

---

the relative resistivity. Tantalum impurities lead to a greater increase in the resistivity while manganese leads to the highest, with a doubling of the resistivity for an impurity  $\delta$ -layer at the interface with the substrate when it is moved to the centre of the film. This dependence upon impurity character cannot be modelled within the theory of Fuchs for scattering at film boundaries. The scattering type involved is more likely to be the cause of this change in magnitude. Mn impurities have been shown to produce the spin effect, as outlined in section 2.4.1.1, in the ordinary Hall effect when doped in a Cu host at higher concentrations [49; 68]. Iridium is known to produce strong skew scattering when used a dopant in spin Hall effect devices [10] but its effect on the resistivity is less well known. Tantalum is also known to produce skew scattering, and has been postulated as a candidate for resonant scattering with side-jump in spin Hall effect devices [14; 177]. These scattering types may be the cause of the dependence on impurity character, but the cause currently remains unknown. Work is ongoing with calculations being performed by Dr. Martin Gradhand at the University of Bristol in order to determine the cause of the relative changes.

#### 4.4 The Hall effect in thin films with impurity $\delta$ -layers

Impurities of Mn, Ta, Fe, W, Ir and Bi are considered as delta layers within a Cu host. A temperature of 2 K is used to measure the Hall coefficient(s) in order to determine the changes in the absence of strong electron-phonon scattering, allowing other forms of scattering to be observed to modify the Hall effect; this could include scattering with side-jump [69] or the spin effect [49; 68], as outlined in section 2.4.1.1. Fields of up to 8 T are applied in the perpendicular orientation for a Hall bar of Cu with an impurity  $\delta$ -layer at a fixed position in the  $z$  axis of the film. The Cu thickness used is in the range  $(16 \pm 1)$  nm over eight datasets with 136 samples analysed for transport, in all. The film thickness is converted into monolayers for the analysis, with each film assumed to contain 40 monolayers (ML) of Cu as the average interplanar spacing of Cu is around 2-4 Å [178; 179] for polycrystalline samples such as these.

#### 4.4.1 The anomalous Hall effect in Cu( $\delta$ Fe)

There is one system considered in this chapter, that of Fe  $\delta$ -layers in a Cu host, which deviates from the linear relationship between  $\rho_{xy}$  and applied field. In this case, an anomalous Hall effect is produced and the case for a  $\delta$ -layer in the centre of the film is shown in fig. 4.3. For this film, it is found that  $R_H = -(84.10 \pm 0.07) \text{ p}\Omega\text{m T}^{-1}$  and  $R_S = (36.9 \pm 0.4) \text{ p}\Omega\text{m}$  at a temperature of 2 K as per the definition in equation 2.28. The anomalous Hall component can be clearly seen to saturate at relatively low field, compared to the measurement range, and as the field is increased beyond this, there exists a linear response in the Hall resistivity due to the OHE. This image is quite different than those first discovered for the AHE, where  $R_S$  was found to be much greater than  $R_H$  [70]. Given the nature of the impurities, it is prudent to check whether the low-high field transition discussed by Hurd [57] can be observed.

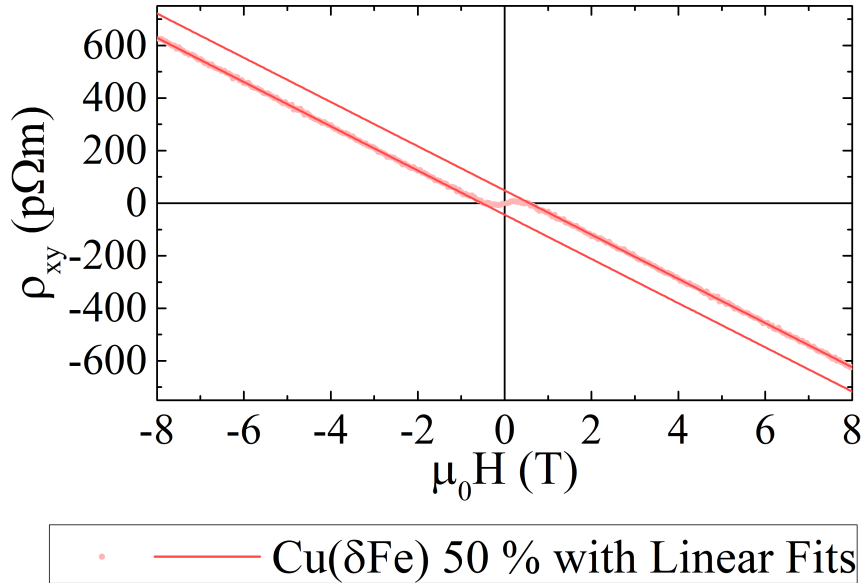


Figure 4.3: The Hall resistivity  $\rho_{xy}$  is shown as a function of applied field for 40 ML Cu with a  $\delta$ -layer of Fe at 20 ML. The data were taken at 2 K. Linear fits are shown to the ordinary Hall component.

An anomalous Hall effect produced by such a dilute amount of Fe in a non-magnetic host which is far from satisfying the Stoner criterion, and hence unable to experience

#### 4.4 The Hall effect in thin films with impurity $\delta$ -layers

---

a magnetic proximity effect, is surprising. Previous studies involving Fe as a dilute impurity with a non-magnetic host have largely involved much greater concentrations; 60 % coverage of one monolayer in a 40 ML sample equates to a concentration of 1.5 %, in comparison to those in excess of 30 % in, for example, ZrFe [69]. Whilst a planar array of Fe atoms in Pt has previously been studied [79], this was for a much thinner film and hence a much higher concentration. The films discussed in fig. 2.6 are 0.9 mm thick with lateral dimensions 1 cm x 5.7 cm [64], making them bulk-like in comparison to the thin films investigated in this study.

The change in Hall resistivity from the linear ordinary Hall resistivity is plotted in fig. 4.4 for Fe  $\delta$ -layers at various positions within 40 ML of Cu. This allows for comparison to fig. 2.4b) from section 2.4.1. For impurities at 40 ML, i.e. the exposed surface of the film, no discernible AHE is observed and as such  $|\Delta\rho_{xy}| \approx 0$  for all fields. For the impurity  $\delta$ -layer placed at the other surface, that between the substrate and the film, however, an AHE is observed. The largest  $R_S$  observed occurs for a  $\delta$ -layer at the centre of the film, i.e. at 20 ML, and it can be seen from fig. 4.4 that this consequently produces the largest  $|\Delta\rho_{xy}|$  as a function of field. For impurities on the top surface of the film, the exposure to air causes oxidation. The Fe in this position, therefore, and when placed a few ML into this top surface, is oxidised and produces no AHE.

The form of the curves in fig. 4.4 is classified as type C when compared to fig. 2.4. This signifies that there is a sizeable spin component, due to the spin effect, to the Hall resistivity which does not saturate at the fields applied [57]. This is a surprising result, as it has previously been found that for dilute magnetic impurities, in systems such as AuFe, a spin component has been absent from the observed Hall resistivity; only when the concentration is increased can a component be observed, with the response becoming type B and then type C with increasing concentration [57; 63]. Some results for comparison are shown in fig. 2.6. It can be observed that the data in fig. 2.6b) show a non-saturating spin component at the highest concentrations of Fe within a Cu host; for the very highest concentration, of 325 ppm or 0.03 %, the response with field is linear. The physics which lead to the enhancement of the spin component of

#### 4.4 The Hall effect in thin films with impurity $\delta$ -layers

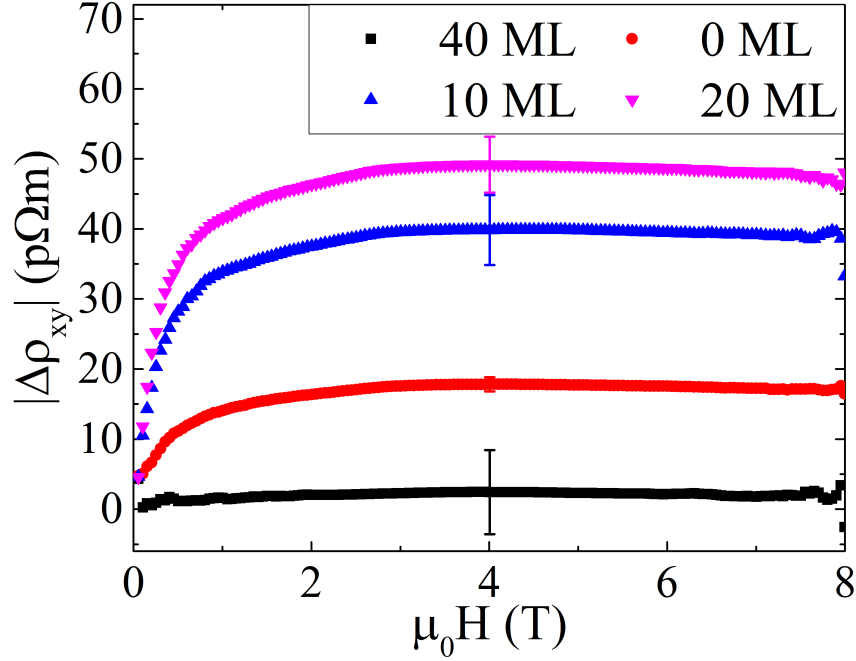


Figure 4.4: The absolute change in the Hall resistivity after subtraction of the ordinary Hall resistivity is shown for 40 ML Cu with a  $\delta$ -layer of Fe placed at the positions indicated in the legend. The data have been averaged and an indication of the scatter is shown at  $\mu_0 H = 4$  T with a single error bar for each curve. The data were collected at a temperature of 2 K.

the AHE in Cu( $\delta$ Fe) compared to a more traditional dilute CuFe alloy is currently unknown. Calculations are underway by a collaborator which hope to shed some light on the phenomenon, investigating skew scattering and scattering with side-jump in these samples. The effect of impurity  $\delta$ -layer position on the anomalous Hall coefficient  $R_S$  is shown in fig. 4.5.

The anomalous Hall component vanishes for  $\delta$ -layers at the top surface of the film. Being exposed to air, it is likely the Fe impurities are oxidised hence diminishing the anomalous Hall effect. The maximum magnitude of  $R_S$  occurs not at 20 ML but 16 ML. Enhanced scattering may be expected to be observed in the centre of the film for much the same reason as the increase in longitudinal resistivity; the largest contribution from scattering at the  $\delta$ -layer interface occurs for a  $\delta$ -layer in the centre of the film, according to the expansion of Fuchs-Sondheimer theory. The contribution of scattering

#### 4.4 The Hall effect in thin films with impurity $\delta$ -layers

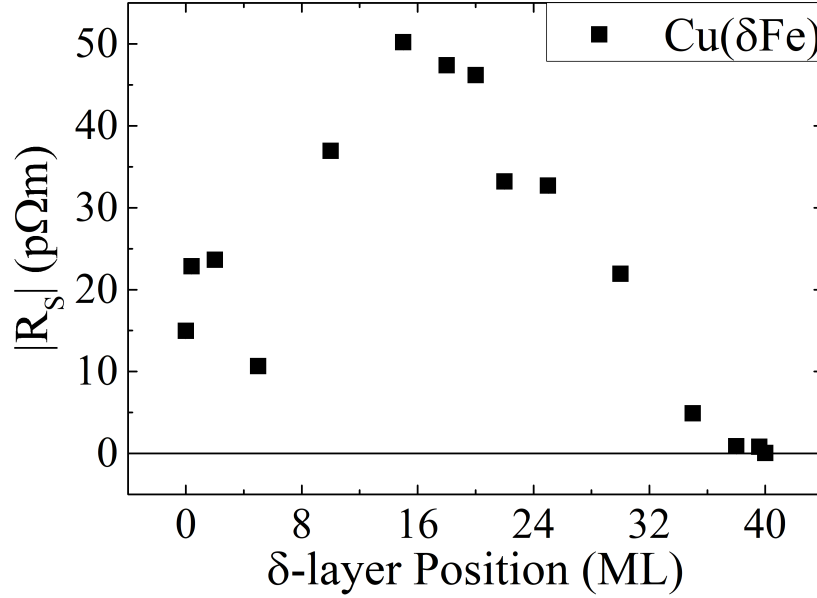


Figure 4.5: The anomalous Hall coefficient  $R_S$  as a function of  $\delta$ -layer position for a  $\delta$ -layer of Fe within 40 ML of Cu. All measurements were taken at 2 K. A solid line is provided at  $R_S = 0$  for comparison to clean Cu.

with side-jump to the anomalous Hall effect is expected to be proportional to  $\rho_{xx}^2$ , as in equation 2.27, and this could be the reason for the qualitative similarity; scattering with side-jump is known to be a prevalent cause of the anomalous Hall effect for Fe impurities [47; 48; 56; 69; 80]. This analysis is left to further work as longitudinal resistivity data could not be collected for these samples.

#### 4.4.2 The ordinary Hall effect in Cu with impurity $\delta$ -layers

It has been shown that a  $\delta$ -layer of Fe impurities within a 16 nm film of Cu produces an anomalous Hall effect which can be observed in the Hall resistivity as a function of field. Dopants of Ta, W, Ir and Bi were also employed in this study within a Cu host of the same thickness. An example of the observed Hall resistivity for a sample without dopants and with a  $\delta$ -layer of Iridium midway through the film is shown in fig. 4.6. Linear fits indicate that no deviation is observed from the ordinary Hall effect and no anomalous behaviour is observed as a function of field for any of the samples

#### 4.4 The Hall effect in thin films with impurity $\delta$ -layers

doped with non-magnetic impurities under study. The inclusion of an impurity  $\delta$ -layer changes the value of the Hall coefficient and this effect is discussed further in the remainder of this section.

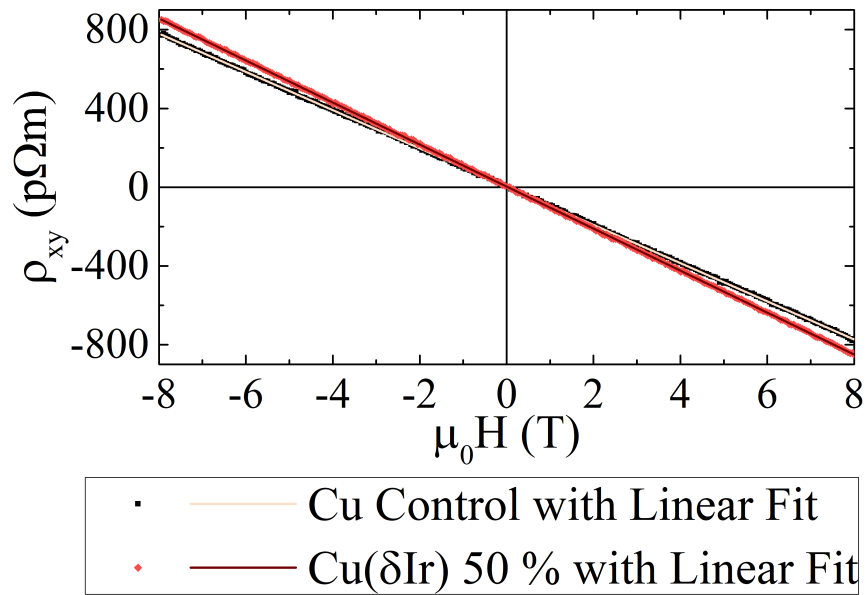


Figure 4.6: The Hall resistivity  $\rho_{xy}$  is shown as a function of applied field for pure Cu (black squares) and Cu with a  $\delta$ -layer of Ir impurities in the centre of the film (red diamonds). Both measurements are displayed with linear fits and were taken at a temperature of 2 K.

The change in the ordinary Hall coefficient  $R_H$  is shown as a function of impurity  $\delta$ -layer position in fig. 4.7 for all impurity  $\delta$ -layer systems under study. The standard deviation of  $2 \text{ p}\Omega\text{m T}^{-1}$  is indicated by the dashed lines in fig. 4.7 as a percentage change from the control value for each dataset. It can hence be seen that the trends which emerge are statistically significant and not a result of random fluctuations in the measurement. All data are collected at a temperature of 2 K with an applied field of up to 8 T. The data in fig. 4.7a) for Cu with a  $\delta$ -layer of Ir is displayed as both red circles and blue triangles; these are two separate sets of samples which were repeated as a further indicator of the statistical significance of the result. Some scatter, of the same order as the standard deviation found for Cu with an interruption in growth, is observed but its magnitude indicates an excellent agreement between datasets and hence

#### 4.4 The Hall effect in thin films with impurity $\delta$ -layers

a significant result.

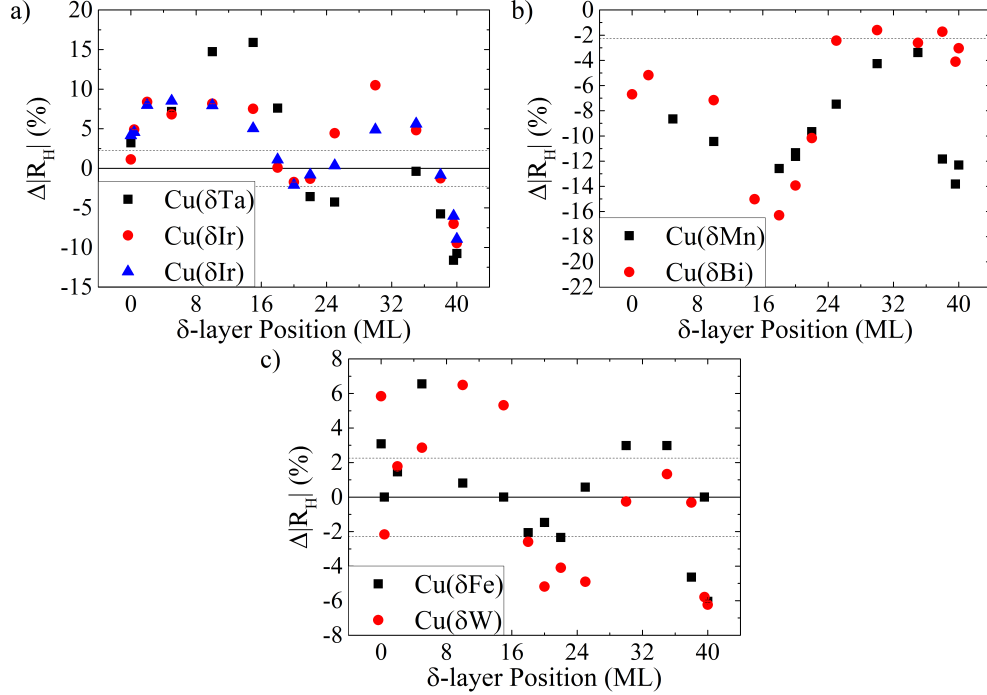


Figure 4.7: Relative changes in the ordinary Hall coefficient  $R_H$  as a function of impurity  $\delta$ -layer position for impurities of a) Ta and Ir, b) Mn and Bi, and c) Fe and W within a 40 ML Cu host from the value without impurities. All measurements were taken at 2 K and the dashed black lines represent the standard deviation in the value of  $R_H$  found from the pure 40 ML Cu control samples.

It is worth noting the electron configurations of the various impurities at this point; the impurity sites are assumed to be well-separated and non-interacting and hence their electronic configurations are of interest. The data have been grouped according to the spin state of the impurity ion as a result of the valence shell filled using Hund's rule. It can be observed that impurities within each grouping possess a similar trend with impurity position, both qualitatively and quantitatively. The electron configuration in the valence shell for Ta is  $5d^3$  and for Ir  $5d^7$ . This means that both these shells contain three unpaired electrons. For Mn and Bi, their valence electron configurations are  $3d^5$  and  $6p^3$ , respectively; these shells are half-filled and hence their orbital angular momentum is zero. The valence configurations for the final grouping, Fe and W, are  $3d^6$  and  $5d^4$ ,

respectively, meaning both have four unpaired electrons in their valence shells. This correlation is of note when considering the ordinary Hall coefficient for samples with dilute impurities [49; 68; 84]. Though traditionally this was thought to be observed as a deviation from linear behaviour for the Hall resistivity as a function of field, if the samples remain in the low-field condition, as illustrated in fig. 2.4a), a linear trend with field will be observed. This has not been experimentally confirmed, however, and as such there is currently no accompanying theory which allows for extraction of parameters. It is hoped that the calculations underway will allow for a better understanding of the spin effects in this system and lead to a method for extracting more meaningful data about the spin effect from the Hall resistivity data in the absence of non-linear effects.

It is clear from fig. 4.7 that the ordinary Hall coefficient of Cu is modified by the inclusion of the  $\delta$ -layer of both magnetic and non-magnetic impurities as a function of position. This change is asymmetric about the centre of the film; in the calculations currently being performed, an attempt is being made to simulate the effects of polycrystalline Cu in a real-world system.

## 4.5 Summary

It has been shown that discontinuous impurity  $\delta$ -layers of both magnetic (Fe) and non-magnetic impurities (Ta, Ir, W and Bi) alter the value of the ordinary Hall coefficient in a manner dependent upon the impurity character at a temperature of 2 K. This change as a function of position has never before been observed. The form of the Hall effect remains linear for non-magnetic impurity  $\delta$ -layers in a Cu host up to a field of 8 T. A correlation is apparent between the spin state of the impurity ions and the form and magnitude of the position dependence. In the case of magnetic impurities, a single  $\delta$ -layer of Fe within 20 ML of Cu has been shown to produce an anomalous Hall effect which depends upon the position of the impurity  $\delta$ -layer in a manner separate from the associated ordinary Hall coefficient of the films. The fundamental physics at work here is interesting and novel; theoretical work is underway to provide an explanation of all the effects discussed in this chapter and the contents of this chapter will lead to a

high impact journal publication in the near future.

---

# CHAPTER 5

---

The effect of localised Fe impurities on  
the magnetotransport of thin Pt films

## 5.1 Introduction

Pt doped with magnetic impurities has long been a system of interest in solid state physics, with the discovery of the magnetic proximity effect (MPE) leading to the potential for designing materials with desirable properties for applications [68; 79; 85; 86; 143; 159; 180]. More recently, great interest has been placed on the effect of the MPE on spin transport phenomena such as the spin Hall effect (SHE) and spin Hall magnetoresistance (SHMR) [17; 20–23; 109; 112; 116; 163; 181].

The effect of discontinuous delta layers of Fe impurities within thin Pt films is studied here. The motivation behind this work is two-fold; the work in chapter 4 shows that impurity  $\delta$ -layers play a role in the ordinary Hall effect (OHE) for thin films doped with discontinuous layers of both magnetic and non-magnetic impurities with high spin-orbit coupling (SOC). The position dependence of a discontinuous layer of magnetic impurities on the anomalous and ordinary Hall effects is investigated here as an extension of this study in a Pt host. The second part of the motivation lies with some anomalous magnetotransport behaviour found in recent literature in YIG/Pt bilayers [21; 22; 58; 112; 163] and an ongoing debate in the literature about whether the MPE could play a role. To complement this study, the magnetotransport of YIG/Pt bilayers under various preparation conditions are studied in chapter 6. To simulate the MPE, and to understand the implications for the magnetotransport of localised magnetic impurities within Pt, discontinuous layers of Fe are deposited on an  $\text{Al}_2\text{O}_3$  substrate prior to the deposition of ultrathin Pt. In this chapter, the various magnetotransport phenomena that result are discussed in detail.

## 5.2 Magnetotransport of thin and ultrathin Pt films

In this section, the magnetotransport of both thin and ultrathin, 2D, films of Pt is investigated. An ultrathin film is one whose thickness is much smaller than the mean free path of the conduction electrons in the material; for bulk Pt, this is around 10-13 nm [182]. The film thicknesses are chosen to be 22 nm, as this is sufficiently large

## 5.2 Magnetotransport of thin and ultrathin Pt films

to remove finite size effects and mesoscopic phenomena from low temperature magnetotransport, as demonstrated here, and 2 nm to probe quantum interference effects. These films are deposited via dc magnetron sputtering and are hence nanocrystalline in nature; this means that the substrate texture direction plays very little role in the structure of the films.

### 5.2.1 Resistivity as a function of temperature

Before beginning a study on the effects of magnetic impurities within thin films, it is first prudent to ensure the quality of the source material and determine the innate concentration of any pre-existing magnetic impurities. The prevalent method for determining this is via measurements of the Kondo effect, where the resistivity of a metallic sample increases at low temperatures due to scattering from magnetic impurities [146], as discussed in section 2.8. It is known that Fe impurities within Pt exhibit spin-fluctuation behaviour in very dilute concentrations, leading to a logarithmic increase in the resistivity at low temperatures [159; 180; 183]. This allows one to determine if the concentration of impurities has surpassed a particular threshold [159].

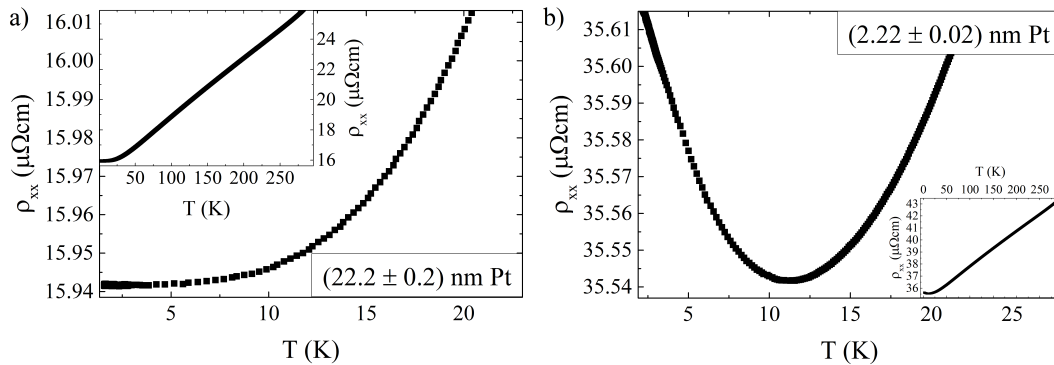


Figure 5.1: The resistivity as a function of temperature for a)  $(22.2 \pm 0.2)$  nm Pt deposited on an  $\text{Al}_2\text{O}_3$  substrate and b)  $(2.22 \pm 0.02)$  nm Pt deposited on a YAG substrate via dc magnetron sputtering. The insets show the full temperature range, while the main figures show the low temperature regions where an upturn is visible in b) but not a). All measurements are taken in zero magnetic field.

## 5.2 Magnetotransport of thin and ultrathin Pt films

---

Fig. 5.1a) shows the resistivity of  $(22.2 \pm 0.2)$  nm Pt deposited via dc magnetron sputtering onto an  $\text{Al}_2\text{O}_3$  substrate, as a function of temperature. The value of the resistivity is consistent with that found in recent work for 20 nm Pt; the value reported is around  $20 \mu\Omega\text{cm}$  [34] while the values found in this sample vary in the approximate range  $16\text{-}26 \mu\Omega\text{cm}$ . It is expected that this film will have a slightly higher resistivity compared to the reported value, as that sample was annealed at high temperatures, whereas this film was not. This value hence signifies a high quality polycrystalline film of Pt.

Fig. 5.1a) shows the low temperature region of the resistivity data. No upturn is visible, signifying a lack of any spin fluctuation or Kondo effects and hence an absence of significant quantities of magnetic impurities, consistent with the quoted source material purity of 99.99 %. This means that any upturn observed upon the introduction of magnetic dopants is due entirely to the concentration added. This concurs with the value of the resistivity to suggest the Pt grown by dc magnetron sputtering is of high quality.

Fig. 5.1b) shows the resistivity of  $(2.22 \pm 0.02)$  nm Pt deposited via dc magnetron sputtering onto a  $\text{Y}_3\text{Al}_5\text{O}_{12}$  (YAG) substrate, as a function of temperature. The value of the resistivity observed is much larger than for the  $(22.2 \pm 0.2)$  nm sample shown in fig. 5.1a), varying in the approximate range  $36\text{-}53 \mu\Omega\text{cm}$  in the samples used here. This is consistent with experimental values in the literature [184]. This larger value is a consequence of the film becoming ultrathin, i.e. much thinner than the mean free path, and therefore susceptible to quantum interference effects. The reduced cross-sectional area leads to a higher number of interfacial scattering events as the thickness of the film is significantly smaller than the expected mean free path for conduction electrons within the Pt film [29; 184].

The data in fig. 5.1b) show a clear increase in the resistivity at low temperature, with a minimum value at  $(11.2 \pm 0.4)$  K. The resistivity below the minimum increases in proportion to  $\ln T$ , consistent with three phenomena outlined in chapter 2: the Kondo effect, as per equation 2.50 [146]; quantum interference, as per equation 2.34, where

## 5.2 Magnetotransport of thin and ultrathin Pt films

$\tau_i = \beta T^{-p}$  contains the temperature dependence [122], and the enhanced electron-electron interaction, as per equation 2.38. None of these phenomena can fully describe the data on their own, however. If values from the literature for ultrathin Pt are used to simulate to effect of quantum interference, weak anti-localisation is observed with a decrease in the resistivity at low temperatures. Even with very low screening, the enhanced electron-electron interaction alone cannot explain the data. Only when both theories are combined can a fit to these data be obtained. This fit is shown in fig. 5.2a) with the electron-electron power law shown in fig. 5.2b).

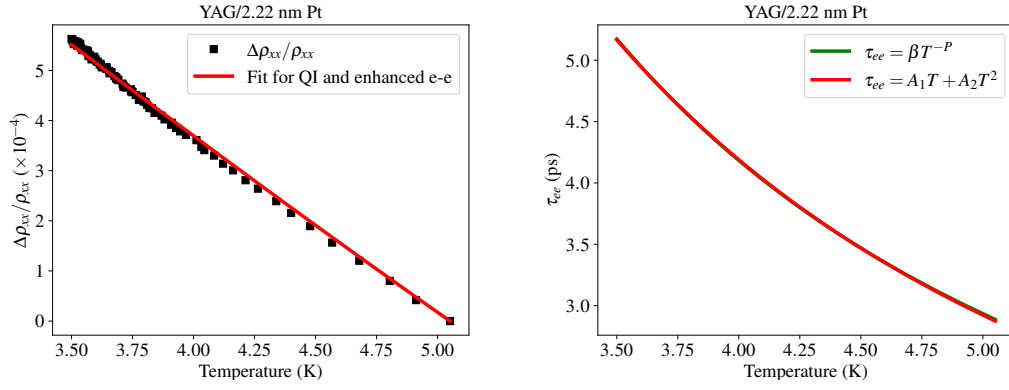


Figure 5.2: The resistivity data from fig. 5.1b) is fitted on the left with equation 2.34 whilst on the right the values found from use of equation 2.35 are fitted with equation 2.37.

The film is expected to be two dimensional due to its thickness being much shorter than the expected mean free path and therefore the two dimensional expressions for weak localisation and electron-electron interaction discussed in section 2.6.1 are used in fig. 5.2. The only way to obtain a fit is to add together the two contributions: quantum interference and electron-electron interaction.

As well as  $\tau_{so}$ , the temperature dependence of the electron-electron interaction time,  $\tau_{ee}$  is obtained. For  $\tau_{ee}$  we can fit equation 2.35 to learn whether the samples are clean and follow Fermi liquid behaviour, or whether they have an enhanced interaction. As can be seen from table 5.1,  $A_1$  is much greater than  $A_2$ , indicating that the  $\tau_{ee}$  is enhanced by the 2D nature of the sample when compared to the bulk-like contribution, which goes as  $T^2$ . The parameters obtained from this fit are shown in table 5.1 below. The value obtained for  $\tau_{so}$  is larger than expected by a factor of 10. However, to

## 5.2 Magnetotransport of thin and ultrathin Pt films

Table 5.1: Parameters for the fits of quantum interference and the enhanced electron-electron interaction in fig. 5.2.

Sample	$\tau_{\text{so}}$ (ps)	$\rho_{xx}$ ( $\mu\Omega\text{cm}$ )	$F$	$L_{\text{so}}$ (nm)	$\lambda$ (nm)
YAG/2.22 nm Pt	$6\pm 4$	$30\pm 3$	$0.36\pm 0.01$	$30\pm 3$	$11\pm 1$
Sample	$\beta(\times 10^{-10})$	$P$	$A_1(\times 10^{10} \text{ s/K})$	$A_2(\times 10^{10} \text{ s/K}^2)$	
YAG/2.22 nm Pt	$0.38\pm 0.09$	$1.59\pm 0.05$	$2.470\pm 0.008$	$0.874\pm 0.002$	

make sense of this number, we need the diffusion constant to find the lengthscale of the spin-orbit scattering. The value from the bulk heat capacity has been used which then gives scattering lengths of the order of 30 nm (see table 5.1); an order of magnitude too high.  $D$  is also calculated from the Fermi velocity and the mean free path which increases its value from that obtained from the heat capacity by an order of magnitude. The value of  $D$  hence cannot be constrained very well. The data of fig. 5.2b) show similarities with those found for AuPd alloys [136]. For samples with  $\rho_{xx} < 1 \mu\Omega\text{cm}$ , hence deemed to be clean [123], values of between 10-30 ps have been found [120]. The longer lifetimes indicated by these data hence suggest a smaller contribution from this effect to the transport.

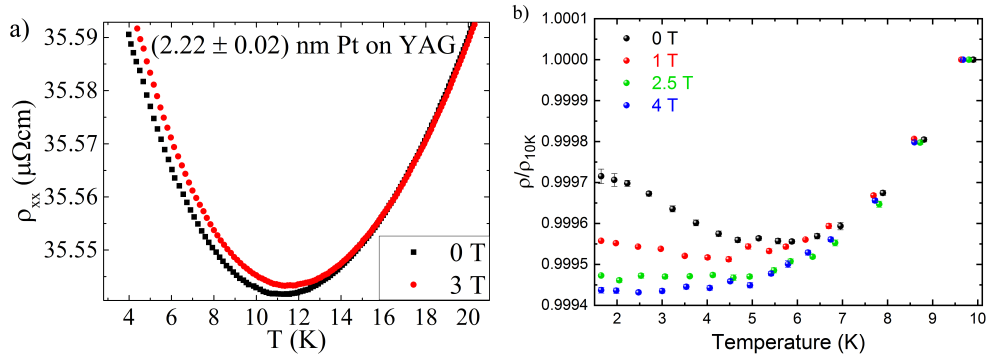


Figure 5.3: The resistivity as a function of temperature for a)  $(2.22 \pm 0.02)$  nm Pt on YAG cooled in zero field (black squares) and an applied field of 3 T (red circles) and b) Ag with a dilute amount of magnetic impurities, cooled in various fields, relative to the resistivity at 10 K. Graph b) courtesy of [185].

The third logarithmic temperature dependence mentioned is the Kondo effect. The absence of a resistivity minimum in the  $(2.22 \pm 0.2)$  nm data indicate the source ma-

## 5.2 Magnetotransport of thin and ultrathin Pt films

---

terial is of high purity and hence the minimum observed for  $(2.22 \pm 0.02)$  nm Pt is not due to the Kondo effect from source material impurities. While the substrates for the two films are different, neither contain magnetic elements and as such the Kondo effect should not be induced from this difference. The application of a magnetic field when cooling the sample works to destroy the Kondo effect; this can be seen in fig. 5.3b) for Ag films; the resistivity increases less with the application of greater fields below  $T_{\min}$  until standard metallic behaviour is observed at 4 T. In order to fully remove the Kondo effect from the data, the ultrathin sample was cooled in a field of 3 T; these data are shown in fig. 5.3a) alongside the zero field data. It can be seen that the opposite effect occurs; there is a larger increase in the resistivity below  $T_{\min}$  when a field is applied out of the sample plane, indicating quantum interference effects.

### 5.2.2 Conventional magnetoresistance

The change in resistance as a function of field, i.e. the conventional magnetoresistance (MR), of thin Pt films is considered. In order to separate any intrinsic effects from Pt, it is prudent to consider the MR in both thin and ultrathin films of Pt; this enables the contribution of quantum interference effects to the MR to be better understood. The MR is discussed for the perpendicular orientation, where the field is oriented out of the plane of the sample. This are illustrated in fig. 3.6, and is the orientation most of interest when studying quantum interference effects.

Fits of quantum interference phenomena are applied to the data in fig. 5.4 from equation 2.40 and are displayed as solid lines. The variation of the characteristic magnetic fields as a function of temperature are displayed in fig. 5.5. Using  $D = 33 \text{ cm}^2/\text{s}$ , from the mean free path, it is found that  $\tau_{\text{so}}$  varies in the range  $0.8\text{-}6.0 \times 10^{-13} \text{ s}$ , in line with expectation from the spin diffusion length [110; 186]. The value of  $B_i$  is found to increase from low temperatures, as one would expect for electron-electron interaction followed by increased phonon scattering. The values of  $B_s$ ,  $B_{\text{so}}$  and  $B_o$  for the magnetic, spin-orbit and elastic contributions, respectively, are not expected to vary with temperature [122] and this is what has been found for the clean Pt sample. The data show that weak anti-localisation can explain this data and obtain reasonable values for

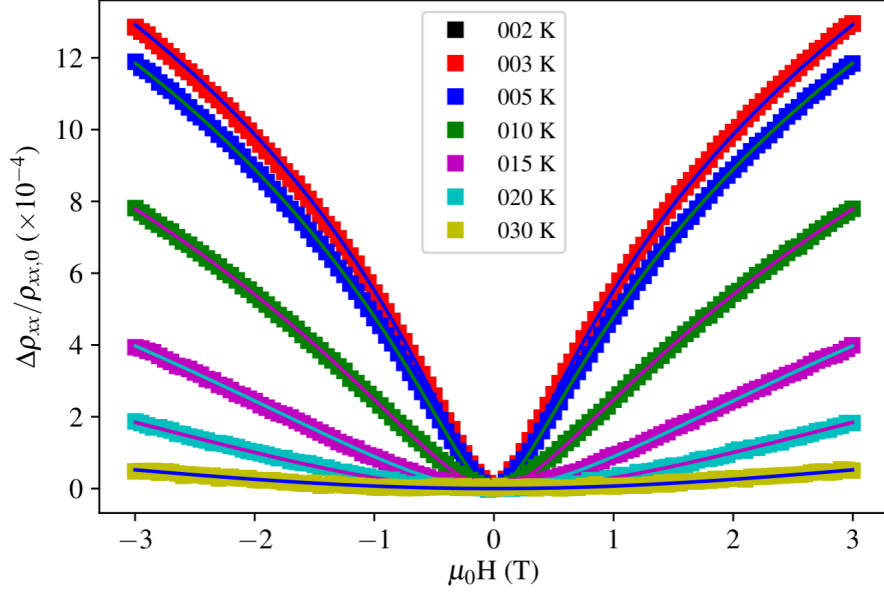


Figure 5.4: The perpendicular magnetoresistance for  $(2.22 \pm 0.02)$  nm Pt on a YAG substrate, plotted as a function of both applied magnetic field and temperature up to 50 K. Please note the curves for 2 K and 3 K overlap significantly with the point size chosen.

$\tau_{\text{so}}$ . The electron-electron interaction leads to a small magnetoresistance which is neglected in this thesis.

The temperature dependence of the magnitude of the field-dependent MR are shown in fig. 5.6 for both thin and ultrathin Pt. In both cases, the MR in all three orientations is seen to be negligibly small above 50 K. Below 50 K, an increase to a positive MR in all orientations is observed in both samples, with the largest being for the perpendicular orientation due to quantum interference effects in the ultrathin film.

### 5.2.3 Angle-dependent magnetoresistance

The angle-dependent magnetoresistance (ADMAR) for thin films of Pt on a non-magnetic substrate remains largely unexplored in modern literature, yet plays a role in the measured values of the SHMR and AMR quoted for YIG/Pt bilayers. Here, the intrinsic effects from Pt are studied in order to understand the contribution of finite size effects

## 5.2 Magnetotransport of thin and ultrathin Pt films

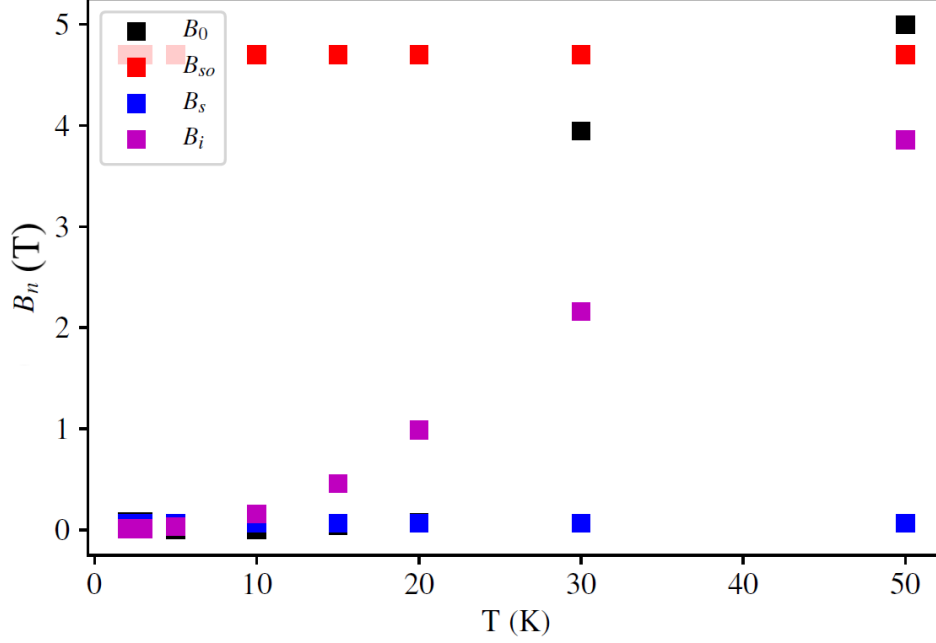


Figure 5.5: The various characteristic fields for scattering types used in the weak localisation model of the perpendicular magnetoresistance. Uncertainties are plotted as error bars but are smaller than the point size used.

to the magnitude of the ADMR at high fields. A film thickness of around 2 nm is chosen for this study, as this has been found to be optimum in studies of the SHMR in YIG/Pt bilayers [17; 113; 160; 161]. A control sample of a larger thickness is used to isolate quantum interference effects. In angle dependent measurements on YIG, a field is applied while the samples are rotated in three measurement planes, outlined in section 3.5.2. A large field is applied in order to maximise the magnitude and allow small ADMR to be measured above the experimental noise. Examples of the rotation are shown in fig. 5.7.

Fig. 5.7 shows that in the  $\alpha$ -plane at a temperature of 5 K and an applied field of 3 T, an angle-dependent magnetoresistance with a cosine squared dependence on the angle manifests. The data in fig. 5.8 represent a combination of measurements of the full angle-dependence and of differences between the relative conventional MRs which were measured, at an applied field of 3 T.

## 5.2 Magnetotransport of thin and ultrathin Pt films

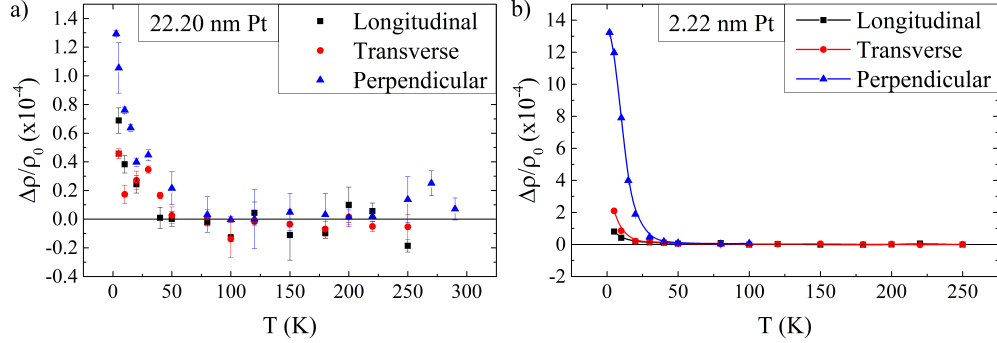


Figure 5.6: The magnitude of the longitudinal, transverse and perpendicular magnetoresistances at an applied field of 3 T are shown here as a function of temperature. The samples under study are a)  $(22.2 \pm 0.2)$  nm Pt on an  $\text{Al}_2\text{O}_3$  substrate and b)  $(2.22 \pm 0.02)$  nm Pt on a YAG substrate. Lines shown are guides to the eye.

The ADMRs in all three orientations are shown for both thin and ultrathin Pt in figs. 5.8a) and 5.8b) respectively. As the MR in all three orientations and both samples was found to be negligible above 50 K, so too is the ADMR in all three orientations. In the thicker sample, a small positive value is observed below 30 K in the  $\alpha$ -plane. The  $\beta$ -plane exhibits a small positive magnitude below 50 K. The  $\gamma$ -plane, where AMR is typically measured, exhibits a negative value below 50 K. The magnitudes of all these ADMRs are of the order of  $10^{-5}$  and are thus much smaller than reported values of SHMR or AMR in YIG/Pt bilayers. Their origins are in the magnetoresistance observed at low temperatures in Pt, and as such the mechanisms are far removed from those of SHMR and AMR.

The ultrathin Pt sample, shown in fig. 5.8b), develops ADMRs with much larger magnitudes, of the order of  $10^{-4}$ ; this is much more significant for measurements of the SHMR and AMR. Quantum interference effects play a large role in increasing these values, and once again the mechanisms behind these signals are not the same as for SHMR and AMR; they only contribute to the value through the method used to measure them. A positive signal with a cosine squared dependence which is in phase with SHMR emerges in the  $\beta$ -plane below 30 K, to a maximum magnitude of  $(8.07 \pm 0.03) \times 10^{-4}$  at 5 K. This is even larger than the SHMR measured in YIG/Pt

## 5.2 Magnetotransport of thin and ultrathin Pt films

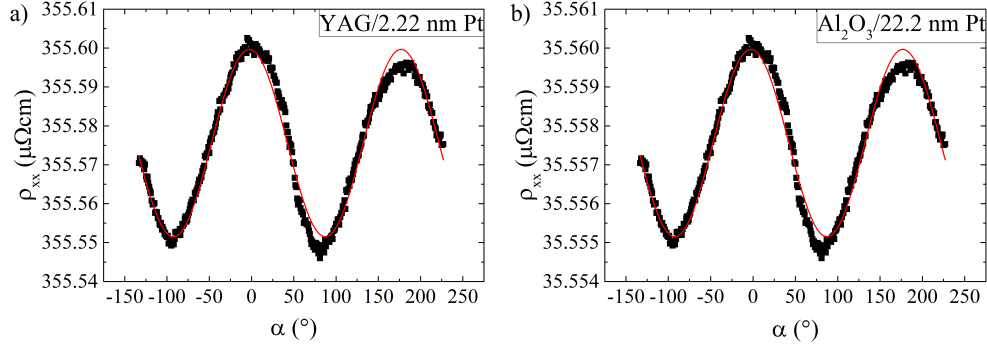


Figure 5.7: The angle-dependent magnetoresistance at a temperature of 5 K and applied field of 3 T in the  $\alpha$ -plane for a)  $(2.22 \pm 0.02)$  nm Pt on YAG and b)  $(22.2 \pm 0.2)$  nm Pt on  $\text{Al}_2\text{O}_3$ . Red lines show cosine squared fits to the data. Amplitudes are plotted in fig. 5.8 as a function of temperature.

bilayers in some cases [110], and is an effect that has not been taken into account as of yet. The  $\gamma$ -plane exhibits a large negative ADMR below 30 K, to a maximum magnitude of  $-(9.48 \pm 0.03) \times 10^{-4}$  at 5 K. This corresponds to a negative AMR signal if current measurement formalism is applied [22; 23; 181]. The  $\alpha$ -plane is used to measure the sum of SHMR and AMR signals, and in this case represents the sum of the  $\beta$  and  $\gamma$  ADMRs well with a magnitude of  $-(1.285 \pm 0.007) \times 10^{-4}$ .

The magnitude of the ADMR is strongly dependent upon the field, and is a product of the weak anti-localisation observed at reduced thicknesses. The increases in the  $\beta$ - and  $\gamma$ -plane magnitudes below 30 K are attributed to weak anti-localisation via the magnetoresistance fitting. These trends are explored in dilute PtFe alloys and YIG/Pt bilayers later in this thesis to elucidate a mixture of complex effects.

### 5.2.4 The Hall effect

The Hall effect measured in both thin and ultrathin Pt is another method to determine the quality of the films and any contribution to the Hall effect from quantum interference effects. In both samples, the ordinary Hall effect is observed, which is due to the Lorentz force and described in section 2.4. The sign of the Hall effect is negative, as expected for electron charge carriers in a metallic sample. The Hall resistivity

## 5.2 Magnetotransport of thin and ultrathin Pt films

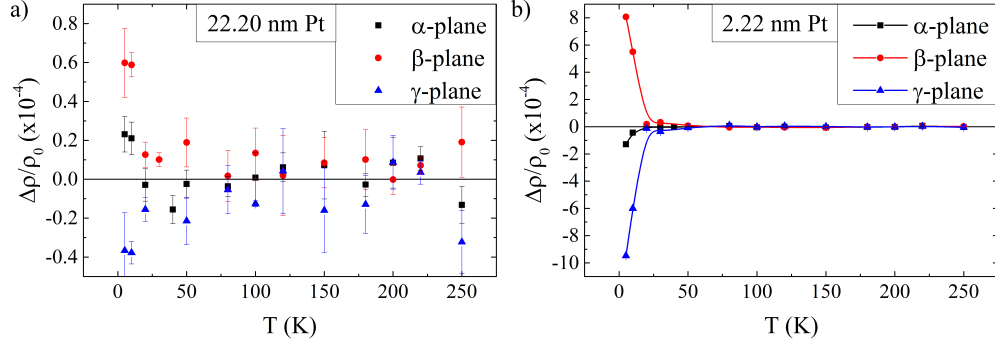


Figure 5.8: *The temperature dependence of the magnitude of the angle-dependent magnetoresistance taken at an applied magnetic field magnitude of 3 T for a)  $(22.2 \pm 0.2)$  nm Pt on  $Al_2O_3$  and b)  $(2.22 \pm 0.02)$  nm Pt on YAG. The planes are as outlined in section 3.5.2, with  $\alpha$  being the  $x$ - $y$  plane,  $\beta$  the  $y$ - $z$  and  $\gamma$  the  $x$ - $z$ . Lines shown are guides to the eye.*

over the entire field range is used to calculate the ordinary Hall coefficient,  $R_H$ , as the dependence on field is entirely linear. Further detail regarding the extraction of Hall coefficients from raw data can be found in section 3.5.3. Representative examples are shown at a temperature of 5 K in fig. 5.9.

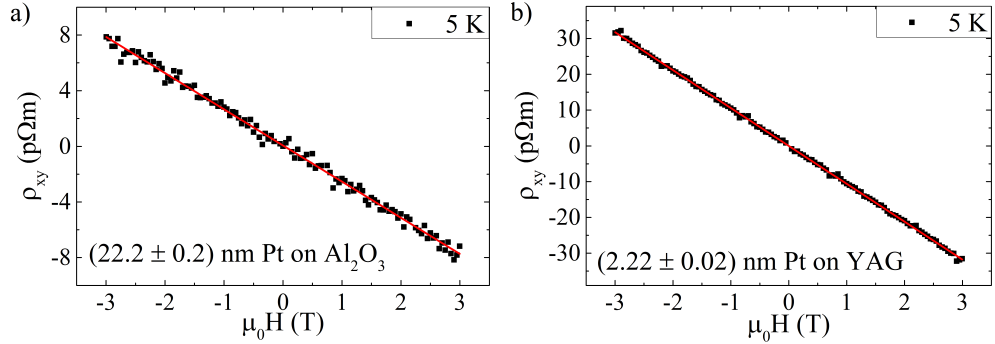


Figure 5.9: *The Hall resistivity as a function of field with linear fit is shown for a)  $(22.2 \pm 0.2)$  nm Pt on  $Al_2O_3$  and b)  $(2.22 \pm 0.02)$  nm Pt on YAG at a temperature of 5 K.*

The temperature dependences of the ordinary Hall coefficient for thin and ultrathin films of Pt are shown in figs. 5.10a) and 5.10b) respectively. The shape of the temperature dependence is similar in both cases, with a decrease in magnitude below 30 K. This behaviour cannot be attributed to weak anti-localisation, as it is present in

## 5.2 Magnetotransport of thin and ultrathin Pt films

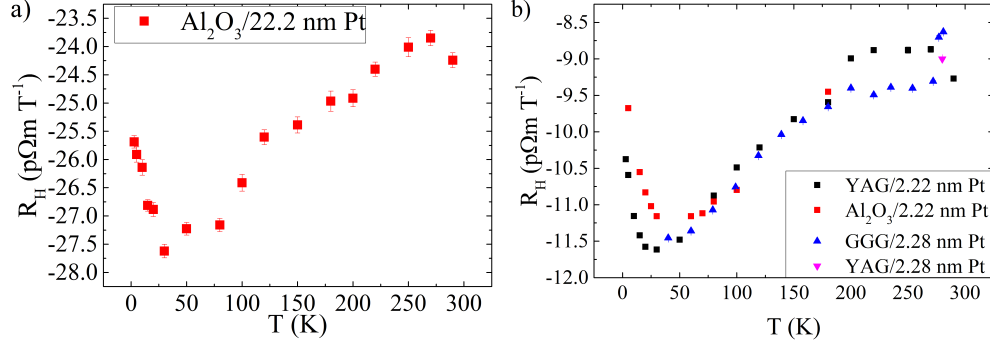


Figure 5.10: The magnitude of the ordinary Hall coefficient plotted as a function of temperature for a)  $\text{Al}_2\text{O}_3/22.2$  nm Pt and b) approximately 2 nm Pt deposited on various substrates; see the legend for more details.

the thicker sample also. The magnitude of  $R_H$  is, however, quite different for thin and ultrathin films. The value of  $R_H$  for a thin film is consistent with values in the literature [187; 188]. The ultrathin sample has a much larger magnitude, however. This is consistent with trends previously observed for very thin films of Pt [189]. Here, the Hall coefficient at room temperature decreases in magnitude from  $-(24.2 \pm 0.1)$   $\text{p}\Omega\text{m T}^{-1}$  for the  $\text{Al}_2\text{O}_3/22.2$  nm Pt sample to  $-(9.27 \pm 0.02)$   $\text{p}\Omega\text{m T}^{-1}$  for the YAG/2.22 nm sample Pt studied throughout this section. There are changes in the position of the minima and in the magnitude of the Hall coefficient for the samples plotted in fig. 5.10b). These are most likely due to small variations in the sample thickness; two films have a quoted thickness of  $(2.22 \pm 0.02)$  nm whilst the others have a thickness of  $(2.28 \pm 0.02)$  nm. Those samples with the same quoted thickness are similar in magnitude; more data are required to determine if the minima remain consistent.

The data represented in this section hence demonstrate that the Pt grown by dc magnetron sputtering for the purposes of this thesis is of high quality and provides magnetotransport results which exhibit a mixture of enhanced electron-electron interaction and quantum interference effects in the ultrathin regime.

## 5.3 Interfacial Fe doping in the magnetotransport of ultrathin Pt films

Various concentrations of Fe were deposited as a discontinuous layer prior to the deposition of 2 nm of Pt via dc magnetron sputtering. *In-situ* deposition in a high vacuum environment allows for exceptionally clean samples. Sapphire ( $\text{Al}_2\text{O}_3$ ) is the substrate of choice for this study, as thermally oxidised silicon has been found to greatly increase the resistance of ultrathin films of Cu; well above that observed when using an  $\text{Al}_2\text{O}_3$  substrate. This large increase in resistivity from Si made the measurement of Cu films thinner than 4 nm impossible in the preparation of fig. 4.1. Sapphire provides a single crystal surface; due to the preparation methods used in producing the substrates, small steps are present on the surface [190]. The Fe may hence preferentially settle into these during sputtering. The data do not reflect formation of continuous wires on the surface, however. By localising impurities on the surface of the substrate, the effect of localised magnetic ions on the surface of YIG is emulated, enabling this to be compared to the data presented in chapter 6. It also poses interesting questions for the scattering physics which are rarely explored in such a localised manner.

A pause time of 0.1 s was used in order to deposit approximately 4 % of a monolayer (ML) of Fe. This coverage approximation is based on the growth rate of  $(0.089 \pm 0.005) \text{ nm s}^{-1}$ , found from x-ray reflectivity of thicker calibration samples, depositing a thickness of Fe which equates to around 4 % of the lattice constant of Fe in 0.1 s. A pause time of 0.2 s was then assumed to deposit 8 % ML of Fe. A further experiment was performed where, during growth, the substrate was moved over the Fe source and away again, without a scheduled pause, prior to the deposition of Pt. This is represented as  $\delta\text{Fe}$ , as the coverage of this technique was not determinable by the techniques employed in the preparation of this thesis. In order to determine the coverage of  $\delta\text{Fe}$ , transmission electron microscopy (TEM) could be used, although this proved unfruitful in previous studies [106]. The superSTEM facility has a much higher resolution microscope and hence may be able to determine the coverage. This is left to future work. This amount of Fe is deposited in addition to any during a pause time, and hence is always present in addition to the coverage quoted for samples with higher Fe concentration. Measurements of this sample allow for a concentration study of the

magnetotransport effects.

#### 5.3.1 Resistivity as a function of temperature

The resistivities of the various concentrations of interfacial Fe are plotted in Fig. 5.11. The values are normalised to the resistivity at the minimum as follows

$$\rho_{\text{norm}} = \frac{\rho(T) - \rho_{\text{min}}}{\rho_{\text{min}}} \quad (5.1)$$

where  $\rho_{\text{norm}}$  is the normalised resistivity value plotted,  $\rho(T)$  is the value of the resistivity at a particular temperature,  $T$ , and  $\rho_{\text{min}}$  is the value of the resistivity at the minimum. The sample of YAG/2.22 nm Pt is used as a control sample, and its properties are discussed in more detail in section 5.2; the minimum in resistivity is here entirely due to weak anti-localisation. When a small amount of impurities is added between the Pt film and the substrate, the temperature at which the minimum occurs,  $T_{\text{min}}$ , increases. As the amount of impurities added is increased, so too does  $T_{\text{min}}$ , indicating this increase is due to the concentration of magnetic impurities.

The sample with  $\delta\text{Fe}$  deposited beneath Pt has a slightly greater thickness of 2.28 nm compared to the other samples with a quoted thickness of  $(2.22 \pm 0.02)$  nm. This difference in thickness is far less than one ML, and is considered to have only a very small effect on concentration dependent phenomena. It is known that the  $\delta\text{Fe}$  sample has the smallest concentration of impurities due to the nature of its growth, and this is confirmed in the magnetotransport data.

The concentration dependence of  $T_{\text{min}}$  indicates the presence of a Kondo effect or spin fluctuation behaviour [146; 158; 159]. Below the minimum, the resistivity increases in proportion to  $\ln T$  for all samples; from the clean Pt study it is known that this behaviour cannot be explained by the enhanced electron-electron interaction with a negative contribution from weak anti-localisation alone. It is therefore difficult to extract concentration data from these curves. If the effect exhibited were the Kondo effect alone, there are methods to determine the concentration of impurities, but a successful method of removing the contribution of weak anti-localisation and the enhanced

### 5.3 Interfacial Fe doping in the magnetotransport of ultrathin Pt films

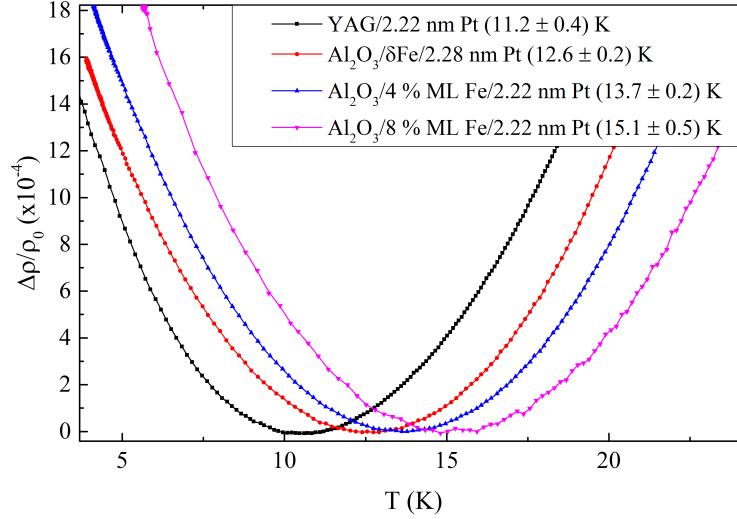


Figure 5.11: *The normalised resistivity as a function of temperature at low temperatures of various concentrations of Fe beneath an ultrathin Pt film. Lines shown are guides to the eye. The temperatures displayed in the legend represent the temperatures at which the resistivity minima occur for each sample.*

electron-electron interaction to determine this has yet to be found [154–157]. In addition, the relative changes at low temperature scale with data for other samples, as shown in fig. 5.12.

This scaling would seem to indicate that the Kondo effect cannot fully explain the data, either. With future work, these data could help build a model for the specific case of Fe impurities within Pt, localised at the interface, as the concentration is controlled. For systems without a deliberate addition of impurities, such a model would prove imperative in understanding the transport of these systems, such as YIG/Pt bilayers discussed in chapter 6.

#### 5.3.2 Conventional magnetoresistance

As described in section 5.2.2, the MR is explored here for two samples of Pt interfacially doped with Fe on an  $\text{Al}_2\text{O}_3$  substrate. Both Pt thicknesses are 2 nm, but the Fe concentration is 4 % ML Fe in one sample and  $\delta\text{Fe}$  in the other, as described at the

### 5.3 Interfacial Fe doping in the magnetotransport of ultrathin Pt films

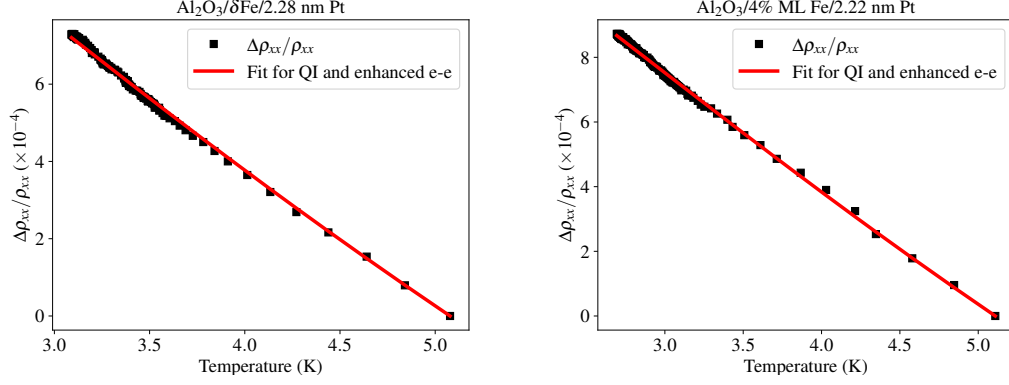


Figure 5.12: The fits to the resistivity data below  $T_{\min}$  for a)  $\text{Al}_2\text{O}_3/\delta\text{Fe}/2.22 \text{ nm Pt}$  and b)  $\text{Al}_2\text{O}_3/4 \text{ \% ML Fe}/2.28 \text{ nm Pt}$ , using both quantum interference and the enhanced electron-electron interaction.

Table 5.2: Parameters for the fits of quantum interference and the enhanced electron-electron interaction in figs. 5.2 and 5.12.

Sample	$\tau_{\text{so}}$ (ps)	$\rho_{xx}$ ( $\mu\Omega\text{cm}$ )	$F$	$L_{\text{so}}$ (nm)	$\lambda$ (nm)
YAG/2.22 nm Pt	$6\pm 4$	$30\pm 3$	$0.36\pm 0.01$	$30\pm 3$	$11\pm 1$
$\text{Al}_2\text{O}_3/\delta\text{Fe}/2.28 \text{ nm Pt}$	$7\pm 3$	$30\pm 3$	$0.318\pm 0.005$	$34\pm 3$	$14\pm 1$
$\text{Al}_2\text{O}_3/4 \text{ \% ML Fe}/2.22 \text{ nm Pt}$	$7\pm 2$	$30\pm 3$	$0.332\pm 0.005$	$33\pm 3$	$13\pm 1$
Sample	$\beta$ ( $\times 10^{-10}$ )	$P$	$A_1$ ( $\times 10^{10} \text{ s/K}$ )	$A_2$ ( $\times 10^{10} \text{ s/K}^2$ )	
YAG/2.22 nm Pt	$0.38\pm 0.09$	$1.59\pm 0.05$	$2.470\pm 0.008$	$0.874\pm 0.002$	
$\text{Al}_2\text{O}_3/\delta\text{Fe}/2.28 \text{ nm Pt}$	$0.32\pm 0.6$	$1.65\pm 0.05$	$2.58\pm 0.01$	$1.320\pm 0.004$	
$\text{Al}_2\text{O}_3/4 \text{ \% ML Fe}/2.22 \text{ nm Pt}$	$0.34\pm 0.04$	$1.63\pm 0.05$	$2.32\pm 0.01$	$1.200\pm 0.003$	

start of section 5.3.

Fig. 5.14 shows the perpendicular MR for the two concentrations of Fe as a function of temperature. Solid lines show fits to the theory of quantum interference phenomena described in section 2.6.2. Qualitatively, these fits appear to describe the data rather well. The quantitative picture is different, however. Even in calculations performed with various input parameters, the data could only be fit when  $\tau_{\text{so}}$  was much greater than the  $10^{-13} \text{ s}$  magnitude expected from both the spin diffusion length [110] and the fits to the undoped data in fig. 5.4. The negative magnetoresistance requires a non-zero  $B_S$  value and a low  $B_{\text{so}}$  value in conjunction. The remainder of the fields

### 5.3 Interfacial Fe doping in the magnetotransport of ultrathin Pt films

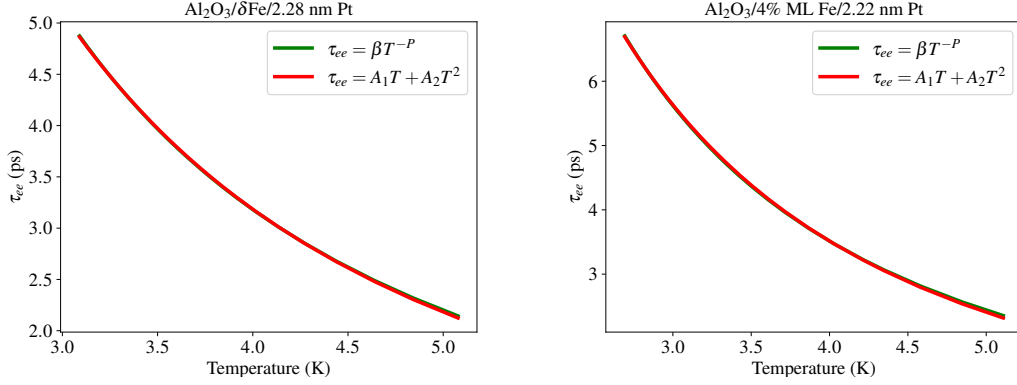


Figure 5.13: The fits to the power law found from fig. 5.12 for the inelastic scattering time in a)  $\text{Al}_2\text{O}_3/\delta\text{Fe}/2.22 \text{ nm Pt}$  and b)  $\text{Al}_2\text{O}_3/4\% \text{ ML Fe}/2.22 \text{ nm Pt}$ . Parameters are shown in table 5.3.1 below.

follow no set pattern, with fields varying between 0 – 2.5 T for the 4 % ML sample, and between 0 – 7 T for the  $\delta\text{Fe}$  sample. This could be an interesting new effect; the interplay between spin-orbit effects and the insertion of a magnetic layer at the interface. This has not been studied before; impurities added in previous work were dispersed and usually within thicker samples. Kondo MR has previously been thought to be suppressed in the ultrathin regime [191] and resistivity scaling data appear to suggest the Kondo effect is not the prevalent mechanism for the upturn in resistivity at low temperatures, as per fig. 5.12. This combination of phenomena has not been able to be fully explained in the literature previously, and this thesis is no exception [135].

The temperature dependence of the MR in the three different orientations are shown in Fig. 5.15. The presence of Fe is seen to cause a change in sign of the magnetoresistance in all three orientations at low temperatures compared to the clean Pt case shown in fig. 5.6. This is predicted to occur through magnetic scattering in the quantum interference effect [122; 123; 180]. A higher concentration of Fe results in a sign change of the MR at a higher temperature in all three orientations. Both the positive longitudinal and perpendicular MRs have a larger magnitude for a higher concentration, as well as all three negative MRs at low temperatures having a larger magnitude for the higher concentration. The literature currently lacks a study of interfacial doping in this manner, with current theory applicable to exchange enhancement and magnetic ordering of

### 5.3 Interfacial Fe doping in the magnetotransport of ultrathin Pt films

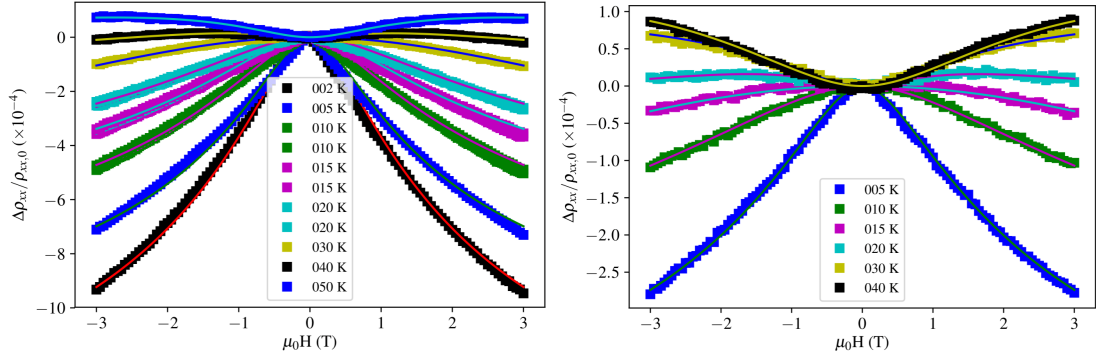


Figure 5.14: *The perpendicular magnetoresistance as a function of temperature and field for a)  $Al_2O_3/4\%$  ML Fe/2.22 nm Pt and b)  $Al_2O_3/\delta$ Fe/2.28 nm Pt. The solid lines show fits using the quantum interference equations from section 2.6.2. Please note panel a contains repeats at 10 K, 15 K and 20 K which overlap significantly but can be viewed more clearly when zoomed in.*

large moments distributed throughout a dilute alloy [180]. This case is quite specific, and there exists a gap in the theory landscape which makes it difficult to extract concentration and other information from these data.

#### 5.3.3 Angle-dependent magnetoresistance

The angle-dependent MR for the two samples interfacially doped with Fe are shown as a function of temperature in fig. 5.17. Measurements were performed in the geometry described in 3.5.2 with an applied field of 3 T. Representative data are shown in fig. 5.16.

The ADMR for ultrathin Pt with  $\delta$ Fe beneath is shown in fig. 5.17b). The  $\alpha$ ,  $\beta$  and  $\gamma$  plane MRs are seen to fluctuate with large uncertainty around zero magnitude above 50 K, and are hence deemed to be negligible. Below 50 K, however, there exists an increase and positive MR in all three planes. For the  $\alpha$  and  $\beta$  planes, this bears similarities to the trend observed for a thin Pt film shown in fig. 5.8a). The  $\alpha$  and  $\gamma$  plane MRs are positive for the  $\delta$ Fe doped sample, in contrast to the negative effects observed in these planes for ultrathin Pt, shown in fig. 5.8b). The replacement of weak anti-localisation with weak localisation due to the presence of magnetic impurities is part

### 5.3 Interfacial Fe doping in the magnetotransport of ultrathin Pt films

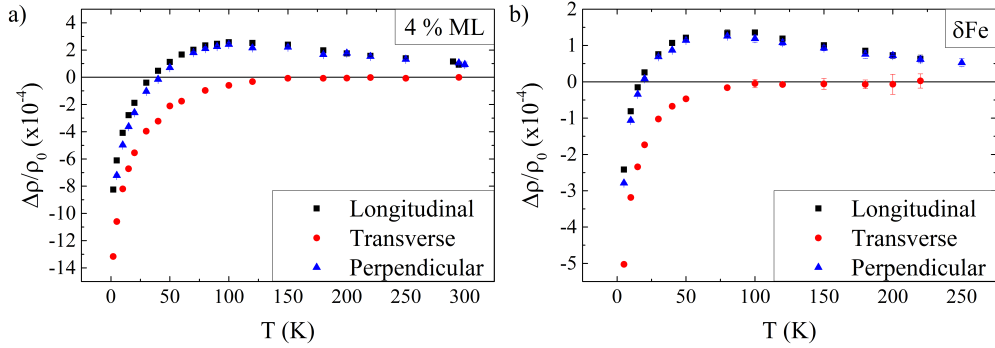


Figure 5.15: The magnitude of the MR at an applied field of 3 T as a function of temperature in the longitudinal, transverse and perpendicular orientations. The sample structures are a)  $Al_2O_3/4\% \text{ ML Fe}/2.22 \text{ nm Pt}$  and b)  $Al_2O_3/\delta\text{Fe}/2.28 \text{ nm Pt}$ .

of the reason for this. However, the  $\gamma$  plane MR was also negative for a thin Pt film without quantum interference effects. This would suggest that at low temperatures, scattering from magnetic impurities causes a positive ADMR in all three orientations. Its magnitude is larger in the  $\alpha$  and  $\beta$  planes than for thin Pt, but doesn't reach the large magnitudes caused by weak anti-localisation in pure ultrathin Pt.

Fig. 5.17a) shows the angle-dependent MR for the sample of Pt with 4% ML Fe beneath, and this exhibits a large positive MR in the  $\alpha$  and  $\beta$  planes over the entire temperature range. As the geometry of the  $\beta$  plane is the standard method to measure the SHMR [17; 110; 113], this has implications for measurements on magnetic insulators, further explored in chapter 6. MR in the  $\gamma$  plane is the standard method by which the AMR is measured in ferromagnetic materials. A small signal is apparent in this plane only at low temperatures, which is in agreement with AMR measurements in YIG/Pd bilayers in the literature [118]. This same mechanism of scattering cannot be responsible for the MR observed in the  $\beta$  plane at higher temperatures, as it is obscured by phonon scattering.

Above 50 K, the MR in the  $\beta$  plane for 4% ML Fe beneath ultrathin Pt has a strong dependence on the temperature. Below this temperature, the dependence is complicated by a range of low temperature scattering events prevalent once phonon scattering becomes negligible. The maximum magnitude of this MR is found at 5 K to

### 5.3 Interfacial Fe doping in the magnetotransport of ultrathin Pt films

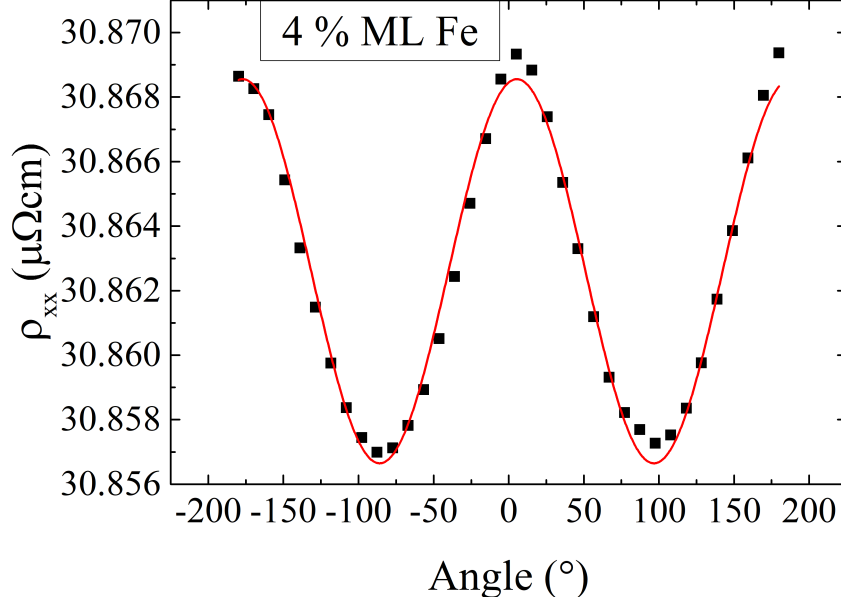


Figure 5.16: Representative angle-dependent data for  $\text{Al-2O}_3/4\% \text{ ML Fe}/2.22 \text{ nm Pt}$  at an applied field of 3 T and a temperature of 2 K in the  $\beta$ -plane. The solid red line describes a cosine squared fit to the data.

be  $(3.4 \pm 0.1) \times 10^{-4}$ , comparable to some SHMR measurements on YIG/Pt bilayers in the literature [110]. The magnitude and temperature dependence of this MR represent a novel form of SHMR which has not previously been observed. The 4% ML Fe forms a thin layer of a dilute PtFe alloy beneath an ultrathin Pt film. This does not exhibit long-range magnetic order, as the impurities are well spaced, and no ferromagnetic signal could be observed via magnetometry measurements. However, the rotation in this plane with an applied magnetic field gives rise to a change in the resistivity that follows a cosine squared dependence on the angle, as in the SHMR [17; 113]. The signal in this sample has a strong dependence on the magnitude of the field applied, in contrast to the SHMR discovered in YIG/Pt bilayers, which is expected to saturate in magnitude for fields larger than the coercive field of the YIG [17]. This effect is hence termed a paramagnetic SHMR (PSHMR). The MPE is expected to play a role, enhancing the apparent size of magnetic impurities by polarising adjacent Pt, as outlined in section 2.7.

### 5.3 Interfacial Fe doping in the magnetotransport of ultrathin Pt films

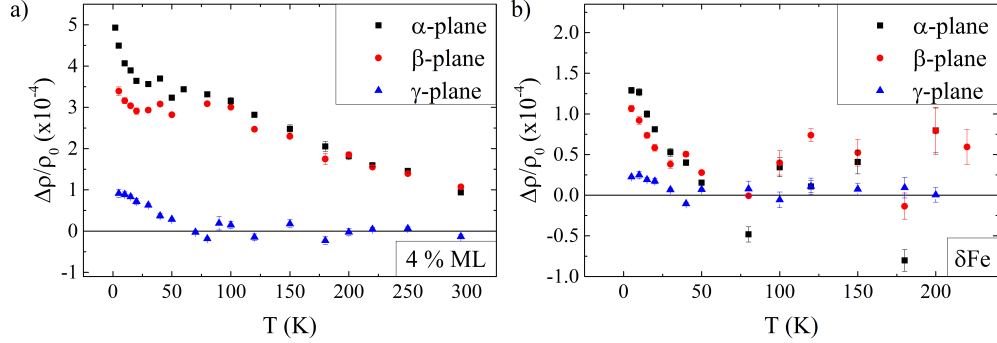


Figure 5.17: The magnitude of the ADMR at an applied field of 3 T as a function of temperature in the  $\alpha$  ( $x$ - $y$ ),  $\beta$  ( $y$ - $z$ ) and  $\gamma$  ( $x$ - $z$ ) planes. The sample structures are a)  $Al_2O_3/4\%$  ML Fe/ $2.22\text{ nm Pt}$  and b)  $Al_2O_3/\delta\text{Fe}/2.28\text{ nm Pt}$ .

The lack of a signal at high temperatures in an AMR geometry is often cited as evidence of a lack of magnetic impurities in a Pt film [23; 58; 112]. This behaviour is observed for Pt interfacially doped with Fe in the  $\gamma$  orientation, with both high and low concentration, as shown in fig. 5.17; therefore a lack of signal at high temperatures is not evidence of a lack of interfacial magnetic impurities. A small signal develops in this orientation below 70 K for 4 % ML Fe and below 30 K for  $\delta\text{Fe}$ , with a concentration dependent magnitude. Its maximum observed value for 4 % ML Fe of  $(9 \pm 1) \times 10^{-5}$  occurs at 5 K; a much smaller value than for the  $\alpha$  and  $\beta$  planes. For  $\delta\text{Fe}$ , the maximum observed magnitude of  $(2.5 \pm 0.4) \times 10^{-5}$  occurs at 10 K, likewise smaller than the other MRs at this temperature. This signal only manifests when phonon scattering is suppressed.

#### 5.3.4 The Hall effect

An anomalous Hall effect is observed in both Pt samples with dilute interfacial impurities. The shape as a function of applied magnetic field is not trivial, and has a strong temperature dependence. A selection of Hall effect data are shown in fig. 5.18 to illustrate this.

In both cases, there exists a non-trivial field dependence up to high fields. The cause of this behaviour, which bears a strong contrast to the ordinary Hall effect ob-

### 5.3 Interfacial Fe doping in the magnetotransport of ultrathin Pt films

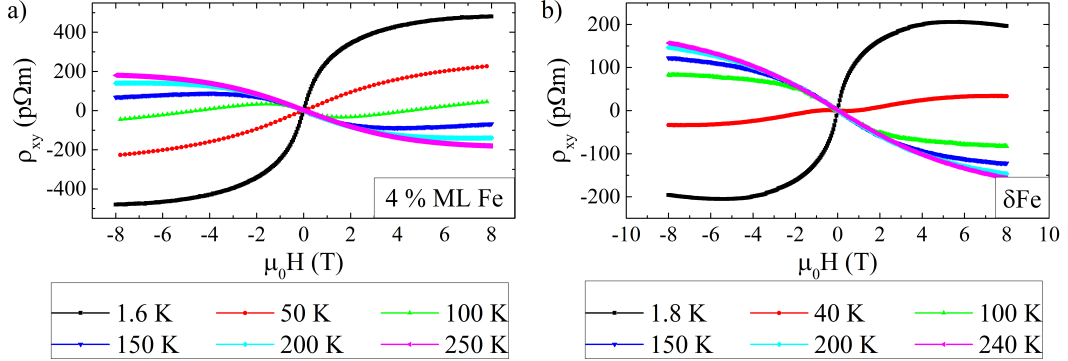


Figure 5.18: The Hall effect observed for ultrathin Pt films doped with an interfacial discontinuous layer of Fe. The samples are a)  $\text{Al}_2\text{O}_3/4\% \text{ ML Fe}/2.22 \text{ nm Pt}$  and b)  $\text{Al}_2\text{O}_3/\delta\text{Fe}/2.28 \text{ nm Pt}$ . The asymmetric component of the raw Hall data is shown.

served in ultrathin Pt in section 5.2.4, is the Fe dopants added at the interface with  $\text{Al}_2\text{O}_3$ . The anomalous Hall effect (AHE) is hence observed in these dilute alloy systems, but lacks the sharp saturation observed in ferromagnets [70]. The form of the Hall effect is notably similar in shape to that for a planar array of Fe nanoparticles [79] and that recently observed in YIG/Pt bilayers [22; 23; 112], as well as for a gated ionic liquid in contact with Pt [86]. The shape is seen to have similarities between the two concentrations displayed in fig. 5.18, yet the magnitude of the Hall resistivity  $\rho_{xy}$  has a strong dependence on the concentration. There are also more subtle differences which are revealed with a more in-depth analysis, discussed in the remainder of this section. The Hall coefficients are extracted from data above 7 T, as this was indicated as a crossover with linear fits to the high and low field Hall effects.

The data in fig. 5.18 look like they might be related to superparamagnetism; the saturation data resemble a Langevin function and at low temperatures, the curves are hysteretic. This would indicate that we are below the blocking temperature. However, the data are not Langevin-like; plots of the data scaled by  $B/T$  are not coincident, as shown in fig. 5.19.

In order to determine whether skew scattering or scattering with side-jump were dominant within these samples, the resistivity scaling of equation 2.27 was employed. The longitudinal resistivity  $\rho_{xx}$ , shown as a function of temperature in fig. 5.20a), was

### 5.3 Interfacial Fe doping in the magnetotransport of ultrathin Pt films

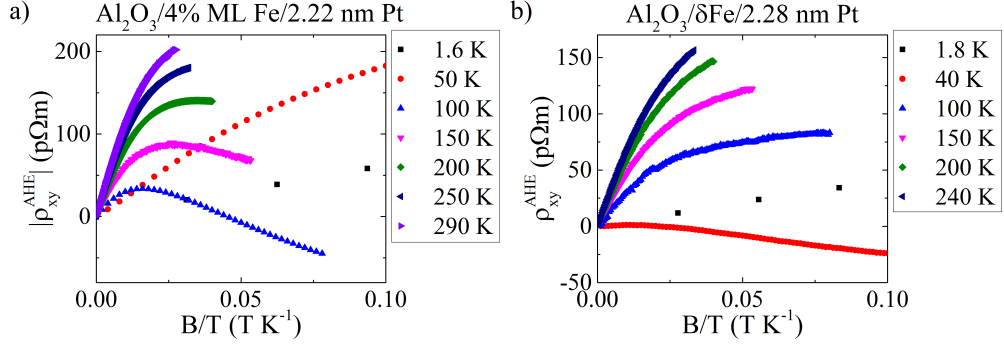


Figure 5.19: The Hall resistivity scaled as a function of the field divided by the temperature for a) 2.22 nm Pt with 4% ML Fe at the interface with  $\text{Al}_2\text{O}_3$  and b) 2.28 nm Pt with  $\delta\text{Fe}$  at the interface with  $\text{Al}_2\text{O}_3$ .

plotted on the  $x$  axis with the anomalous Hall resistivity  $\rho_{xy}^{\text{AHE}} = R_S$ , shown as a function of temperature in fig. 5.20b), was plotted on the  $y$  axis. The result can be viewed in fig. 5.21.

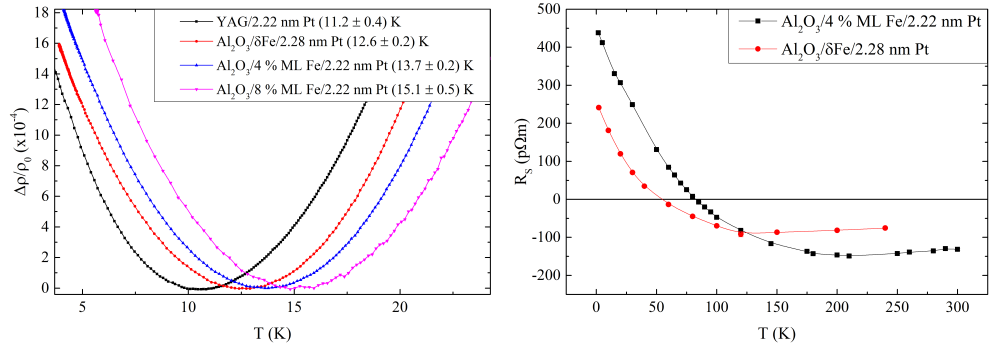


Figure 5.20: On the left, the normalised value of  $\rho_{xx}$  is plotted as a function of temperature at low temperatures, repeated from fig. 5.11. The right shows the value of  $\rho_{xy}^{\text{AHE}} = R_S$  as a function of temperature, as in fig. 5.24.

In fitting fig. 5.21, values below  $T_{\text{min}}$  are neglected. It is found that to produce a fit to the data, an intercept is required such that the fitting equation becomes

$$\rho_{xy}^{\text{AHE}} = \kappa\rho_{xx}^2 + \Phi\rho_{xx} + C \quad (5.2)$$

where  $C$  is a constant  $\rho_{xy}$  value when  $\rho_{xx}$  is extrapolated to zero. This is clearly un-

### 5.3 Interfacial Fe doping in the magnetotransport of ultrathin Pt films

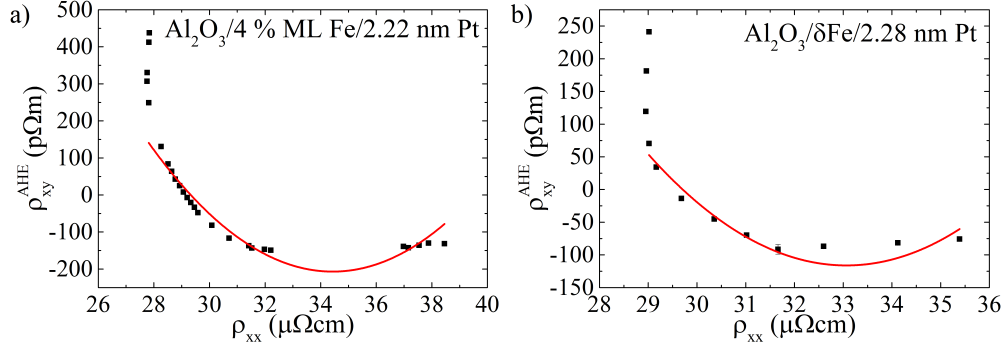


Figure 5.21: The value of  $R_S$ , plotted as  $\rho_{xy}^{\text{AHE}}$ , scaled with the longitudinal resistivity for a) 2.22 nm Pt with 4 % ML Fe at the interface with  $\text{Al}_2\text{O}_3$  and b) 2.28 nm Pt with  $\delta\text{Fe}$  at the interface with  $\text{Al}_3\text{O}_3$ . Red lines show quadratic fits to the data.

physical; without a longitudinal charge resistivity, no anomalous Hall resistivity can exist. The coefficients found from such fits, i.e.  $\kappa$  and  $\Phi$  in equation 5.2, are hence also unphysical and do not correspond to intrinsic, side-jump or skew scattering contributions. It is clear that this method of scaling the anomalous Hall resistivity does not apply to these samples doped with Fe. The table of parameters obtained from the fits of equation 5.2 in fig. 5.21 is shown below, table 5.3.

Table 5.3: The parameters found from scaling the anomalous Hall resistivity with the longitudinal resistivity.  $R_{\text{sq}}$  represents the goodness of fit for equation 5.2.

Substrate	$\Phi$ (mrad)	$\kappa$ ( $\text{MSm}^{-1}$ )	$C$ ( $\mu\Omega\text{cm}$ )	$R_{\text{sq}}$
$\text{Al}_2\text{O}_3/\delta\text{Fe}$	$-(70\pm 10)$	$0.10\pm 0.02$	$1.1\pm 0.2$	0.89826
$\text{Al}_2\text{O}_3/4\% \text{ ML Fe}$	$-(55\pm 4)$	$0.079\pm 0.007$	$0.92\pm 0.07$	0.9486

Both interfacially doped PtFe samples exhibit a low field component to the Hall resistivity which has a different gradient to the rest of the field region at intermediate temperatures. This becomes clearest during the region in temperature over which the anomalous Hall coefficient changes sign. The low field Hall effect over this region is shown in fig. 5.22 for both samples. A few differences are immediately apparent; the gradient of the anomalous region at 30 K is much steeper for the larger concentration; this is shown as changes in the Hall coefficients in figs. 5.23 and 5.24. For the lower

### 5.3 Interfacial Fe doping in the magnetotransport of ultrathin Pt films

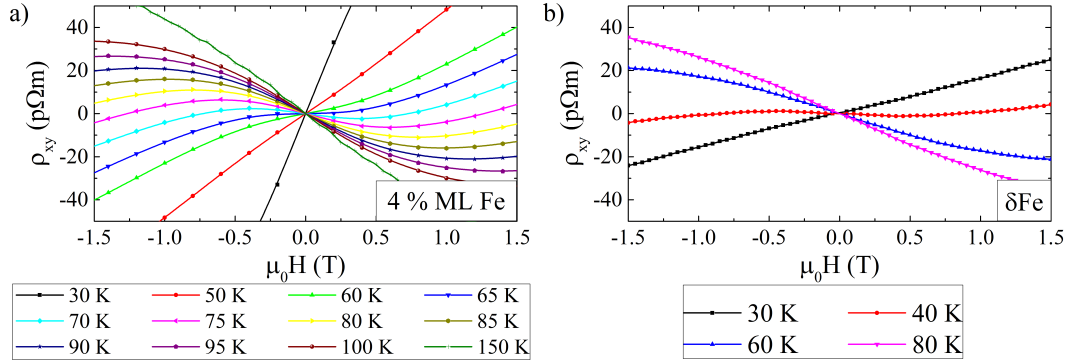


Figure 5.22: The low field Hall effect over the temperature region where the anomalous Hall effect changes sign for Pt interfacially doped with a discontinuous layer of Fe. The samples are a)  $\text{Al}_3\text{O}_3/4\% \text{ ML Fe}/2.22 \text{ nm Pt}$  and b)  $\text{Al}_2\text{O}_3/\delta\text{Fe}/2.28 \text{ nm Pt}$ . The asymmetric component of the raw Hall data is shown. Lines serve as guides to the eye. The same scales are used in both diagrams for ease of comparison.

concentration  $\delta\text{Fe}$ , shown in fig. 5.22b), the central component is most markedly different at 40 K. The change in sign of the anomalous Hall coefficient,  $R_S$ , is seen to first be apparent at high fields, and the low field component maintains a signal of the opposite sign over the transition region; this is not reflected in the value of  $R_S$ , as it is calculated from the high field ordinary Hall component, as outlined in section 3.5.3.

A larger density of data is presented over the region where  $R_S$  changes sign for the sample doped with 4% ML Fe in fig. 5.22a). The temperature region is higher due to the increased concentration of magnetic impurities. For the region where the anomalous Hall component has a dependence upon the field, the gradient of this region is seen to smoothly change from positive at low temperatures, to negative at higher temperatures. It maintains a small component at low field of opposite sign during the transition, as for the lower concentration sample. These data are qualitatively consistent with data in the literature for thicker samples of Pt with a planar array of Fe nanoparticles embedded within them [79]. In this case, a higher concentration was also found to result in a sign change of  $R_S$ , although data for the transition region are not reported here. The sign of the ordinary Hall coefficient,  $R_H$ , is positive at room temperature in these samples, in contrast with both samples considered here. The origin of the central component in this data is not well understood.

### 5.3 Interfacial Fe doping in the magnetotransport of ultrathin Pt films

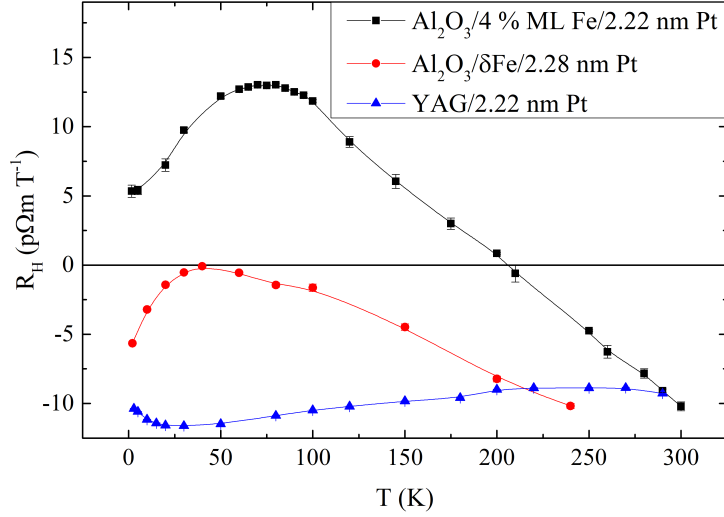


Figure 5.23: *The ordinary Hall coefficient  $R_H$  as a function of temperature for ultrathin Pt films doped with a discontinuous interfacial layer of Fe. Concentrations are shown in the legend. Undoped Pt is shown as a control. Lines serve as guides to the eye.*

The temperature dependence of  $R_H$  for ultrathin Pt films interfacially doped with Fe is shown in fig. 5.23. The magnitude is seen to vary greatly over the temperature range, when compared to that for clean ultrathin Pt on YAG. A positive  $R_H$  manifests below 200 K for Pt with 4 % ML Fe beneath; this behaviour of a positive  $R_H$  value is observed in Pt with a planar array of Fe nanoparticles [79] and also for Fe films [50; 63; 73; 138; 139]. This effect is found only for the highest Fe concentration here studied. For the lower concentration of Fe,  $R_H$  remains negative at all temperatures, with a minimum magnitude of  $-(0.09 \pm 0.09) \text{ p}\Omega\text{m T}^{-1}$  observed at 40 K. To the best of the candidate's knowledge, this is the only time Fe impurities within Pt have been found to give a negative ordinary Hall component throughout the temperature range studied. The transition from a negative to a positive Hall coefficient is interesting and not yet explained. However, with the quality and quantity of data amassed here, we may be able to interest a theoretician in explaining these results.

The temperature dependence of  $R_S$  for ultrathin Pt films interfacially doped with Fe is shown in fig. 5.24. The coefficient is extracted from the raw data by the process described in section 3.5.3. The temperature dependence of this coefficient bears

## 5.4 Thickness dependence of the magnetotransport of Pt thin films with a discontinuous interfacial layer of Fe

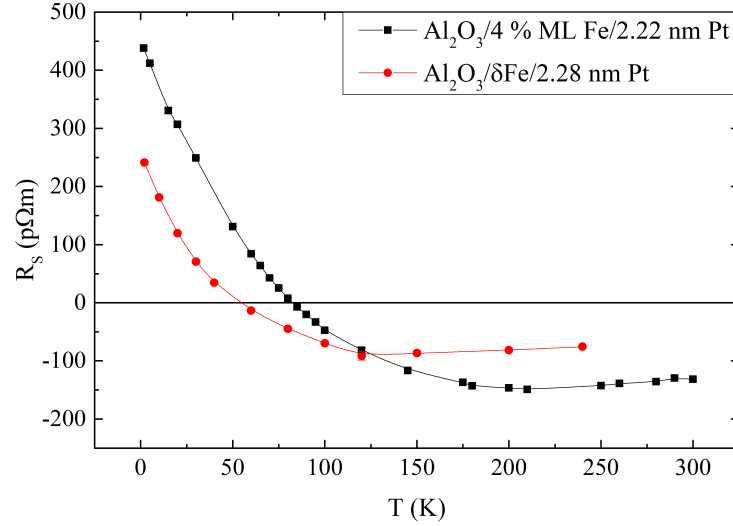


Figure 5.24: The anomalous Hall coefficient  $R_S$  as a function of temperature for ultrathin Pt films doped with a discontinuous interfacial layer of Fe. Lines serve as guides to the eye.

qualitative resemblance to that of  $R_S$  for ultrathin Pt with an ionic liquid [86]. In the cited experiment, various voltages were applied to an ionic liquid in contact with a thin Pt film. This leads to various concentrations of magnetic ions in contact with the Pt film, and varying temperature dependences of  $R_S$  result from the MPE [86]. Larger voltages give rise to a higher temperature for the change in sign of  $R_S$  and a steeper increase in its positive value at low temperatures. This equates with the concentration dependence observed here with impurities localised at the interface. The sign change of the anomalous Hall effect as a function of temperature has been observed recently in other systems, but is not yet explained [75; 192–194].

## 5.4 Thickness dependence of the magnetotransport of Pt thin films with a discontinuous interfacial layer of Fe

When a sample thickness of 5.55 nm Pt is considered with 4 % ML Fe beneath on an  $\text{Al}_2\text{O}_3$  substrate, the Hall effect is seen to have a marked difference in shape. Repre-

sentative data for this Hall effect are shown in fig. 5.25a). The high field Hall effect is much more linear and as expected for the anomalous Hall effect in a sample exhibiting a lower concentration of independent magnetic impurities. This is reflected in the magnitude of the Hall coefficients. The ordinary Hall coefficient, shown in fig. 5.25b), remains negative throughout the temperature range under study, and has a larger amplitude than that of  $(2.22 \pm 0.02)$  nm undoped with Pt. This is due to its greater thickness contributing to a Hall coefficient which is closer to the bulk than for ultrathin Pt. The anomalous Hall coefficient, shown in fig. 5.25c), has the same shape in the temperature dependence, but has a far shallower increase at low temperatures and decrease at high temperatures. This is due to the thicker film; as the impurities are confined at the interface with the substrate, this film exhibits behaviour for a much lower concentration of Fe. It is remarkable that such a minute amount of magnetic impurities confined in such a way is able to produce an anomalous Hall effect. The film is thicker than the typical spin diffusion length for polycrystalline Pt films of 1.2-1.6 nm [186].

To complete this study of the anomalous Hall effect in thin films with interfacial impurities, further work should be completed. The low field Hall effect, during the change in sign of the anomalous Hall effect, can not be seen to exhibit regions of different sign in fig. 5.25a) due to the chosen resolution of the experiment. A higher resolution in field and a wider temperature range would further elucidate the mechanisms at work in this sample. A detailed study over a range of thicknesses would also enable the effect of interfacial impurities on this Hall effect to be studied. As these measurements are quite lengthy, this proved out of the scope of this PhD project.

## 5.5 Summary

It has been demonstrated that quantum interference effects make a substantial contribution to the angle-dependent magnetoresistance, indicating that in 2D samples, such as those used in measurements of the SHMR in YIG/Pt bilayers, this effect should be taken into account. A discontinuous  $\delta$ -layer of Fe placed within an ultrathin Pt film, localised at the interface with an  $\text{Al}_2\text{O}_3$  substrate, is found to have a dramatic impact upon its magnetotransport. A large negative MR is found to develop in the

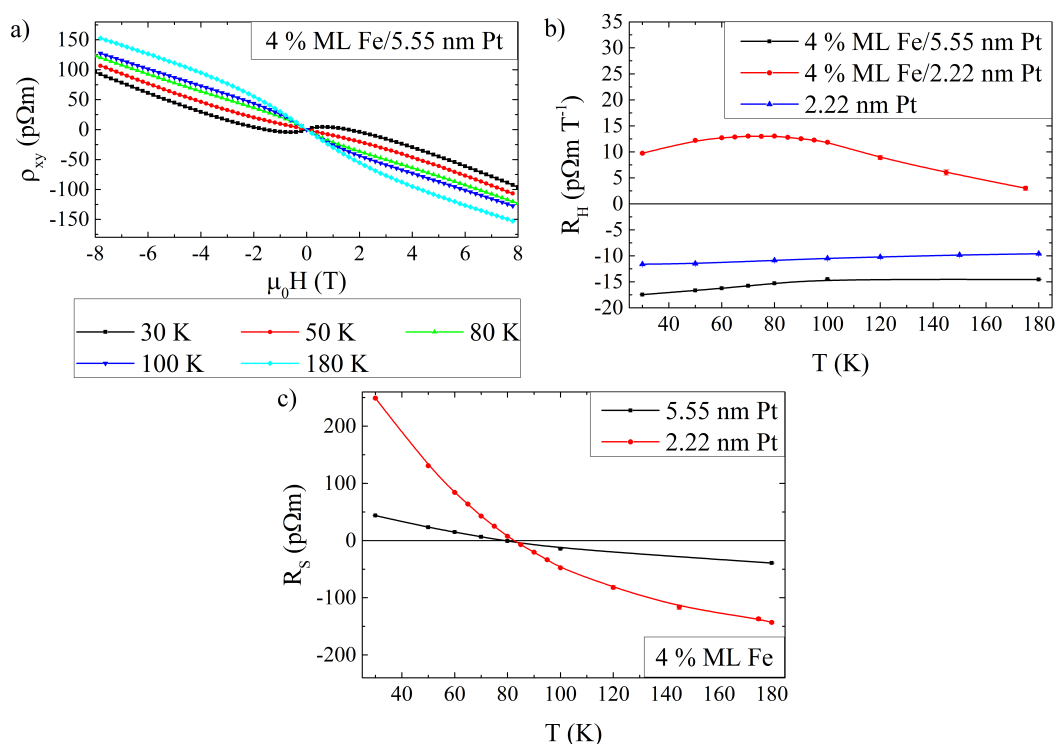


Figure 5.25: The Hall data for 5.55 nm Pt with 4 % ML Fe beneath on an  $Al_2O_3$  substrate: a) shows the Hall resistivity as a function of field at select temperatures, b) shows the ordinary Hall coefficient,  $R_H$  and c) shows the anomalous Hall coefficient,  $R_S$ , both as a function of temperature for both 5.55 nm (black squares) and  $(2.22 \pm 0.02)$  nm (red circles) Pt with 4 % ML Fe beneath. b) also shows  $R_H$  for  $(2.22 \pm 0.02)$  nm Pt without Fe impurities. Lines are to guide the eye.

perpendicular orientation where weak anti-localisation is destroyed by the presence of magnetic impurities, and weak localisation becomes dominant. The magnitude of this MR is dependent upon the concentration of impurities added. A small AMR is found below 50 K, with a magnitude dependent upon the concentration. A paramagnetic spin Hall magnetoresistance (PSHMR) is found to manifest with a strong temperature dependence distinct from that of the conventional SHMR. In a system with reduced concentration, this PSHMR is considerably reduced.

It is found that a concentration of less than 4 % ML Fe at the substrate is sufficient to cause the anomalous Hall effect to manifest within Pt, with a higher concentration

of 4 % ML causing a change in sign of the ordinary Hall coefficient below 200 K. For a larger film thickness of 5 nm, the anomalous Hall effect persists with only 4 % ML Fe placed at the substrate.  $R_S$  exhibits behaviour in all cases as a function of temperature and concentration qualitatively similar to that for a Pt system with MPE [86]. The Hall effect data are not Langevin-like, however, and resistivity scaling of the AHE show that there is a strong side-jump contribution.

---

# CHAPTER 6

---

Interfacial dependence of  
magnetotransport in YIG/Pt bilayers

## 6.1 Introduction

With the recent discovery of the spin Hall magnetoresistance (SHMR) [17; 113], bilayers of magnetic insulators and normal metals with high spin-orbit coupling have attracted much research interest. The magnetic proximity effect at the interface in YIG/Pt bilayers has been investigated in the literature, with varying results [20–23]. Here, the YIG/Pt interface is prepared in four different ways, allowing for an investigation of the impact of interface preparation on the magnetic proximity effect.

## 6.2 Characterisation of YIG

The magnetic insulator yttrium iron garnet ( $\text{Y}_3\text{Fe}_5\text{O}_{12}$ , YIG) is grown to high quality at the University of Leeds, due to the optimising work of other group members in recent years [110; 161; 195; 196]. Two substrates are used throughout this study: gadolinium gallium garnet ( $\text{Gd}_3\text{Ga}_5\text{O}_{12}$ , GGG) and yttrium aluminium garnet ( $\text{Y}_3\text{Al}_5\text{O}_{12}$ , YAG). Both substrates have a similar lattice parameter to YIG, aiding in the formation of epitaxial films. A magnetic 'dead layer' was found to exist upon annealing YIG films grown on GGG substrates [165; 196], leading to the use of YAG substrates in this study. This represents the first time this substrate was used in the group for the growth of YIG by rf magnetron sputtering, and hence a brief study of the characteristics of films grown on both YAG and GGG is presented here, in addition to analysis at the various stages of interface preparation.

### 6.2.1 Magnetometry

Vibrating sample magnetometry is used to probe the magnetic properties of the YIG films in the plane of the sample, as outlined in section 3.4. A comparison of data for annealed YIG films on both GGG and YAG is shown in fig. 6.1.

The three YIG samples shown in fig. 6.1 were grown simultaneously, then two were annealed together in a furnace to a final thickness of  $(40.8 \pm 0.8)$  nm. Two

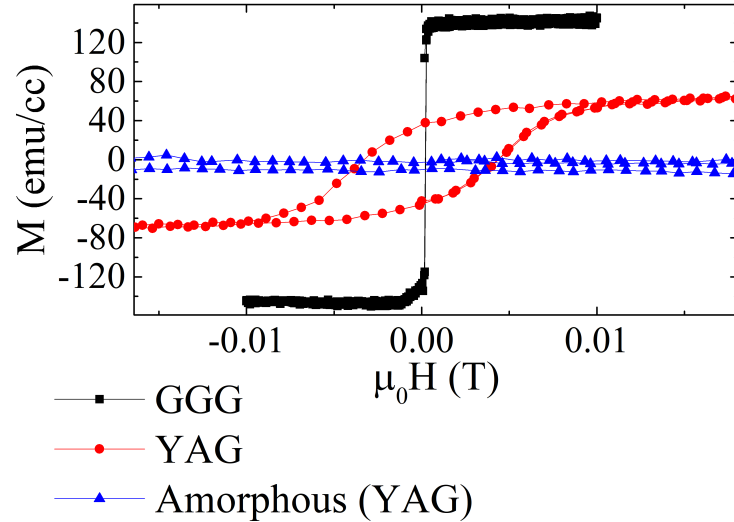


Figure 6.1: Magnetometry data for  $(40.8 \pm 0.8)$  nm of YIG grown by rf magnetron sputtering on both GGG (black squares) and YAG (red circles, blue triangles) substrates simultaneously. Two samples were annealed together in a furnace, as outlined in 3.2.2.2, whilst the third was left amorphous. VSM measurements are taken in the plane of the sample at a temperature of 295 K.

samples on YAG and two on GGG were grown at the same time, and results for the same substrate are consistent. The magnetometry work was performed in the plane of the sample at 295 K, and it was found that both directions yielded consistent results, suggesting a magnetically isotropic film. There are striking differences in the magnetometry data between the two substrates, however. The saturation magnetisation,  $M_S$ , is found to be much smaller for the YAG substrate than GGG. On GGG,  $M_S$  is found to be  $(140 \pm 10)$  emu/cc, which is comparable to findings for bulk YIG films and consistent with previous films from the department [110; 161; 196]. On a YAG substrate, the  $M_S$  is found to be  $(77 \pm 8)$  emu/cc; almost half that for GGG. The coercive field,  $H_c$ , also is markedly different for the two different substrates; on GGG it has a value of  $(0.5 \pm 0.1)$  Oe, whilst on YAG this rises to  $(370 \pm 50)$  Oe; an increase of almost two orders of magnitude. It can be seen that the sample which wasn't annealed lacks a net magnetisation.

The stark contrast in the magnetometry data is attributed to different lattice parameters of the substrates. GGG and YAG have lattice parameters of  $12.383 \text{ \AA}$  and  $12.000$

Å, respectively, whilst YIG has a lattice parameter of 12.376 Å [167; 197; 198]. The substrate offering the closest match is hence GGG, and this explains why the magnetic properties are more in line with that of bulk YIG than for YAG substrates. It has previously been found that a larger lattice mismatch leads to strain on epitaxially grown YIG, which can induce an anisotropy and strongly affect the magnetic properties of the YIG [199]. Another possible cause of the decrease in the value of  $M_S$  is the diffusion of non-magnetic Al or Y from the substrate, consistent with recently observed results at the YAG/YIG interface [168].

It is important to note that a linear paramagnetic background signal has been removed from the data for GGG shown in fig. 6.1, due to the strong paramagnetism observed in GGG. No paramagnetic signal is observed on YAG, making this a preferred choice for low temperature magnetometry measurements, where background signals become harder to extract. As YAG possesses no conventionally magnetic elements, the formation of a magnetic dead layer from the migration of these elements is avoided, giving opportunity to study its potential effects in contrast to GGG. Despite possessing less desirable magnetic properties for applications, YIG films grown on YAG hence still hold considerable interest for the scientific community.

Much of this chapter focuses on magnetotransport for YIG during various stages of preparation, so the magnetic properties at these stages is worth noting. Directly after deposition and prior to annealing, the YIG films are amorphous and exhibit no ferrimagnetic signal in magnetometry measurements; on GGG, the paramagnetic background signal is apparent, but on YAG no signal is observable above the noise level of the system. This is shown in blue on fig. 6.1 alongside the data after the annealing process. After etching, and taking the difference in thickness into account, no statistically significant change is seen in either the  $M_S$  or  $H_c$  value.

### 6.2.2 X-ray diffraction

The YIG crystal structure is probed via the use of x-ray diffraction at  $2\theta$  values greater than  $20^\circ$ . Fig. 6.2 shows representative high angle x-ray diffraction data for YIG which

has been annealed on a YAG substrate.

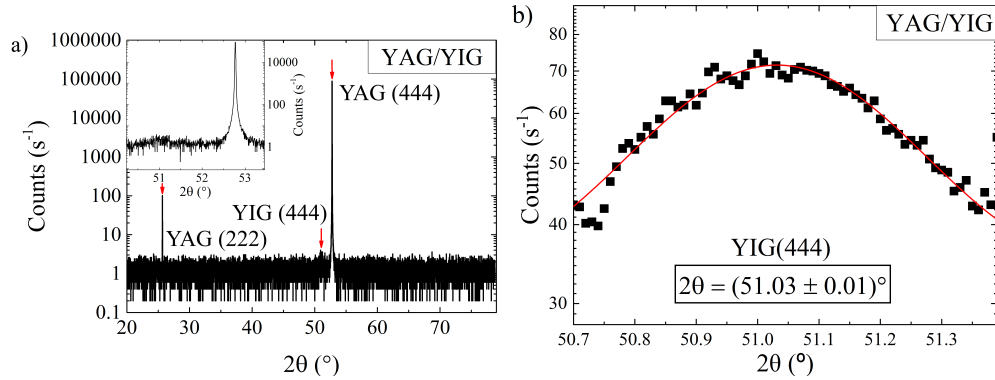


Figure 6.2: a) High angle x-ray diffraction data are shown for annealed YIG on a YAG substrate; the main figure shows the full  $2\theta$  range considered, whilst the inset shows the YIG(444) and YAG(444) peaks. Following realignment to the YIG(444) peak, the Gaussian fit of this peak is shown in b).

The peak for the YIG(444) crystal plane is found to be centred at  $(51.03 \pm 0.01)^\circ$ , which corresponds to a lattice parameter of  $(12.36 \pm 0.01) \text{ \AA}$  for the (444) plane, consistent with expectation for YIG [167], via the method outlined in section 3.3.2. The low intensity is due to the thin nature of the film; recently, larger peaks have been observed for YIG grown in the group which is of thickness 200 nm [200]. Two YAG peaks are observed in the spectrum in fig. 6.2, centred at  $(25.7 \pm 0.1)^\circ$  and  $(52.8 \pm 0.1)^\circ$ , corresponding to lattice parameters of  $(12.0 \pm 0.1) \text{ \AA}$  for the (222) plane and  $(12.0 \pm 0.1) \text{ \AA}$  for the (444) plane, respectively, consistent with expectation for YAG [197]. For YIG films grown on GGG, the peak positions in the x-ray diffraction spectrum are much closer together and difficult to distinguish without higher intensity scattering from a thicker film. Thicker films of YIG grown on GGG within the group have proven to be of very high quality with an interplanar spacing that indicates low strain in the YIG layer [110; 161; 165]. The YIG grown on YAG is of lower quality, having a lower magnetisation and low intensity XRD peak. The impact of this on the study is small; providing the layer possesses a magnetisation, its magnitude has no impact on the SHMR. Interfacial effects under investigation do not depend upon the bulk magnetic properties of the YIG, but it is left to future work to determine if any change in inter-

facial effects could be determined depending on the termination at the surface.

## 6.3 Resistivity and its temperature dependence in YIG/metal bilayers

The resistivity of metallic samples has long been used as a measure of their purity and quality. The resistivity of thin films is particularly sensitive, susceptible to large increases if interfaces are rough, their structure is disordered or if impurities exist within the films, among other factors. When considering the change in resistivity as a function of temperature, further information regarding the film structure can be gained. In this section, the effect of the YIG preparation method on the resistivity and its temperature dependence will be explored. Fig. 6.3 shows the normalised resistivity at low temperatures for YIG/Pt bilayers with various interfaces.

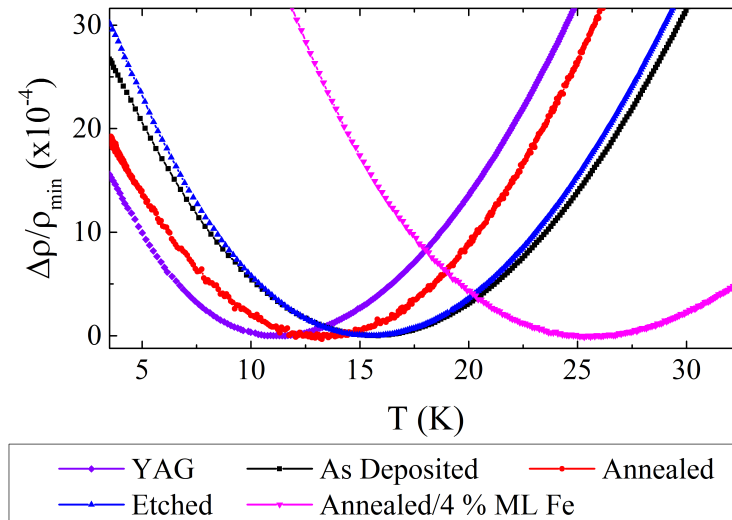


Figure 6.3: The normalised longitudinal resistivity at low temperatures for ultrathin Pt in YIG/Pt bilayers with different interfaces. Lines are shown as guides to the eye. The interface structure for each film is displayed in the legend, and each film consists of  $(2.22 \pm 0.02)$  nm Pt on the top surface. YAG represents the control sample without YIG.

### 6.3 Resistivity and its temperature dependence in YIG/metal bilayers

In fig. 6.3, the normalised resistivity data are calculated as in eqn. 5.1, and data for  $(2.22 \pm 0.02)$  nm Pt on a YAG substrate is represented by purple diamonds, as already shown in fig. 5.1b). This is a control sample fabricated in the same growth cycle as the other samples on a YAG substrate. The as deposited, annealed and etched samples of YIG are all on a YAG substrate, whereas the sample with 4 % ML Fe between the YIG and Pt is deposited on GGG in a separate growth run. The absolute resistivities lie in the range  $30\text{-}36 \mu\Omega\text{cm}$ , for all but the etched film which has a resistivity of  $53 \mu\Omega\text{cm}$ . This large increase is thought to be due to the film surface becoming exceedingly rough; previous work has shown high, thin peaks form on the surface after etching when probed with atomic force microscopy (AFM) [161]. In the case of the other films, the highest value found was for Pt on amorphous YIG, consistent with the higher  $T_{\min}$  found in fig. 6.3 for this film. The lowest resistivity was found for clean Pt on YAG, as expected, of  $30 \mu\Omega\text{cm}$ .

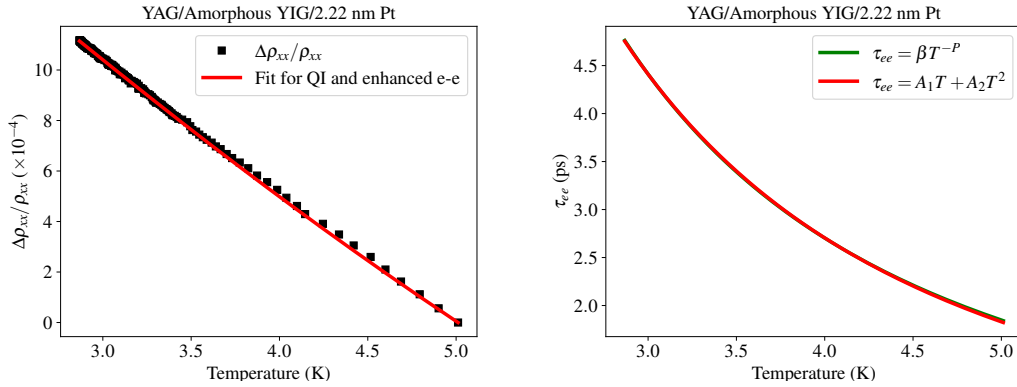


Figure 6.4: For YAG/Amorphous YIG/2.22 nm Pt, a fit of a) the quantum interference and enhanced electron-electron interaction to the resistivity, as per equations 2.34 and 2.38, and b) the resulting power law for the electron-electron interaction as per equation 2.37.

The YIG samples have varying thicknesses dependent upon the stage of preparation the surface is left at: as deposited YIG has thickness of  $(36.6 \pm 0.6)$  nm; annealed YIG of  $(34 \pm 2)$  nm and etched YIG of  $(32 \pm 1)$  nm. The thickness are found from x-ray reflectivity data, as outlined in section 3.3.1. This data is shown in an appendix with associated fits. The Pt thickness is consistent throughout the samples, found by x-ray reflectivity from control samples of around 40 nm thickness within the

### 6.3 Resistivity and its temperature dependence in YIG/metal bilayers

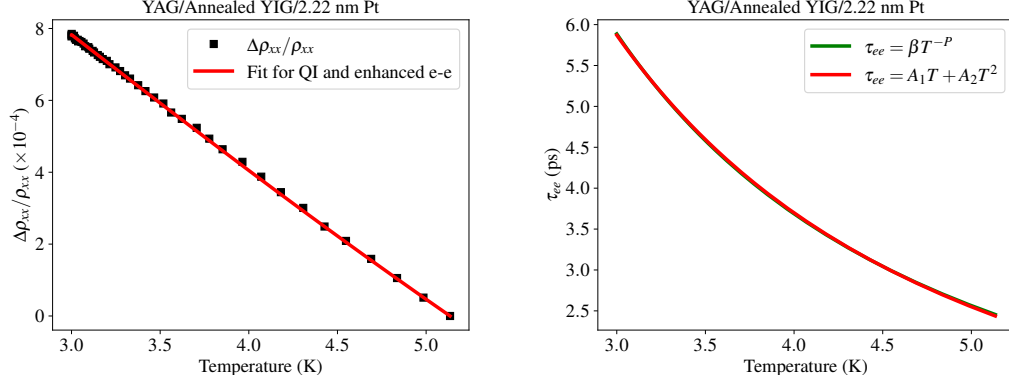


Figure 6.5: For YAG/Annealed YIG/2.22 nm Pt, a fit of a) the quantum interference and enhanced electron-electron interaction to the resistivity, as per equations 2.34 and 2.38, and b) the resulting power law for the electron-electron interaction as per equation 2.37.

growth. The position of the resistivity minima shows variation between samples consistent with varying concentrations of magnetic ions at the interface. It was recently posited that engineering the crystal structure of the YIG at an interface with metals could strongly affect the magnetotransport properties of the system [201]. Due to the growth method utilised in this study, the lattice termination cannot be engineered in such a way to complement this mathematical study; however, this would be possible with liquid phase epitaxy, pulsed laser deposition or molecular beam epitaxy with *in-situ* reflection high-energy electron diffraction: an area for future research. The method employed of using amorphous (as deposited), ordered (annealed) and etched YIG does allow for a study of how these processes affect the concentration of magnetic ions at the termination of the film. Based on the work of chapter 5, the effect of varying concentrations of Fe impurities has been studied and here allows for interpretation of the magnetotransport data where the concentration of magnetic ions is unknown. The systems are not entirely equivalent, but the physics of a localised dilute concentration of magnetic impurities at the surface of a thin film is poorly understood. The systems are sufficiently similar to shed light on some of the unexplained phenomena occurring in YIG/Pt bilayers.

Fits to the resistivity data and resulting  $\tau_{ee}$  power law are shown in figs. 6.4, 6.5 and 6.6 for the amorphous, annealed and etched samples of YIG, respectively. The

### 6.3 Resistivity and its temperature dependence in YIG/metal bilayers

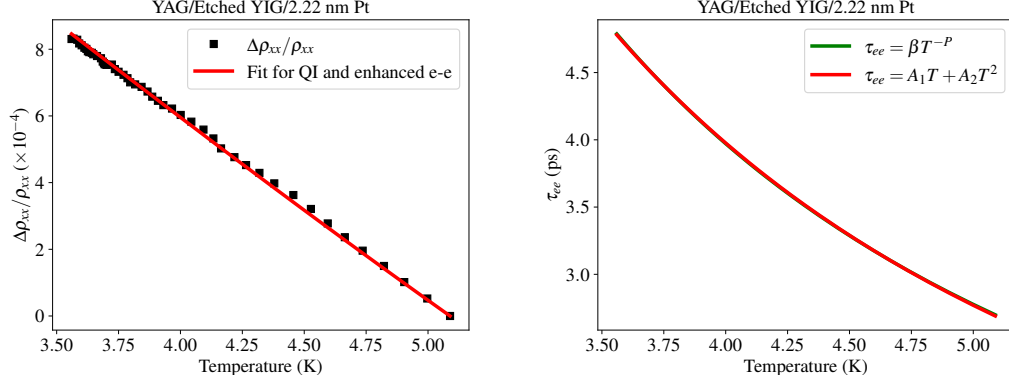


Figure 6.6: For YAG/Etched YIG/2.22 nm Pt, a fit of a) the quantum interference and enhanced electron-electron interaction to the resistivity, as per equations 2.34 and 2.38, and b) the resulting power law for the electron-electron interaction as per equation 2.37.

parameters found from fits of both weak localisation and enhanced electron-electron interaction to the resistivity data are shown in table 6.3, alongside the results from chapter 5. Values of  $P$  are consistent with those in the literature for similar systems [202]. Variations between samples are small and give us confidence that these fits are meaningful. Fitting the temperature dependence of  $\tau_{ee}$  to the Fermi liquid equation confirms the values of  $P$  are consistent with 2D behaviour. The values of  $F$  are also consistent with the literature and our expectations - the enhanced electron-electron interaction has reduced the Thomas-Fermi screening factor. As mentioned, the spin-orbit lengthscale, which is equivalent to the spin diffusion length for this type of scattering [202], depends on the elastic diffusion constant which is not well known; hence, our best estimate is an order of magnitude too large. The elastic mean free path  $\lambda$  shows that the samples are in the limit of being two dimensional. The point remains that the spin-orbit lifetime is an order of magnitude too large compared to other measurements. However, it should be noted that these effects have not been calculated together; they are usually calculated independently and then added as though they were independent. For example, we are not aware of a 2-D calculation for the effects of strong spin-orbit scattering on the electron-electron interaction. Also, there is no account taken of magnetic impurity scattering in the temperature dependence. It is equally important that the correct expressions are used; recently a publication was found to use a 1D expression to analyse data from a 3D sample [202]. It is not clear what effect using the correct

### 6.3 Resistivity and its temperature dependence in YIG/metal bilayers

Table 6.1: Parameters for the fits of quantum interference and the enhanced electron-electron interaction in figs. 5.2, 5.12, 6.4, 6.5 and 6.6.

Sample	$\tau_{\text{so}}$ (ps)	$\rho_{xx}$ ( $\mu\Omega\text{cm}$ )	$F$	$L_{\text{so}}$ (nm)	$\lambda$ (nm)
YAG/2.22 nm Pt	6 $\pm$ 4	30 $\pm$ 3	0.36 $\pm$ 0.01	30 $\pm$ 3	11 $\pm$ 1
Amorphous YIG/2.22 nm Pt	7 $\pm$ 1	36 $\pm$ 3	0.295 $\pm$ 0.005	31 $\pm$ 3	11 $\pm$ 1
Annealed YIG/2.22 nm Pt	7 $\pm$ 3	33 $\pm$ 3	0.343 $\pm$ 0.005	32 $\pm$ 3	12 $\pm$ 1
Al <sub>2</sub> O <sub>3</sub> / $\delta$ Fe/2.28 nm Pt	7 $\pm$ 3	30 $\pm$ 3	0.318 $\pm$ 0.005	34 $\pm$ 3	14 $\pm$ 1
Etched YIG/2.22 nm Pt	6 $\pm$ 3	53 $\pm$ 3	0.35 $\pm$ 0.01	24 $\pm$ 3	8 $\pm$ 1
Al <sub>2</sub> O <sub>3</sub> /4 % ML Fe/2.22 nm Pt	7 $\pm$ 2	30 $\pm$ 3	0.332 $\pm$ 0.005	33 $\pm$ 3	13 $\pm$ 1

Sample	$\beta$ ( $\times 10^{-10}$ )	$P$	$A_1$ ( $\times 10^{10}$ s/K)	$A_2$ ( $\times 10^{10}$ s/K <sup>2</sup> )
YAG/2.22 nm Pt	0.38 $\pm$ 0.09	1.59 $\pm$ 0.05	2.470 $\pm$ 0.008	0.874 $\pm$ 0.002
Amorphous YIG/2.22 nm Pt	0.29 $\pm$ 0.03	1.70 $\pm$ 0.05	2.500 $\pm$ 0.009	1.690 $\pm$ 0.003
Annealed YIG/2.22 nm Pt	0.35 $\pm$ 0.06	1.63 $\pm$ 0.05	2.43 $\pm$ 0.02	1.080 $\pm$ 0.005
Etched YIG/2.22 nm Pt	0.36 $\pm$ 0.09	1.60 $\pm$ 0.05	2.55 $\pm$ 0.01	0.934 $\pm$ 0.003
Al <sub>2</sub> O <sub>3</sub> / $\delta$ Fe/2.28 nm Pt	0.32 $\pm$ 0.06	1.65 $\pm$ 0.05	2.58 $\pm$ 0.01	1.320 $\pm$ 0.004
Al <sub>2</sub> O <sub>3</sub> /4 % ML Fe/2.22 nm Pt	0.34 $\pm$ 0.04	1.63 $\pm$ 0.05	2.32 $\pm$ 0.01	1.200 $\pm$ 0.003

expression might have on the parameters returned.

The temperature at which the resistivity minimum occurs,  $T_{\text{min}}$ , varies by a significant amount depending on the YIG surface. As stated in section 5.2.1, the minimum in the YAG/Pt sample occurs at  $(11.2 \pm 0.4)$  K and is due to quantum interference and the enhanced electron-electron interaction, as the source material has been shown to be free of significant amounts of magnetic impurities. The addition of magnetic impurities localised at the interface of the substrate was found to increase  $T_{\text{min}}$  to  $(13.7 \pm 0.2)$  K for 4 % ML Fe in section 5.3.1. Here, it is found that, for  $(2.22 \pm 0.02)$  nm Pt deposited on amorphous YIG,  $T_{\text{min}}$  increases to  $(15.6 \pm 0.2)$  K, suggesting a large concentration of magnetic ions are present at the YIG/Pt interface. For an annealed sample, this value decreases to  $(13.4 \pm 0.5)$  K and for an etched sample rises to  $(15.6 \pm 0.2)$  K. The amorphous and etched samples hence have the same  $T_{\text{min}}$  value and therefore ostensibly the same concentration of magnetic ions on the YIG surface. The annealed sample, however, with a lower  $T_{\text{min}}$ , appears to have a lower concentration of magnetic ions, but still more than in the non-magnetic control sample. This trend follows from that seen for deliberate interfacial doping of Fe within Pt in chapter 5. In order to

### 6.3 Resistivity and its temperature dependence in YIG/metal bilayers

investigate whether magnetic ions are static on the YIG surface, or alloying with the metallic layer, Cu is used in the following section.

#### 6.3.1 Resistivity of YIG/Cu bilayers

Cu with dilute amounts of Fe impurities is a system known to exhibit the Kondo effect and be particularly sensitive to very low concentrations of magnetic impurities [98; 151]. For impurities localised at the interface, a thicker film results in a lower concentration of impurities. To determine whether Kondo scattering is present from magnetic impurities at the YIG surface, thin films of Cu were grown on annealed samples of YIG. Cu is much farther from satisfying the Stoner criterion than Pt and as such experiences a magnetic proximity effect of negligible magnitude. This allows for the separation of the magnetic proximity effect from the results and allows one to determine whether intermixing at the YIG/metal interface contributes to the observed resistivity minimum phenomenon.

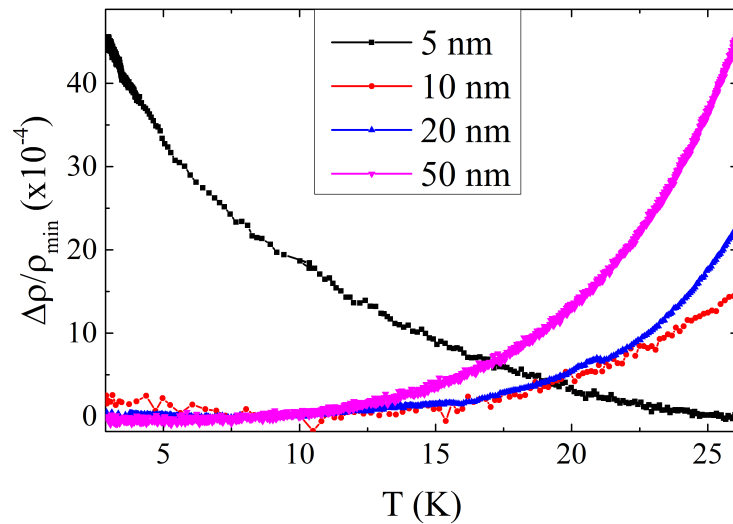


Figure 6.7: Resistivity data, normalised to the minimum resistivity observed, is shown at low temperatures for various thickness of 99.9999% pure Cu deposited on annealed YIG atop a GGG substrate.

### 6.3 Resistivity and its temperature dependence in YIG/metal bilayers

---

Fig. 6.7 shows the normalised resistivity at low temperatures of various thicknesses of Cu deposited on YIG. The normalising in equation 5.1 has been applied to display the data. The YIG is deposited on a GGG substrate and has undergone the annealing and etching processes. The Cu target chosen for this study has 99.9999% purity to enable detection of the minute concentrations of impurities which may be present at larger film thicknesses for a sparse coverage of magnetic impurities at the interface. A Cu film thickness of 20 nm was used in chapter 4 and no resistivity minimum above 4 K was observed in these systems. As such, 20 nm Cu is thought, like 20 nm Pt, to not exhibit weak localisation phenomena; as such, resistivity minima for this thickness are caused by Kondo scattering from magnetic impurities [151].

Resistivity minima are observed for thickness of up to 20 nm Cu on YIG; at 50 nm, no minimum is observed and the temperature dependence of the resistivity is metallic. For 5 nm Cu,  $T_{\min}$  occurs at  $(28 \pm 2)$  K. For double this thickness, the value changes to  $(10 \pm 2)$  K, then upon doubling again moves to  $(8 \pm 2)$  K. These correspond to concentrations of  $(0.002 \pm 0.001)$  at.% and  $(0.0007 \pm 0.0002)$  at.% at thicknesses of 10 nm and 20 nm Cu, respectively, using the empirical relation found in [151] and neglecting weak localisation. These exceptionally small concentrations are consistent with the presence of interfacial impurities. For 7.5 nm Cu, a  $T_{\min}$  value of 15 K has been found [130], indicating that the higher value observed here is due to magnetic impurities. Further magnetoresistance data would be needed to fully separate weak localisation from the Kondo effect in this system, as their temperature dependences are proportional; this is left to future work [122; 146].

This brief study serves to demonstrate that magnetic impurities cause Kondo scattering in thin films of Cu deposited on YIG. This means intermixing is present at the interface between a metal and YIG, independent of any magnetic proximity effects. The intermixing is known to be of the lengthscale of less than 2 ML from cross-sectional transmission electron microscopy (TEM) work performed on similar samples [110; 161]; the resolution of the technique is insufficient to rule out intermixing below this length scale.

### 6.4 Angle-dependent magnetoresistance in YIG/Pt bilayers

The SHMR is a recently discovered phenomenon which is simply measured by rotating a YIG/metal bilayer in a constant applied magnetic field in the  $\beta$ -plane [17]. In this section, the ADMR of YIG/Pt samples with various interfaces is reported, with a study on the field-dependence of the SHMR.

#### 6.4.1 Field dependence of the spin Hall magnetoresistance

The SHMR is a phenomenon which is independent of the magnitude of the applied field above the saturation field of the insulating magnetic layer [17; 113]. The field dependence of the signal measured in the  $\beta$ -plane ( $y$ - $z$  plane) is investigated at 100 K in order to determine if an additional PSHMR exists for any of the interfaces under study, shown in fig.6.8.

A strong field dependence is observed for the ADMR in the  $\beta$ -orientation which is not expected from the theory of the conventional SHMR [17; 113]. For a substrate of amorphous YIG, the conventional SHMR signal is expected to be small as the moments are randomly aligned. This SHMR will only saturate at very high fields, which depend upon the anisotropy of the amorphous YIG, as this is when the magnetisation is fully rotated out of the plane of the sample [203]. The signal measured in this sample is hence interpreted as a combination of SHMR and PSHMR signals, as discussed in chapter 5, resulting from disordered Fe sites at the YIG surface. The strong field dependence observed in fig. 6.8a) is therefore expected as more of these isolated sites, both within the YIG and on its surface, are aligned with the field. The magnitude of the PSHMR is found to be  $(1.38 \pm 0.04) \times 10^{-4}$  at an applied field of 3 T and  $(0.28 \pm 0.04) \times 10^{-4}$  at an applied field of 1 T. The lower field magnitude is chosen to be sufficiently high to saturate an annealed YIG sample out of the plane. This large value shows that the PSHMR is capable of surpassing the SHMR in magnitude.

## 6.4 Angle-dependent magnetoresistance in YIG/Pt bilayers

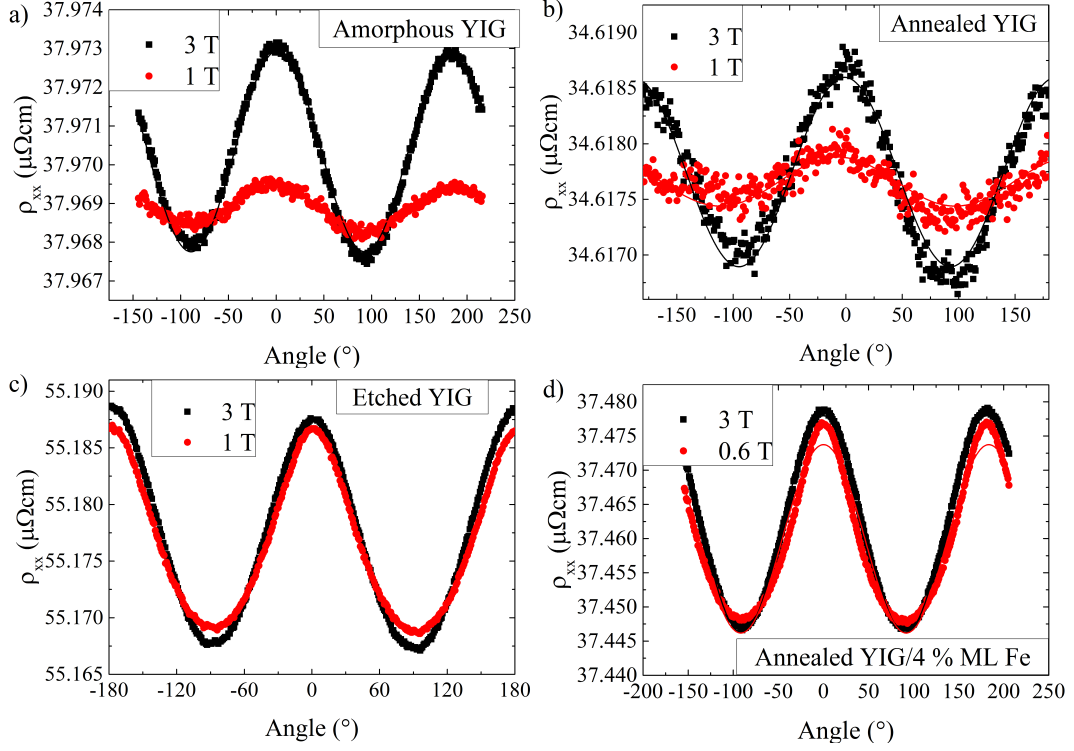


Figure 6.8: The field dependence of the magnetoresistance in the  $\beta$ -plane at 100 K for 2.22 nm Pt on a) amorphous YIG, b) annealed YIG, c) etched YIG and d) 2.28 nm Pt on annealed YIG with 4 % ML Fe on top. The solid lines show cosine squared fits to the data. Samples a)-c) have a YAG substrate, while sample d) is grown on GGG. The fields are chosen to be above the expected saturation field of the YIG out of the sample plane.

Once the YIG has been annealed, the conventional SHMR mechanism is expected to be prevalent, as the YIG structure is now ordered. This is expected to saturate at the saturation field of the YIG and remain constant for larger applied fields. A significant difference is still observed between the two applied fields in fig. 6.8b), with magnitudes of  $(0.49 \pm 0.03) \times 10^{-4}$  and  $(0.14 \pm 0.02) \times 10^{-4}$  at applied field of 3 T and 1 T, respectively. Both magnitudes are significantly smaller than for the amorphous YIG sample; this indicates that the PSHMR has reduced in magnitude as the SHMR has manifested. This is in part demonstrated by the reduced  $T_{\min}$  observed in section 6.3 and is demonstrated by other magnetotransport phenomena, explored later in this chapter. A PSHMR is still present, however, as the magnitude of the ADMR remains strongly dependent upon the magnitude of the applied magnetic field above the satura-

## 6.4 Angle-dependent magnetoresistance in YIG/Pt bilayers

---

tion field of the YIG layer.

Upon etching, a large SHMR signal is found to manifest at 1 T, with a large PSHMR also found. The magnitude at 1 T is found to be  $(3.22 \pm 0.04) \times 10^{-4}$ , which increases to  $(3.69 \pm 0.07) \times 10^{-4}$  at an applied field of 3 T; the PSHMR in this field range is hence significantly less than that observed for amorphous YIG, but larger than for annealed YIG. The resistivity has increased significantly to around  $55 \mu\Omega\text{cm}$  compared to the  $34\text{-}38 \mu\Omega\text{cm}$  found for the other interfaces with YIG. This reinforces the result of increased roughness found from x-ray reflectivity as the most likely cause of the increase. The large increase in the SHMR signal by an order of magnitude indicates an improved spin mixing conductance in this sample, which is also evidenced by the Hall effect found in section 6.6.1. An enhancement of the PSHMR is also found in this sample, however, in comparison the YIG which has been annealed.

For the sample shown in fig. 6.8d), where the interface is doped with 4 % ML Fe, the field dependence of the SHMR signal is less remarkable when considered as a percentage change. The magnitudes of the ADMR are  $(8.5 \pm 0.1) \times 10^{-4}$  and  $(7.7 \pm 0.1) \times 10^{-4}$  at applied fields of 3 T and 0.6 T, respectively. It can be seen that at 0.6 T the angle dependence does not fit a cosine squared dependence very well. This is because this field is insufficient to fully saturate the moment of the YIG layer out of the sample plane. The larger magnitude within this sample at a low applied field is due to the larger SHMR signal that exists when GGG is the chosen substrate; fig. 6.10 shows this as a function of temperature clearly. The field dependence beyond the saturation field shows that a PSHMR also exists in this sample, as expected from the Fe doping alone, and as observed in chapter 5 for the same level of doping on an  $\text{Al}_2\text{O}_3$  substrate. The magnitude of the change in signal between the two fields is  $(0.8 \pm 0.1) \times 10^{-4}$ ; this is a little less than the change for amorphous YIG, which is  $(1.10 \pm 0.06) \times 10^{-4}$ , but significantly larger than the change observed for etched YIG. This appears to suggest a larger PSHMR in the amorphous YIG sample, consistent with a slightly larger Pt thickness reducing the effective concentration within the film doped with Fe. These data also raise the question of whether the PSHMR and SHMR have a detrimental effect on one another. This concept is discussed further in the following section.

### 6.4.2 Temperature dependence of the ADMR

The temperature dependence of the ADMR in all orientations for all interfaces is shown in fig. 6.9. The definition of the measurement geometry is located in section 3.5.2, fig. 3.6. The  $\beta$ -plane MR is where the SHMR can be measured, the  $\gamma$ -plane the AMR and the  $\alpha$ -plane represents the sum of the SHMR and AMR. At first glance, it can immediately be seen that there are significant quantitative and qualitative differences in the ADMR for the different YIG/Pt interfaces under study. The sample considered to give the highest spin mixing conductance and largest magnitude SHMR is etched YIG, when prepared on a GGG substrate. The data for the  $\alpha$ -plane of this sample is shown in fig. 6.10. This is the sample type used for previous work in the group and has been shown to have consistently high quality [110; 161; 165; 196]. When the substrate is changed to YAG, the value of the SHMR decreases dramatically due to the reduced structural quality of the YIG film and hence reduced spin mixing conductance; this is apparent from the data shown in fig. 6.9c). The archetypal YIG/Pt bilayers consist of annealed or etched YIG, with the amorphous YIG and doped interface samples here facilitating a separation of spin torque related effects from interfacial magnetic effects.

When the YIG layer is amorphous, the ADMR has a strong temperature dependence in all three orientations. In the  $\gamma$ -plane, where conventional AMR would manifest [22; 23; 163; 181], the response remains smaller than in the  $\beta$ -plane throughout the temperature range, and only becomes significantly higher than zero below 100 K. This is consistent with a low temperature AMR found recently in YIG/Pd bilayers, believed to be due to spin-dependent scattering within a ferromagnetic phase of Pd from the MPE [118]. At higher temperatures, this effect is obscured by phonon scattering, which is spin-independent and as such unaffected by the MPE. A similar temperature dependence of ADMR in the  $\gamma$ -plane has been reported in section 5.3.3, fig. 5.17a), for Pt interfacially doped with Fe on an  $\text{Al}_2\text{O}_3$  substrate. This suggests that spin-dependent scattering manifests below 100 K to cause an imbalance in the scattering between parallel and perpendicular orientations of the applied magnetic field and charge current; in essence, an AMR. This may be due to physical magnetic impurities from intermixing at the interface, as suggested by measurements of Cu in section 6.3.1 on etched YIG, or from a localised MPE from Fe at the surface of the amorphous YIG. The  $\beta$ -plane,

## 6.4 Angle-dependent magnetoresistance in YIG/Pt bilayers

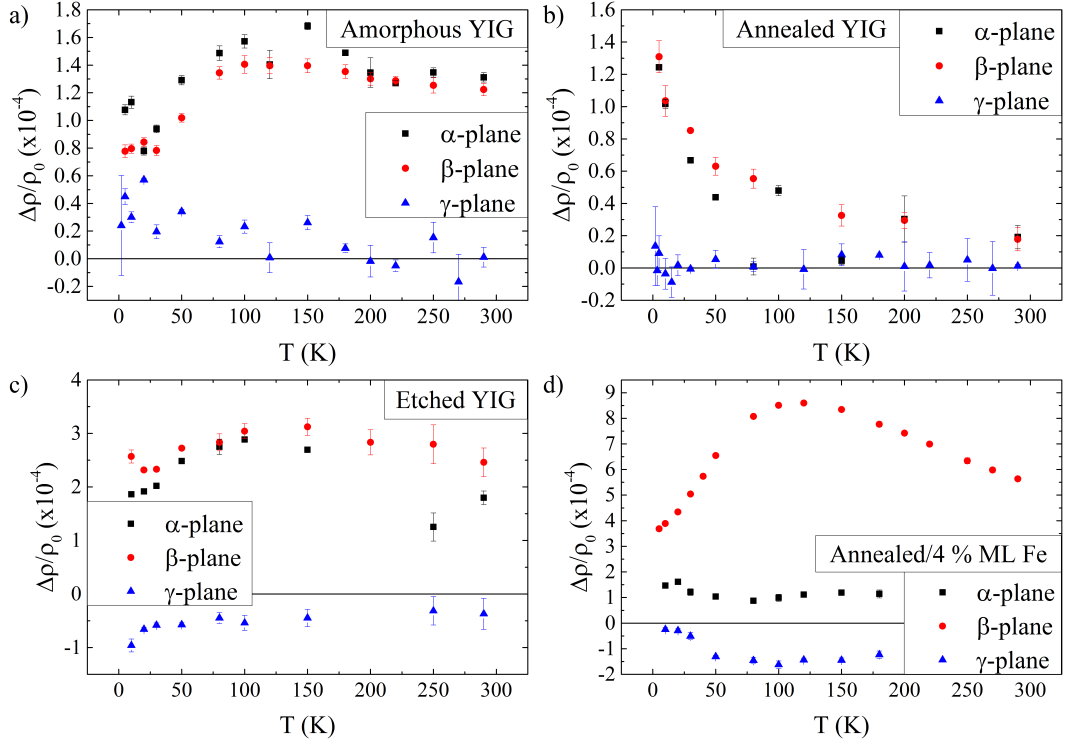


Figure 6.9: The temperature dependence of the ADMR in all three planes with an applied field of 3 T for 2.22 nm deposited on a) amorphous YIG, b) annealed YIG, c) etched YIG and d) annealed YIG with 4 % ML Fe on top.

where SHMR is usually measured, shows a signal of the order of  $10^{-4}$  throughout the temperature range studied. Its strong field dependence, shown in fig. 6.8a), suggests the presence of PSHMR. The absence of magnetic ordering in the YIG would appear to rule out the conventional SHMR effect; this is confirmed by perpendicular MR measurements in section 6.5, fig. 6.11a). The temperature dependence of this PSHMR is very different to that for Fe-doped Pt on  $\text{Al}_2\text{O}_3$ , however. The shape bears qualitative similarities to that for etched YIG, which is interpreted as being due to the temperature dependence of the conventional SHMR [17; 110; 113; 161]. The cause of this is currently unknown. The ADMR in the  $\alpha$  plane acts as an addition of the  $\beta$ - and  $\gamma$ -plane ADMRs, consistent with expectations.

Once the YIG has been annealed, the conventional SHMR is expected to appear due to the net magnetisation which is experienced by the spin current flowing nor-

## 6.4 Angle-dependent magnetoresistance in YIG/Pt bilayers

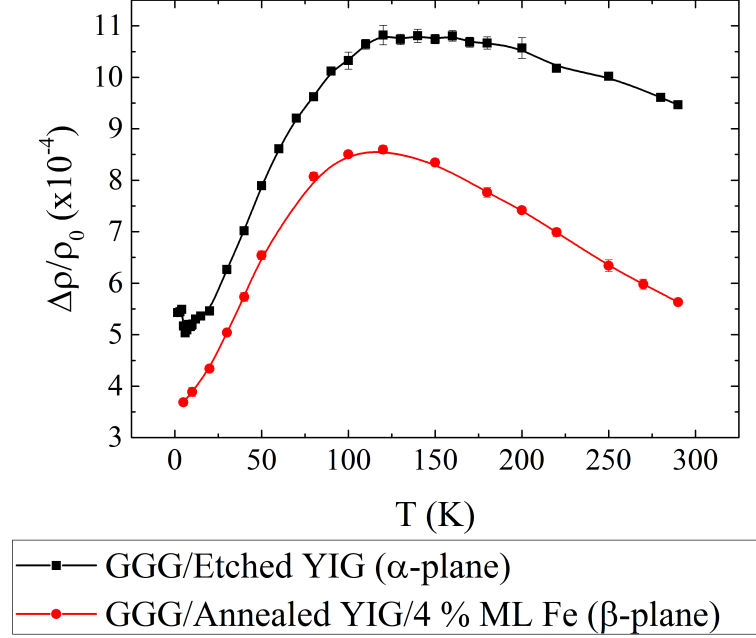


Figure 6.10: The temperature dependence of the magnetoresistance in the  $\alpha$ -plane with an applied field of 3 T for 2.2 nm Pt deposited on etched YIG (black squares) and in the  $\beta$ -plane for annealed YIG with 4 % ML Fe on top (red circles). The substrate used is GGG.

mal to the film surface. The ADMR data for this sample is shown in fig. 6.9b). The  $\gamma$ -plane ADMR does not rise above zero with any statistical significance throughout the temperature range under study, suggesting a dramatically reduced concentration of magnetic sites at the YIG/Pt interface, and hence a significant reduction in the amount of spin-dependent scattering present at low temperatures. The temperature dependence of the  $\beta$ -plane ADMR, however, is drastically different to that previously reported for YIG/Pt bilayers [110; 161] and bears a closer qualitative and quantitative similarity to the temperature dependence of the PSHMR observed in Fe-doped samples in fig. 5.17. The exceptionally small magnitude of this ADMR is due to a combination of the reduced YIG structural quality on a YAG substrate in comparison to GGG, but also due to the lower concentration of Fe sites at the interface, as evidenced by the negligible AMR signal. The strong field dependence of the  $\beta$ -plane ADMR, shown in fig. 6.8b), suggests that the majority of this signal is due to the PSHMR, and indeed its magnitude and temperature dependence are very similar to that observed for the minimal

## 6.4 Angle-dependent magnetoresistance in YIG/Pt bilayers

---

concentration sample explored in chapter 5. This increase with decreasing temperature is more in-keeping with a paramagnetic signal and cannot be explained by the current theory of the SHMR [17; 113]. The  $\alpha$ -plane ADMR is almost identical to the  $\beta$ -plane ADMR, acting again as the sum of the  $\beta$ - and  $\gamma$ -plane ADMRs, as expected.

Upon etching, the  $\beta$ -plane MR increases significantly in magnitude and its shape as a function of temperature, shown in fig. 6.9c), is more in-line with that expected for the conventional SHMR [110; 113; 161]. The dependence upon the field indicates the presence of a sizeable PSHMR in addition to the conventional SHMR. A small negative AMR is present throughout the temperature range under study, becoming more significant below 150 K. This is attributed to enhanced spin-dependent scattering in this temperature region, and agrees with the negative AMR found in fig. 6.9d) for a  $\delta$ -layer of Fe placed at the YIG/Pt interface. The  $\alpha$ -plane MR experiences an increase in magnitude at very low temperatures, where the magnitude of the negative AMR increases, which is inconsistent with the idea of the  $\alpha$ -plane MR being simply the sum of the  $\gamma$ - and  $\beta$ -planes MRs, though their absolute magnitudes do add to produce this  $\alpha$ -plane magnitude. The cause of the change in sign of the AMR is unknown, as the AMR observed for Fe-doped Pt on an  $\text{Al}_2\text{O}_3$  substrate in chapter 5 is positive. This hence may be a consequence of the enhanced spin mixing conductance, although more work needs to be done in this area to characterise this effect.

The data in fig. 6.9d) represent a sample grown on a GGG substrate, which intrinsically provides a higher value of the SHMR due to the higher quality of YIG. Fig. 6.10 shows the magnetoresistance in the  $\alpha$ -plane with an applied field of 3 T for 2.28 nm Pt on etched YIG (black squares) and in the  $\beta$ -plane for annealed YIG with a delta layer of Fe on top (red circles). The larger magnitude of the  $\alpha$ -plane ADMR for etched YIG may be due to the addition of an AMR signal, but its persistence to high temperatures make it likely that this increase is actually due to a better spin mixing conductance at the interface. This could be due to properties from the etching process, or the Fe impurities may reduce the spin mixing conductance, therefore reducing the magnitude of the SHMR. More data are needed on the magnetotransport phenomena of these samples to determine the cause definitively. The  $\beta$ -plane ADMR in the Fe-doped sample

## 6.5 Conventional magnetoresistance and its temperature dependence in YIG/Pt bilayers

---

shows a similar temperature dependence to the SHMR in etched YIG on GGG. Its reduced dependence upon the field, shown in fig. 6.8d), also indicates that the majority of this signal is due to the conventional SHMR. A small PSHMR is present from the Fe doping, but the ADMR and its temperature dependence is dominated by the SHMR. In order to provide a better comparison for a true study of interfacial effects, a study of an Fe-doped sample of annealed YIG deposited on YAG would be most useful.

It is hence clear that the interface structure strongly affects the ADMR in YIG/Pt bilayers. For amorphous YIG, a PSHMR persists even without long range magnetic order in the YIG film. The etching process is seen to improve the spin mixing conductance and cause the conventional SHMR to emerge, while largely a PSHMR is seen to be present for YIG which has been annealed but not etched. This research highlights the importance of improving the interface quality for a direct observation of the SHMR. The use of a GGG substrate is seen to greatly increase the value of the SHMR in conjunction with the etching process; the peak magnitude for etched YIG on YAG in the  $\alpha$ -plane is found to be  $(2.88 \pm 0.04) \times 10^{-4}$  at 100 K, whilst for etched YIG on GGG this value increases to  $(10.8 \pm 0.1) \times 10^{-4}$  in the region 120 - 180 K. To obtain high quality samples for the detection of the SHMR, it is hence found to be optimal to use a GGG substrate in conjunction with the piranha etch process.

## 6.5 Conventional magnetoresistance and its temperature dependence in YIG/Pt bilayers

The conventional magnetoresistance (MR) is also a useful tool for determining the scattering occurring at the interface between YIG and Pt. The perpendicular orientation is explored in this section for the four different interfaces discussed within this chapter. The shape is presented.

The perpendicular MR for the four samples is displayed in fig. 6.11. At higher temperatures, the MR is positive for amorphous, annealed, etched and annealed YIG with 4 % ML Fe, with quantitative differences between the samples. A negative MR

## 6.5 Conventional magnetoresistance and its temperature dependence in YIG/Pt bilayers

---

manifests below 30 K for the sample with amorphous YIG. For annealed YIG, the MR becomes strongly positive at lower temperatures. This behaviour highlights the reduction of magnetic scattering from Fe at the interface, which causes the negative MR observed in fig. 5.14. As in this case, fitting with quantum interference requires a large value of  $B_s$  and a small value of  $B_{so}$  which are inconsistent with known data regarding this system. The narrow central feature observed for etched YIG on YAG is the manifestation of the SHMR as the magnetisation is rotated out of the plane, and plots showing this are not amenable to fits of quantum interference phenomena. The constantly positive nature of the MR at higher fields is consistent with a reduced interfacial Fe concentration in comparison to amorphous YIG. For annealed YIG with 4 % ML Fe on top, a central feature with a sharply positive MR develops. This has a width equivalent to the expected out of plane coercivity of the YIG layer grown on GGG, i.e. approximately 1 T, and as such represents the value of the conventional SHMR [17; 113]. At higher fields, the trend is qualitatively similar to that observed for amorphous YIG, with Fe impurities causing a negative MR below 20 K, as observed in section 5.3.2.

The magnitude of the MR in all three orientations at an applied field of 3 T are plotted in fig. 6.12. The shape and magnitudes vary greatly depending upon the interface type. For amorphous YIG, the temperature dependence of the MR in all three orientations bears a close resemblance to that observed for Fe-doped Pt in fig. 5.15. The positive magnitude is comparable to that for a sample doped with  $\delta$ Fe at the interface. The negative magnitude is somewhat smaller, however, indicating a lower concentration of magnetic scattering sites. At higher temperatures, the positive MR in the longitudinal and perpendicular orientations remains at a fairly constant magnitude in contrast to the reduction in magnitude observed for Fe-doped Pt at the highest temperatures. This may be due to a reduced side-jump scattering mechanism, as this tends to be more prevalent at higher temperatures, but there is little exploration of this in the literature. A coherent theory is required to explain these data quantitatively.

The temperature dependence of the MR for annealed YIG is shown in fig. 6.12b). Here, the transverse MR is seen to be negligible until the negative MR develops below 50 K. The magnitude of this negative MR is smaller than for annealed YIG, either

## 6.5 Conventional magnetoresistance and its temperature dependence in YIG/Pt bilayers

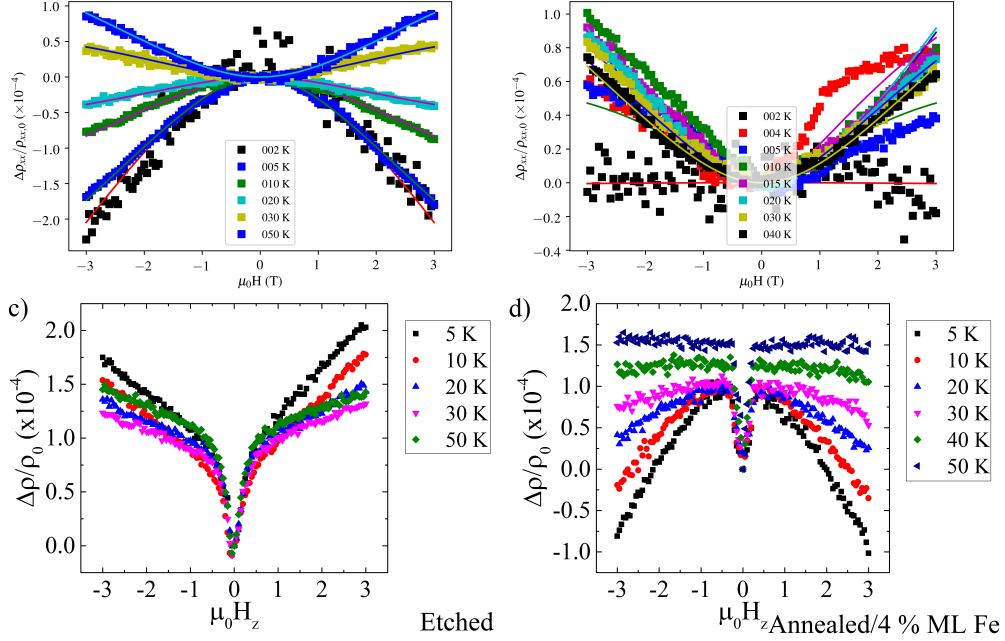


Figure 6.11: The perpendicular magnetoresistance as a function of both temperature and field below 50 K for 2 nm Pt on a) amorphous YIG, b) annealed YIG, c) etched YIG and d) annealed YIG doped with 4 % ML Fe. Solid lines in a) and b) represent fits to quantum interference phenomena.

with or without Fe doping, reinforcing the hypothesis of reduced concentration of interfacial moments within this sample. The shape of the longitudinal and perpendicular MR magnitude as a function of temperature is novel, with a peak magnitude at 20 K of  $(0.81 \pm 0.01) \times 10^{-4}$  in the longitudinal orientation and at 10 K of  $(0.9 \pm 0.1) \times 10^{-4}$  in the perpendicular orientation. The magnitude of these MRs remains positive throughout the temperature range considered. This shape appears to be a result of the YIG interface, as this is not observed for the same thickness of Pt in fig. 5.6b).

The longitudinal MR for the etched YIG sample, shown with the other orientations in fig. 6.12c), shows a qualitatively similar shape to the temperature dependence of the SHMR shown in fig. 6.9c). This concurs with the hypothesis that the central feature observed is related to the improved spin mixing conductance in this sample and indicates the MR is dominated by this contribution. The transverse MR has the same

## 6.5 Conventional magnetoresistance and its temperature dependence in YIG/Pt bilayers

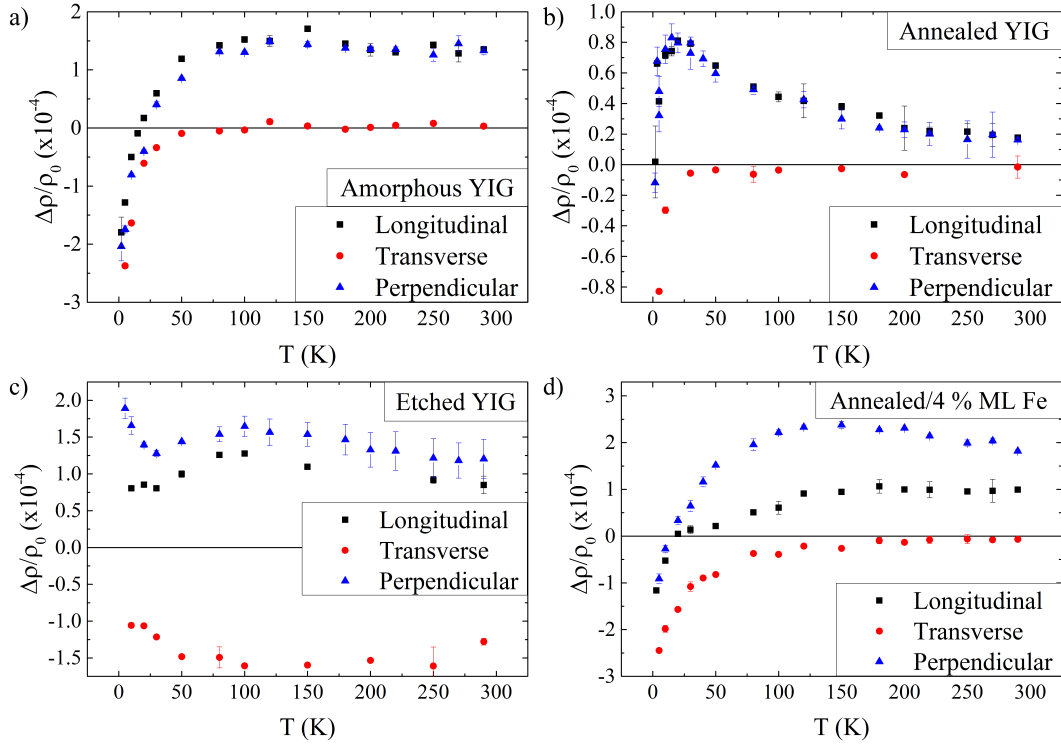


Figure 6.12: The temperature dependence of the magnetoresistance at an applied field of 3 T in all three orientations for 2.22 nm Pt on a) amorphous YIG, b) annealed YIG, c) etched YIG and 2.28 nm Pt on d) annealed YIG with 4 % ML Fe.

qualitative temperature dependence, but reflected in the  $x$ -axis at  $y = 0$  as the central feature has the opposite sign in the transverse MR. The perpendicular MR exhibits the magnitude and temperature dependence of the SHMR, due to the magnetisation of the YIG being rotated out of the plane during measurement and hence showing the SHMR before saturation. Above saturation, another positive MR is observed, producing an increase compared to the longitudinal MR observed. Below 50 K, an additional increase is observed in the perpendicular MR. This follows the reduction of the negative AMR magnitude and is only prevalent in the region where phonon scattering is greatly diminished.

To summarise, it is shown that a negative MR manifests in all three orientations below 50 K for amorphous YIG and annealed YIG doped with 4 % ML Fe, and is attributed to the presence of Fe impurities. The temperature dependence of the MR

in the etched YIG sample represents the SHMR, in both positive and negative values, for all orientations, due to the large low-field contribution from an enhanced spin mixing conductance; this comes from the SHMR being clearly distinguishable in the MR. Annealed YIG shows a novel temperature dependence for both the perpendicular and longitudinal MR, with a sharp decrease in magnitude at very low temperatures. In the transverse orientation, a negative MR manifests below 50 K, which is caused by the presence of Fe impurities. These data hence reinforce some of the conclusions from section 6.4.2, most notably that amorphous YIG possesses the largest concentration of interfacial magnetic impurities without doping.

## 6.6 The interfacial Hall effect

Bilayers of Pt and YIG have recently been shown to exhibit an unconventional Hall effect, with reports from various groups showing responses which differ both qualitatively and quantitatively [21; 22; 58; 112; 163; 164]. The origins of this Hall effect are also debated in the literature, with a low-field contribution observed by some cited as being due to the spin-mixing conductivity at the interface, termed the spin Hall-anomalous Hall effect (SH-AHE) [58; 113], whilst a non-linear high-field component observed by others is thought to be due to the MPE [21; 22; 112; 163]. In this section, the dependence of the Hall response on the interface is reported.

The form of the Hall resistivity as a function of field is displayed in fig. 6.13 for various YIG/Pt interfaces. Regardless of the method of interface preparation, in all cases the shape bears qualitative similarities to that observed in chapter 5, fig. 5.18 for ultra-thin Pt films interfacially doped with a discontinuous layer of Fe. As in chapter 5, the shape appears Langevin-like but scaling with  $B/T$  shows that this is not an appropriate method. This shape is also qualitatively consistent with those observed for YIG/Pt bilayers in recent publications [21; 22; 112; 163]. The AHE persists in all cases to a field higher than the out-of-plane saturation field of the YIG layer [21; 58; 112; 161] and thus cannot originate from the magnetic properties of this layer. Quantitatively, the Hall resistivity is strongly dependent upon the interface preparation method with a much larger value of almost 2000 p $\Omega$ m at 8 T and 1.6 K for a sample doped with Fe,

## 6.6 The interfacial Hall effect

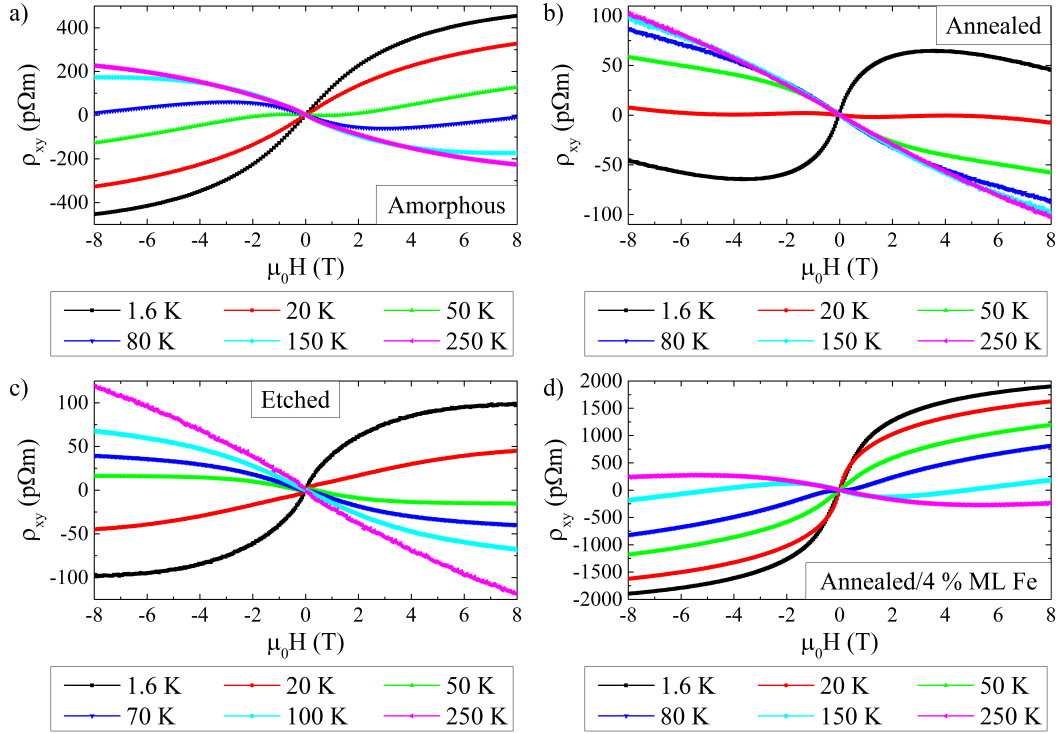


Figure 6.13: The Hall resistivity as a function of field at various temperatures for 2.22 nm deposited on a) amorphous YIG, b) annealed YIG, c) etched YIG and d) annealed YIG with 4 % ML Fe on top. Lines shown are guides for the eye.

compared to around 50 pΩm under the same conditions for an annealed sample without the Fe dopants. A change in sign of  $R_H$  can also be observed between these two samples at this temperature. The amorphous YIG and interfacially doped YIG exhibit the largest Hall resistivities, with the annealed and etched samples have relative quantitative consistency in the Hall resistivity with a peak magnitude of around 100 pΩm. The very low field component, crucial for observation of the SH-AHE, is discussed further in section 6.6.1. The ordinary and anomalous Hall coefficients for these samples, extracted as described in section 5.3.4, are shown as a function of temperature in fig. 6.15.

The temperature dependence of  $R_H$  and  $R_S$  across the various interfaces appears to indicate a trend of a changing concentration of interfacial ferromagnetic moments. In chapter 5, it has been shown that different concentrations of interfacial Fe impurities in

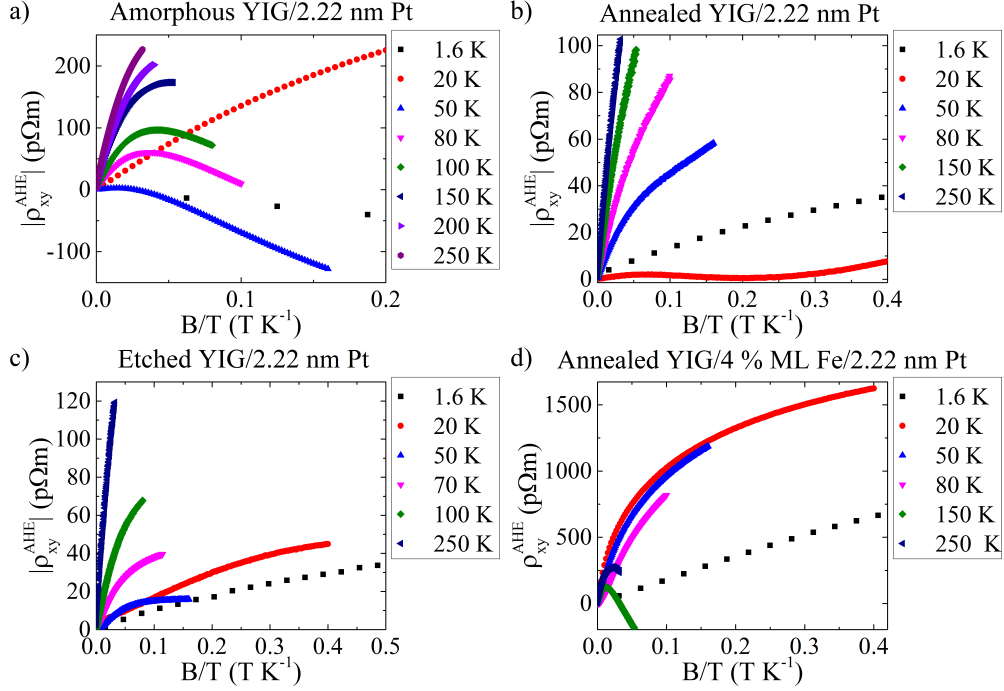


Figure 6.14: *The Hall resistivity scaled with the applied field over the temperature for 2.22 nm Pt on a) Amorphous YIG, b) Annealed YIG, c) Etched YIG and d) Annealed YIG doped with 4% ML Fe.*

an ultrathin Pt film produce qualitatively similar behaviour in the Hall coefficients as a function of temperature. This is shown for two concentrations of Fe in figs. 5.23 and 5.24. A lower concentration of interfacial moments is hence represented by a consistently negative  $R_H$  throughout the temperature range studied, a lower value of  $R_S$  and a lower temperature at which a change in sign occurs for  $R_S$ . Using this data as a basis, it is hence possible to determine the relative concentrations of interfacial moments in the four samples represented in fig. 6.15. Thus, the smallest concentration is observed for Pt deposited on annealed YIG, represented by red circles in fig. 6.15; a change in sign of  $R_S$  is observed below 30 K. After the etching process has been applied to a concurrently produced sample, a larger concentration of interfacial moments is seen to manifest, as  $R_H$  exhibits a change in sign below 50 K and  $R_S$  below 40 K; this sample is represented by blue upward triangles in fig. 6.15.

Amorphous YIG, when used as a substrate for ultrathin Pt, is seen to exhibit a

## 6.6 The interfacial Hall effect

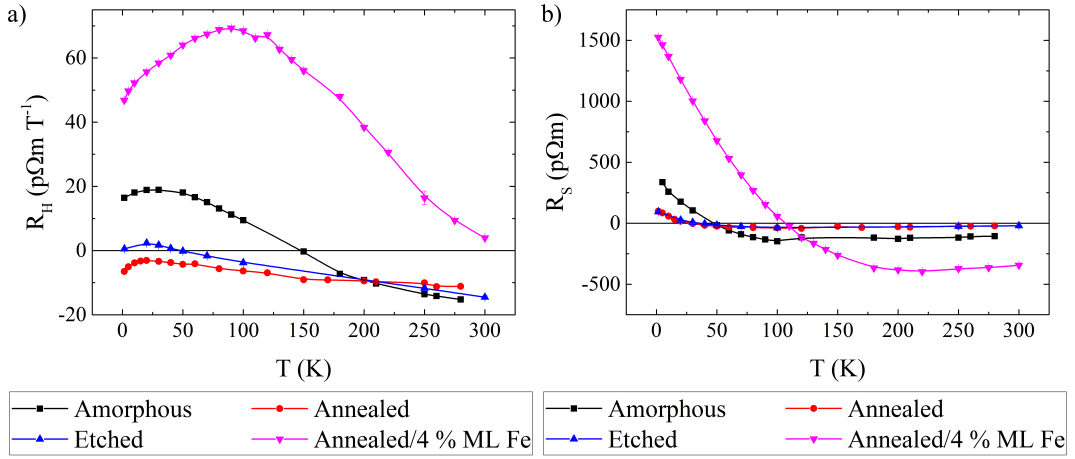


Figure 6.15: The a) ordinary and b) anomalous Hall coefficients as a function of temperature for 2.22 nm Pt deposited on various YIG interfaces. A YAG substrate is used for all but the sample with 4 % ML Fe, which has a GGG substrate. Lines shown are guides for the eye.

large increase in interfacial moments based upon the Hall data, in comparison to ordered YIG samples. This significant change indicates there is a significantly larger concentration of moments from Fe sites at the YIG/Pt interface in this system. The amorphous YIG under study did not exhibit a net magnetic response when magnetometry measurements were performed. This means that the anomalous Hall effect in this system is due entirely to the moments at the interface between the materials.

The anomalous Hall effect observed is attributed to extrinsic spin-orbit scattering from magnetic sites at the YIG/Pt interface. As there is no intrinsic anomalous Hall effect observed in ultrathin Pt, shown in chapter 5 fig. 5.9 where the dependence on field is linear, the addition of impurity sites and disorder at the interface is the cause of the nontrivial field dependence of the Hall resistivity. Scattering with side jump is known to be a prevalent mechanism for the anomalous Hall effect in dilute alloys containing Fe [47; 48]. This is particularly apparent in YIG with 4 % ML Fe on the surface, as in this case the ordinary Hall coefficient remains positive throughout the temperature region under study. The temperature dependence of the anomalous Hall coefficient for all samples, shown in fig. 6.15b), bears qualitative similarities to that of ultrathin Pt experiencing a magnetic proximity effect from an ionic liquid [86], including the trend for concentration dependence. The scaling proposed in equation 2.27 is attempted to

## 6.6 The interfacial Hall effect

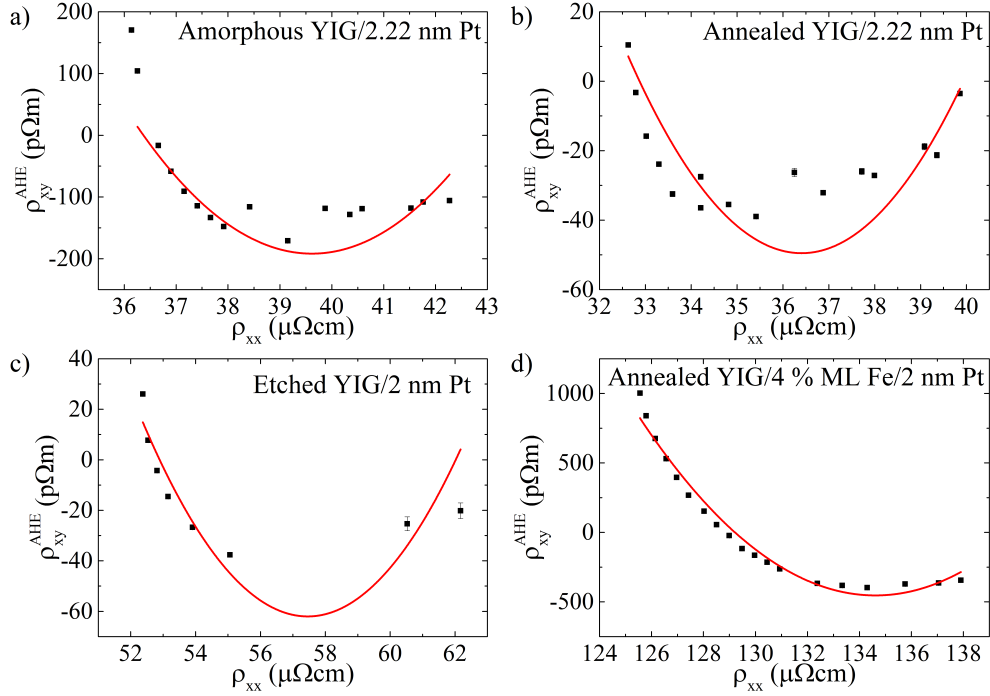


Figure 6.16: Resistivity scaling for the anomalous Hall coefficient  $R_S$ , plotted as  $\rho_{xy}^{\text{AHE}}$ , for 2.2 nm Pt on a) Amorphous YIG, b) Annealed YIG, c) Etched YIG and d) Annealed YIG doped with 4 % ML Fe.

be applied to the data, as shown in fig. 6.16, with parameters in table 6.2. In order for the theory to fit the data, an intercept must be added to the quadratic equation, as per equation 5.2, which is unphysical. The traditional scaling expected for the skew and side-jump scattering in the anomalous Hall effect is hence not applicable to these samples, either doped with Fe or grown on YIG, and hence the coefficients obtained from the fit are also not representative of the physical picture and cannot be used to draw conclusions.

The findings from section 6.4 and previous work [18; 110; 161] have shown that the piranha etch process enhances the spin mixing conductance at the YIG/Pt interface and hence also enhances the magnitude of the SHMR. The findings from the Hall effect also show an increase in the magnetic behaviour of the interface, raising questions about the mechanisms by which the SHMR is enhanced due to the etching. It has been shown in chapter 5 that a paramagnetic spin Hall magnetoresistance (PSHMR) can be

Table 6.2: The parameters found from scaling the anomalous Hall resistivity with the longitudinal resistivity as per equation 5.2, shown in figs. 5.21 and 6.16.  $R_{sq}$  represents the goodness of fit.

Substrate	$\Phi$ (mrad)	$\kappa$ (MSm <sup>-1</sup> )	C ( $\mu\Omega\text{cm}$ )	$R_{sq}$
Al <sub>2</sub> O <sub>3</sub> / $\delta$ Fe	-(70 $\pm$ 10)	0.10 $\pm$ 0.02	1.1 $\pm$ 0.2	0.89826
Al <sub>2</sub> O <sub>3</sub> /4 % ML Fe	-(55 $\pm$ 4)	0.079 $\pm$ 0.007	0.92 $\pm$ 0.07	0.9486
Amorphous YIG	-(140 $\pm$ 30)	0.18 $\pm$ 0.03	2.8 $\pm$ 0.5	0.69879
Annealed YIG	-(29 $\pm$ 4)	0.040 $\pm$ 0.005	0.52 $\pm$ 0.07	0.79793
Etched YIG	-(34 $\pm$ 9)	0.030 $\pm$ 0.008	0.9 $\pm$ 0.3	0.82712
Annealed YIG/4 % ML Fe	-(420 $\pm$ 30)	0.16 $\pm$ 0.01	28 $\pm$ 2	0.97707

measured in interfacially doped dilute PtFe alloys, and this may contribute to the signal measured in etched samples. One measure of the strength of the spin mixing conductivity from magnetotransport, without any enhancement from interfacial Fe doping, is the SH-AHE, discussed in section 6.6.1.

### 6.6.1 The spin Hall-anomalous Hall effect

The spin Hall-anomalous Hall effect (SH-AHE) is a manifestation of the imaginary part of the spin mixing conductance, leading to a field-dependent transverse voltage below the YIG saturation field [113], as described in section 2.5. This appears as an additional transverse voltage at fields below 1 T on top of the other Hall effects observed. Experimentally, this has been observed at 300 K in a YIG/Pt bilayer with a Pt thickness of 2 nm [58]. In addition to the high field curvature, an SH-AHE is also observed in some of the YIG/Pt systems under study, and a selection of these data are shown in fig. 6.17.

It can be seen that the SH-AHE has a larger magnitude when a GGG substrate is used than for YAG, indicating that the imaginary component of the spin mixing conductance is also enhanced for this substrate, as the enhanced SHMR shows the real component is likewise improved. No SH-AHE is observed for YIG which has not undergone the piranha etch surface treatment, indicating that this is crucial for a

## 6.6 The interfacial Hall effect

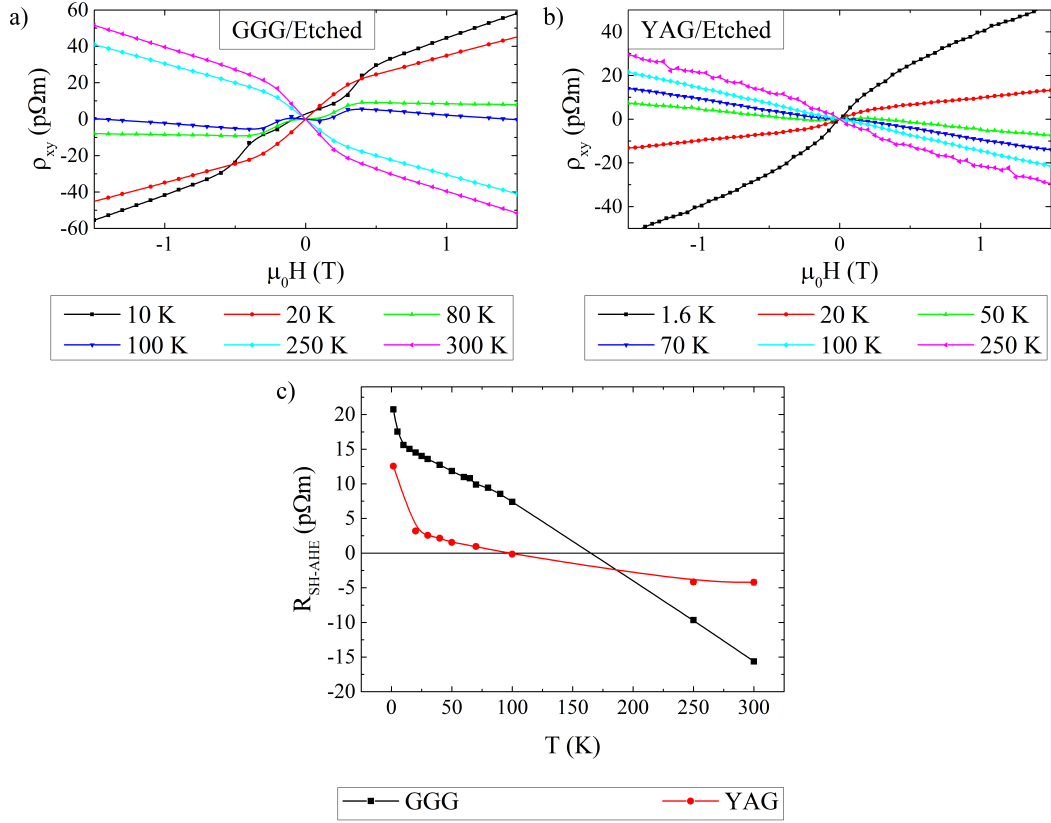


Figure 6.17: The spin Hall-anomalous Hall effect observed for a) GGG/Etched YIG/2.22 nm Pt, b) YAG/Etched YIG/2.22 nm Pt and c) the temperature dependence of the spin Hall-anomalous Hall coefficient for both systems.

significant improvement in the spin mixing conductance, in line with the other magnetotransport data shown. On a GGG substrate, a more complex field dependence is observed within the SH-AHE region at some temperatures, and the cause of this is unclear. On a YAG substrate, the field dependence in the SH-AHE region is linear, as has been previously observed [58]. There are currently no temperature dependence data for this phenomenon in the literature, and that found in this study is shown in fig. 6.17c). The spin Hall-anomalous Hall coefficient,  $R_{SH-AHE}$ , is here defined similarly to  $R_S$ , with half the difference between the  $y$  intercepts of two linear fits in the low field region used to deduce its value. The trend is very different to that of the anomalous and ordinary Hall coefficients in these samples, and is more similar to the temperature dependence of the anomalous Hall coefficient observed for 10 nm Pt on YIG in the lit-

erature [22], with its sharp increase in magnitude at the lowest temperatures observed. It is clear that a much stronger effect is observed in GGG, but both substrates experience a change in sign, with that for GGG occurring at a higher temperature. More data are needed to fully characterise this sign change in both samples.

## 6.7 Summary

The MPE plays a role at the YIG/Pt interface. Techniques employed on similar samples, such as scanning transmission electron microscopy (STEM) at the superSTEM facility [165] and cross-sectional transmission electron microscopy (TEM) [110; 161] show an ordered interface, with intermixing confined to within 1-2 monolayers. This intermixing region is difficult to resolve with these techniques, however, and a concentration of a few percent of one monolayer is beyond the scope of current microscopy techniques. It is thus difficult to definitively state whether the cause of the observed interfacial magnetotransport phenomena lies with a physical intermixing of chemical elements at the interface, or rather if a localised MPE from Fe sites at the YIG surface is the cause. The results from the Kondo effect for thin Cu films deposited on YIG, discussed in section 6.3.1, suggest that some degree of intermixing is present at the interface. Since Cu lacks other anomalous magnetotransport phenomena, such as the anomalous Hall effect, this suggests that either the MPE or the high spin-orbit coupling in Pt plays a role in enhancing these interfacial phenomena. Further work on metals with high spin-orbit coupling which are further from satisfying the Stoner criterion, such as W, Ir, or Rh, could help to illuminate the mediating factor. Systems of Cu doped with metals such as Ir or Bi have been shown to produce a large extrinsic spin Hall effect [10; 12] and are promising candidates for MPE-free investigation of spin transport phenomena at the YIG interface.

It is found that the magnetotransport phenomena in YIG/Pt bilayers depend strongly upon the interface preparation method used. Work on amorphous YIG has shown the interfacial effects present for Fe-doped Pt in the magnetotransport, with an interfacial AHE and negative MR at low temperatures. The piranha etching surface treatment is

found to not only enhance both the real and imaginary components of the spin mixing conductance, as demonstrated by an enhanced SHMR and the appearance of the SH-AHE, but also to enhance the interfacial magnetic effects observed in the magnetotransport. The substrate choice plays a large role in the quality of the spin mixing conductivity, with a larger SHMR and SH-AHE found when using a GGG substrate in conjunction with piranha etching, owing to the reduced strain in this system.

---

# CHAPTER 7

---

Conclusions and future work

---

Throughout this thesis, the effect of extrinsic spin-orbit scattering on magnetotransport phenomena has been considered. In an entirely non-magnetic system, it is found that a discontinuous non-magnetic impurity  $\delta$ -layer significantly modifies both the resistivity and ordinary Hall coefficient in an impurity-dependent manner. The position of the impurity  $\delta$ -layer within the film is found to have a significant impact upon the magnitude of the resistivity, with a peak value emerging at the centre of the film. This is consistent with theoretical predictions using a model of parallel conductors which is independent of the impurity type. It has been found that the transport in thin films doped with impurities shows two new effects - the transport depends on the spin state of the impurity and on its position. This will be published in conjunction with Dr. Martin Gradhand, who is currently performing calculations to explain the physics behind these phenomena. In future work, extending the film thickness until the effect diminishes would enable a lengthscale over which the effects persist to be defined and hence help to shape the theory. The use of impurities which exhibit low spin-dependent scattering could help elucidate all the mechanisms behind the position dependent effect and allow for extraction of skew, spin and side jump scattering contributions with an appropriate choice of impurity.

Placing an impurity  $\delta$ -layer of Fe on an  $\text{Al}_2\text{O}_3$  substrate beneath an ultrathin Pt film has been shown to modify the magnetotransport phenomena in comparison to the clean ultrathin Pt case. Weak anti-localisation is destroyed and a negative magnetoresistance, with magnitude dependent upon the concentration of impurities, manifests at low temperatures in all orientations. A paramagnetic spin Hall magnetoresistance (PSHMR) is discovered in this system which persists to high temperatures for 4 % ML Fe beneath 2 nm Pt, but is only strongly apparent below 50 K for a much lower concentration of Fe. An AMR, of magnitude less than  $1 \times 10^{-4}$ , is observed below 50 K for both Fe concentrations, with a magnitude which increases with increasing concentration. The anomalous Hall coefficient varies with temperature and concentration similarly to systems where an AHE is induced by the MPE [86]. The ordinary Hall coefficient is also found to depend strongly upon the temperature and concentration, changing sign at a higher concentration of Fe. The induced anomalous Hall effect persists to a thickness of 5 nm Pt with 4 % ML Fe beneath. These magnetotransport phenomena have not

---

been explored previously in the literature, and this represents the first time magneto-transport phenomena have been explored for Pt with an impurity layer localised at the interface with the substrate. These data provide an insight into how a localised MPE can cause a PSHMR and an AMR and help to shed light on some of the phenomena which emerge due to localised magnetism at the YIG/Pt interface. These results will be published as they show important effects which influence the interpretation of measurements such as the SHMR, which are currently of great interest.

It has been found that the magnetotransport in YIG/Pt bilayers is strongly dependent upon the method used to prepare the YIG interface. Measurements of resistivity as a function of temperature show a minimum at low temperature which observes an additional contribution due to the enhanced electron-electron interaction. Cu of various thicknesses exhibit a Kondo effect when deposited on YIG, which diminishes at higher thickness, indicating intermixing takes place at the interface. A field dependence of the ADMR in the  $\beta$ -plane, i.e. SHMR orientation, is observed showing that the PSHMR contributes to the measured signal. This is particularly prominent for amorphous YIG, which has low conventional SHMR, and annealed YIG, which exhibits a particularly low SHMR. Placing an impurity  $\delta$ -layer of Fe between YIG and Pt dramatically enhances the magnitude of the observed SHMR due to the contribution from the PSHMR. A small AMR is observed in all YIG/Pt bilayers, but with differing signs.

It is found that the choice of substrate impacts the quality of the YIG/Pt interface and hence the spin mixing conductance and SHMR observed. A GGG substrate provides a larger value of the SHMR than a YAG substrate, owing to the reduced strain and improved stoichiometry of the YIG crystal structure. Etching the top surface of the YIG is found to enhance the spin mixing conductance at the interface, as evidenced by an enhanced SHMR and the manifestation of the SH-AHE. The temperature dependence and substrate dependence for the SH-AHE has been explored for the first time and it is shown to undergo a change in sign at a temperature dependent upon the substrate choice. The temperature dependence is distinct from that of  $R_H$  and  $R_S$ , and a new model is required to understand this and its implications for the imaginary component of the spin mixing conductance. These data will soon be published.

---

An anomalous Hall effect which is not Langevin-like is observed up to high fields in YIG/Pt bilayers. The temperature dependence of the ordinary and anomalous Hall coefficients show that the various types of YIG produce differing amounts of side-jump, attributed to differing amounts of exposed metallic Fe at the surface. The side-jump contribution to the observed anomalous Hall effect is found to be strongly dependent upon the interface preparation method. Contrasting the Hall coefficients with those reported here for Pt with a localised discontinuous layer of Fe, relative concentrations are extracted. Etching the YIG surface is seen to produce a large SHMR in addition to a large PSHMR.

It has hence been shown that extrinsic spin-orbit scattering can have a dramatic effect on the magnetotransport of thin films. Expanding the work of in non-magnetic systems may lead to spin Hall effect devices with a higher efficiency of charge to spin current conversion. These impurity delta layer systems could also be investigated in an ultrathin form on a YIG substrate in order to investigate the possibility of a large extrinsic SHMR which is free from MPE, leading to a strong candidate for the detection of the magnetic state in YIG via spintronics. There is little doubt that extrinsic spin-orbit phenomena have the capability to enhance the spintronics of the future.

---

# APPENDIX A

---

## X-ray Reflectivity of YIG

X-ray reflectivity data were collected for samples of YIG at various stages of the preparation process. The key stages at which data are taken are after deposition of amorphous YIG, after the annealing process and after the etching process. Representative x-ray reflectivity data are shown for a YIG sample on a YAG substrate at these three stages in fig. A.1.

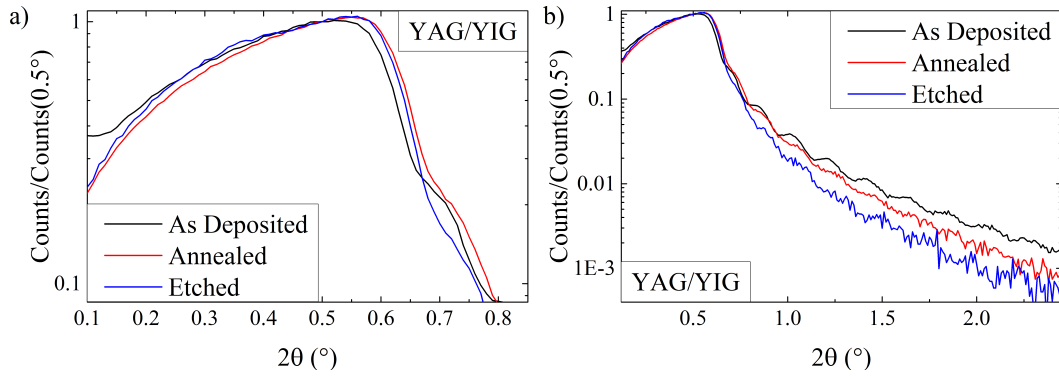


Figure A.1: X-ray reflectivity data are shown for YIG on YAG, grown to a thickness of  $(38 \pm 1)$  nm, at various stages of the preparation process. The changes in the critical edge are shown in a), whilst b) shows the Kiessig fringes. Data are normalised to the count rate for  $2\theta$  at  $0.5^\circ$ .

Qualitatively one can determine a trend where the critical edge moves to higher angle for the annealed sample compared to the amorphous sample, then recedes slightly following the piranha etch process; this is shown in fig. A.1. This qualitative trend is observed for substrates of both YAG and GGG across six plates of sample growth, so can be deemed a statistically significant trend. As the critical edge is known to give information regarding the electron density at the film surface [204], one can then surmise that the electron density is highest for the annealed film compared to the other surfaces. In order to investigate this trend, the GenX fitting program [205] was used to fit the data with various models of sample structure. The results of these fits are shown in fig. A.2 and table A.1.

When producing these fits, various models were tried with varying success. It was found that modelling all of the films with one layer of YIG on a YAG substrate gave poor fits to the critical edge of the film with a high figure of merit (FOM) corresponding to poor agreement with the data. Modelling a layer of  $\text{Fe}_2\text{O}_3$  on top of the YIG

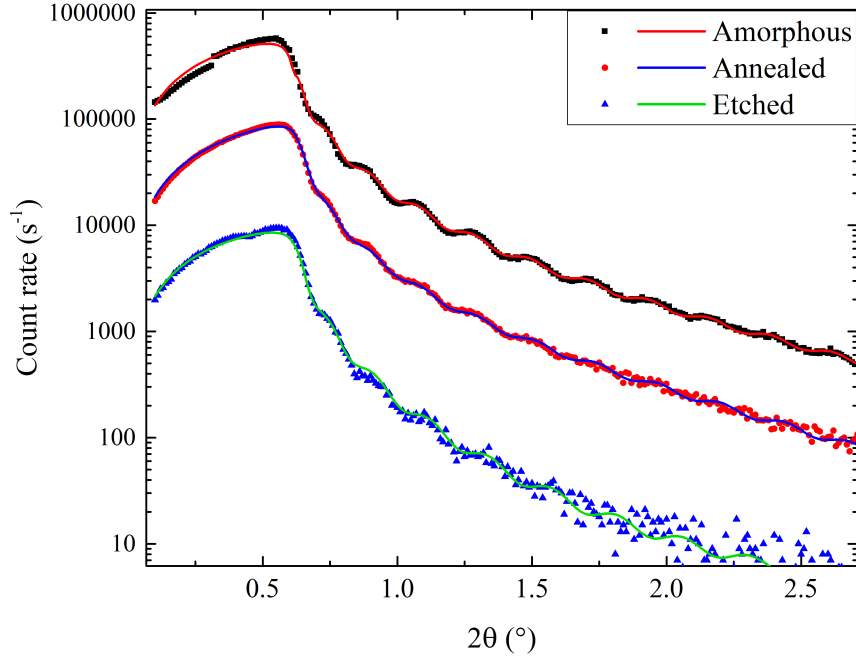


Figure A.2: X-ray reflectivity data for amorphous (as-deposited), annealed and etched YIG on a YAG substrate are shown with fits obtained from GenX [205] using various models described in table A.1.

likewise provided poor agreement with the critical edge position, although a layer of  $\text{Fe}_3\text{O}_4$  could provide convincing fits to all three datasets. The best fits, i.e. those with the lowest FOM, are shown in fig. A.2 and table A.1, however. For amorphous and etched YIG, these consist of a layer of graded YIG, i.e. a top layer with an electron density which differs from the remainder of the YIG in the sample. For the amorphous sample, this layer proved to have a higher density than expected of YIG, whilst for the etched sample this layer had a slightly lower density. When considering the physical process of the piranha etch, this result agrees with expectation. For the amorphous sample, the layer of YIG beneath the top layer is of a lower density than crystalline YIG, as one might expect. The annealed sample, however, requires a top layer with different chemical structure to fit the critical edge. Both iron oxides produced poor fits, with the best match coming from considering a layer of yttria,  $\text{Y}_2\text{O}_3$ , atop the YIG. The YIG beneath is then of the density expected, within uncertainty. This top layer which is deficient in Fe has been observed previously in the literature, and confirmed with

---

Table A.1: Parameters for the fits of x-ray reflectivity data for various YIG films shown in fig. A.2, where  $t$  represents the thickness of each layer and densities referred to are electron densities. For the amorphous and etched samples, the top layer consists of YIG whilst for the annealed sample the material is modelled as  $Y_2O_3$ .

Sample	Top Layer $t$ (nm)	Top Layer Density (%)	YIG $t$ (nm)	YIG Density (%)
Amorphous	$1.7 \pm 4$	$120 \pm 20$	$36.1 \pm 0.4$	$92 \pm 2$
Annealed	$1.8 \pm 0.2$	$119 \pm 4$	$34.3 \pm 0.5$	$101 \pm 1$
Etched	$4.2 \pm 0.5$	$95 \pm 5$	$30 \pm 1$	$100 \pm 5$

polarised neutron reflectometry measurements [206].

When these top layers are compared to the magnetotransport data obtained in chapter 6, there is good agreement with this model. The concentration of magnetic ions was found to be least for the annealed sample, which from x-ray reflectivity fits equates to a layer of yttria, and greatest for the amorphous sample, which appears to have a top layer of YIG with  $(120 \pm 20)\%$  the density expected. This agreement between the two datasets gives confidence that these fits are meaningful.

## REFERENCES

- [1] S. D. Bader and S. S. P. Parkin, “Spintronics,” *Annual Review of Condensed Matter Physics*, vol. 1, no. 1, p. 71, 2010.
- [2] C. H. Marrows and B. J. Hickey, “New directions in spintronics,” *Philosophical Transactions of the Royal Society A*, vol. 369, no. 1948, p. 3027, 2011.
- [3] N. Nagaosa, J. Sinova, S. Onoda, A. H. MacDonald, and N. P. Ong, “Anomalous Hall effect,” *Reviews of Modern Physics*, vol. 82, no. 2, p. 1539, 2010.
- [4] A. Hoffmann, “Spin Hall effects in metals,” *IEEE Transactions on Magnetics*, vol. 49, no. 10, p. 5172, 2013.
- [5] T. Jungwirth, J. Wunderlich, and K. Olejnik, “Spin Hall effect devices,” *Nature Materials*, vol. 11, p. 382, 2012.
- [6] A. V. Chumak, V. I. Vasyuchka, A. A. Serga, and B. Hillebrands, “Magnon spintronics,” *Nature Physics*, vol. 11, no. 6, p. 453, 2015.
- [7] M. I. D’yakonov and V. I. Perel, “Possibility of orienting electron spins with current,” *Soviet Physics Journal of Experimental and Theoretical Physics Letters*, vol. 13, no. 11, p. 657, 1971.
- [8] J. E. Hirsch, “Spin Hall effect,” *Physical Review Letters*, vol. 83, no. 9, p. 1834, 1999.
- [9] A. A. Bakun, B. P. Zakharchenya, A. A. Rogachev, M. N. Tkachuk, and V. G. Fleřisher, “Observation of a surface photocurrent caused by optical orientation of electrons in a semiconductor,” *Soviet Physics Journal of Experimental and Theoretical Physics Letters*, vol. 40, no. 11, p. 1293, 1984.

## REFERENCES

---

- [10] Y. Niimi, M. Morota, D. H. Wei, C. Deranlot, M. Basletic, A. Hamzic, A. Fert, and Y. Otani, “Extrinsic spin Hall effect induced by Ir impurities in copper,” *Physical Review Letters*, vol. 106, no. 12, p. 126601, 2011.
- [11] Y. Niimi, Y. Kawanishi, D. H. Wei, C. Deranlot, H. X. Yang, M. Chshiev, T. Valet, A. Fert, and Y. Otani, “Giant spin Hall effect induced by skew scattering from bismuth impurities inside thin film CuBi alloys,” *Physical Review Letters*, vol. 109, no. 15, p. 156602, 2012.
- [12] P. M. Levy, H. Yang, M. Chshiev, and A. Fert, “Spin Hall effect induced by Bi impurities in Cu: skew scattering and side-jump,” *Physical Review B*, vol. 88, no. 21, p. 214432, 2013.
- [13] D. V. Fedorov, C. Herschbach, A. Johnasson, S. Ostanin, I. Mertig, M. Gradhand, K. Chadova, D. Ködderitzsch, and H. Ebert, “Analysis of the giant spin Hall effect in Cu(Bi) alloys,” *Physical Review B*, vol. 88, no. 8, p. 085116, 2013.
- [14] A. Fert and P. M. Levy, “Spin Hall effect induced by resonant scattering on impurities in metals,” *Physical Review Letters*, vol. 106, no. 15, p. 157208, 2011.
- [15] A. Fert and P. M. Levy, “Erratum: Spin Hall effect induced by resonant scattering on impurities in metals,” *Physical Review Letters*, vol. 111, no. 19, p. 199904, 2013.
- [16] C. Herschbach, M. Gradhand, D. V. Fedorov, and I. Mertig, “Enhancement of the spin Hall angle by quantum confinement,” *Physical Review B*, vol. 85, no. 19, p. 195133, 2012.
- [17] H. Nakayama, M. Althammer, Y.-T. Chen, K. Uchida, Y. Kajiwara, D. Kikuchi, T. Ohtani, S. Geprägs, M. Opel, S. Takahashi, R. Gross, G. E. W. Bauer, S. T. B. Goennenwein, and E. Saitoh, “Spin Hall magnetoresistance induced by a nonequilibrium proximity effect,” *Physical Review Letters*, vol. 110, no. 20, p. 206601, 2013.
- [18] M. B. Jungfleisch, V. Lauer, R. Neb, A. V. Chumak, and B. Hillebrands, “Improvement of the yttrium iron garnet/platinum interface for spin pumping-based applications,” *Applied Physics Letters*, vol. 103, no. 2, p. 022411, 2013.

## REFERENCES

---

- [19] C. Burrowes, B. Heinrich, B. Kardasz, E. A. Montoya, E. Girt, Y. Sun, Y.-Y. Song, and M. Wu, “Enhanced spin pumping at yttrium iron garnet/Au interfaces,” *Applied Physics Letters*, vol. 100, no. 9, p. 092403, 2012.
- [20] S. Geprägs, S. Meyer, S. Altmannshofer, M. Opel, F. Wilhelm, A. Rogalev, R. Gross, and S. T. B. Goennenwein, “Investigation of induced Pt magnetic polarization in Pt/Y<sub>3</sub>Fe<sub>5</sub>O<sub>12</sub> bilayers,” *Applied Physics Letters*, vol. 101, no. 26, p. 262407, 2012.
- [21] T. Kikkawa, M. Suzuki, J. Okabayashi, K.-i. Uchida, D. Kikuchi, Z. Qiu, and E. Saitoh, “Detection of induced paramagnetic moments in Pt on Y<sub>3</sub>Fe<sub>5</sub>O<sub>12</sub> via x-ray magnetic circular dichroism,” *Physical Review B*, vol. 95, no. 21, p. 214416, 2017.
- [22] S. Y. Huang, X. Fan, D. Qu, Y. P. Chen, W. G. Wang, J. Wu, T. Y. Chen, J. Q. Xiao, and C. L. Chien, “Transport magnetic proximity effects in platinum,” *Physical Review Letters*, vol. 109, no. 10, p. 107204, 2012.
- [23] B. F. Miao, S. Y. Huang, D. Qu, and C. L. Chien, “Physical origins of the new magnetoresistance in Pt/YIG,” *Physical Review Letters*, vol. 112, no. 23, p. 236601, 2014.
- [24] P. Laczkowski, J.-C. Rojas-Sánchez, W. Savero-Torres, H. Jaffrès, N. Reyren, C. Deranlot, L. Notin, C. Beigné, A. Marty, J.-P. Attané, L. Vila, J.-M. George, and A. Fert, “Experimental evidences of a large extrinsic spin Hall effect in AuW alloy,” *Applied Physics Letters*, vol. 104, no. 14, p. 142403, 2014.
- [25] C. Herschbach, D. V. Fedorov, M. Gradhand, and I. Mertig, “Colossal spin Hall effect in ultrathin metallic films,” *Physical Review B*, vol. 90, no. 18, p. 180406, 2014.
- [26] Y. Niimi, H. Suzuki, Y. Kawanishi, Y. Omori, T. Valet, A. Fert, and Y. Otani, “Extrinsic spin Hall effect measured with lateral spin valve structures,” *Physical Review B*, vol. 89, no. 5, p. 054401, 2014.

## REFERENCES

---

- [27] B. Gu, I. Sugai, T. Ziman, G. Y. Guo, N. Nagaosa, T. Seki, K. Takanashi, and S. Maekawa, "Surface-assisted spin Hall effect in Au films with Pt impurities," *Physical Review Letters*, vol. 105, no. 21, p. 216401, 2010.
- [28] K. Fuchs, "The conductivity of thin metallic films according to the electron theory of metals," *Mathematical Proceedings of the Cambridge Philosophical Society*, vol. 34, no. 1, p. 100, 1938.
- [29] E. H. Sondheimer, "The mean free path of electrons in metals," *Advances in Physics*, vol. 1, no. 1, p. 1, 1952.
- [30] D. Schumacher, "New evidence for the validity of the Fuchs-Sondheimer theory," *Thin Solid Films*, vol. 152, no. 3, p. 499, 1987.
- [31] C. R. Tellier and A. J. Tossier, *Size effects in thin metals films*. Elsevier, 1982.
- [32] J. R. Hook and H. E. Hall, *Solid state physics: second edition*. Wiley, 1991.
- [33] J. S. Dugdale, *The Electrical Properties of Metals and Alloys*. Edward Arnold, 1977.
- [34] S. Dutta, K. Sankaran, K. Moors, G. Pourtis, S. Van Elshocht, J. Bömmels, W. Vandervorst, Z. Tökei, and C. Adelmann, "Thickness dependence of the resistivity of platinum-group metal thin films," *Journal of Applied Physics*, vol. 122, no. 2, p. 025107, 2017.
- [35] C. H. Marrows, *Indirect exchange coupling in sputtered magnetic multilayers*. PhD thesis, Department of Physics & Astronomy, University of Leeds, 1997.
- [36] J. R. Sambles, "The resistivity of thin metal films - some critical remarks," *Thin Solid Films*, vol. 106, no. 4, p. 321, 1983.
- [37] J. M. Ziman, *Electrons and phonons*. Oxford University Press, 1960.
- [38] M. Kohler, "Zur magnetischen widerstandsänderung reiner metalle," *Annalen der Physik*, vol. 424, no. 1, p. 211, 1938.
- [39] E. Koenigsberg, "Conductivity of thin films in a longitudinal magnetic field," *Physical Review*, vol. 91, no. 1, p. 8, 1953.

## REFERENCES

---

- [40] T. R. McGuire and R. I. Potter, "Anisotropic magnetoresistance in ferromagnetic 3d alloys," *IEEE Transactions in Magnetism*, vol. 11, no. 4, p. 1018, 1975.
- [41] J. M. D. Coey, *Magnetism and Magnetic Materials*. Cambridge University Press, 2010.
- [42] J. Smit, "The spontaneous Hall effect in ferromagnetics I," *Physica*, no. 6, p. 877, 1955.
- [43] J. Smit, "The spontaneous Hall effect in ferromagnetics II," *Physica*, vol. 24, no. 1, p. 39, 1958.
- [44] C. Herschbach, D. V. Fedorov, I. Mertig, M. Gradhand, K. Chadova, H. Ebert, and D. Ködderitzsch, "Insight into the skew-scattering mechanism of the spin Hall effect: potential scattering versus spin-orbit scattering," *Physical Review B*, vol. 88, no. 20, p. 205102, 2013.
- [45] D. Yue and X. Jin, "Towards a better understanding of the anomalous Hall effect," *Journal of the Physical Society of Japan*, vol. 86, no. 1, p. 011006, 2017.
- [46] K. M. Seemann, Y. Mokrousov, A. Aziz, J. Miguel, F. Kronast, W. Kuch, M. G. Blamire, A. T. Hindmarch, B. J. Hickey, I. Souza, and C. H. Marrows, "Spin-orbit strength driven crossover between intrinsic and extrinsic mechanisms of the anomalous Hall effect in the epitaxial  $L1_0$ -ordered ferromagnets FePd and FePt," *Physical Review Letters*, vol. 104, no. 7, p. 076402, 2010.
- [47] L. Berger, "Side-jump mechanism for the Hall effect of ferromagnets," *Physical Review B*, vol. 2, no. 11, p. 4559, 1970.
- [48] L. Berger, "Application of the side-jump model to the Hall effect and Nernst effect in ferromagnets," *Physical Review B*, vol. 5, no. 5, p. 1862, 1972.
- [49] A. Fert, A. Friederich, and A. Hamzic, "Hall effect in dilute magnetic alloys," *Journal of Magnetism and Magnetic Materials*, vol. 24, no. 3, p. 231, 1981.
- [50] Y. Tian, L. Ye, and X. Jin, "Proper scaling of the anomalous Hall effect," *Physical Review Letters*, vol. 103, no. 8, p. 087206, 2009.

## REFERENCES

---

- [51] R. J. Elliott, "Theory of the effect of spin-orbit coupling on magnetic resonance in some semiconductors," *Physical Review*, vol. 96, no. 2, p. 266, 1954.
- [52] Y. Yafet, F. Seitz, and D. Turnbull, *Solid State Physics*, vol. 14. New York Academic, 1963.
- [53] M. I. D'yakonov and V. I. Perel, "Spin orientation of electrons associated with the interband absorption of light in semiconductors," *Soviet Physics Journal of Experimental and Theoretical Physics*, vol. 33, no. 5, p. 1053, 1971.
- [54] M. I. D'yakonov and V. I. Perel, "Spin relaxation of conduction electrons in non-centrosymmetric semiconductors," *Soviet Physics Solid State*, vol. 13, no. 12, p. 3023, 1972.
- [55] E. H. Hall, "On a new action of the magnet on electric currents," *American Journal of Mathematics*, vol. 2, no. 3, p. 287, 1879.
- [56] C. L. Chien and C. B. Westgate, *The Hall effect and its applications*. Plenum New York, 1980.
- [57] C. M. Hurd, *The Hall effect in metals and alloys*. Plenum Press, 1972.
- [58] S. Meyer, R. Schlitz, S. Geprägs, M. Opel, H. Huebl, R. Gross, and S. T. B. Goennenwein, "Anomalous Hall effect in YIG|Pt bilayers," *Applied Physics Letters*, vol. 106, no. 13, p. 132402, 2015.
- [59] S. O. Valenzuela and M. Tinkham, "Direct electronic measurement of the spin Hall effect," *Nature*, vol. 442, p. 176, 2006.
- [60] A. B. Pippard, *Magnetoresistance in metals*. Cambridge University Press, 1989.
- [61] J. E. A. Alderson, T. Farrell, and C. M. Hurd, "Significance of Hall-effect measurements in very dilute alloys," *Physical Review B*, vol. 1, no. 10, p. 3904, 1970.
- [62] J. S. Dugdale and L. D. Firth, "The Hall coefficient of dilute alloys of copper and silver," *Journal of Physics C: Solid State Physics*, vol. 2, no. 7, p. 1272, 1969.

## REFERENCES

---

- [63] S. P. McAlister and C. M. Hurd, "Hall effect in 3d-transition metals and alloys," *Journal of Applied Physics*, vol. 50, no. 11, p. 7526, 1979.
- [64] J. E. A. Alderson, T. Farrell, and C. M. Hurd, "Hall coefficients of Cu, Ag, and Au in the range 4.2-300°K," *Physical Review*, vol. 174, no. 3, p. 729, 1968.
- [65] S. P. McAlister, L. R. Lupton, and C. M. Hurd, "Hall and magnetoresistance effects in mictomagnetic AuMn," *Solid State Communications*, vol. 25, no. 11, p. 903, 1978.
- [66] J. E. A. Alderson and C. M. Hurd, "Hall effect and anisotropic relaxation times in  $\alpha$ -phase AgCd, AgIn, AgSn, and AgSb alloys," *Canadian Journal of Physics*, vol. 48, no. 18, p. 2162, 1970.
- [67] P. M. Levy and A. Fert, "Effect of crystal fields on the Hall effect in Kondo-type systems," *Physical Review B*, vol. 39, no. 16, p. 12224, 1989.
- [68] A. Fert and O. Jaoul, "Left-right asymmetry in the scattering of electrons by magnetic impurities, and a Hall effect," *Physical Review Letters*, vol. 28, no. 5, p. 303, 1972.
- [69] M. Trudeau, R. W. Cochrane, D. V. Baxter, J. O. Strom-Olsen, and W. B. Muir, "Positive Hall effect in paramagnetic Zr-Fe," *Physical Review B*, vol. 37, no. 9, p. 4499, 1988.
- [70] E. H. Hall, "On the "rotational coefficient" in nickel and cobalt," *Proceedings of the Physical Society of London*, vol. 4, no. 1, p. 325, 1880.
- [71] E. H. Pugh, "Hall effect and the magnetic properties of some ferromagnetic materials," *Physical Review*, vol. 36, no. 9, p. 1503, 1930.
- [72] E. H. Pugh and T. W. Lippert, "Hall e.m.f. and intensity of magnetization," *Physical Review*, vol. 42, no. 5, p. 709, 1932.
- [73] D. Hou, G. Su, Y. Tian, X. Jin, S. A. Yang, and Q. Niu, "Multivariable scaling for the anomalous Hall effect," *Physical Review Letters*, vol. 114, no. 21, p. 217203, 2015.

## REFERENCES

---

- [74] S. Onoda, N. Sugimoto, and N. Nagaosa, “Intrinsic versus extrinsic anomalous Hall effect in ferromagnets,” *Physical Review Letters*, vol. 97, no. 12, p. 126602, 2006.
- [75] Z. Fang, N. Nagaosa, K. S. Takahashi, A. Asamitsu, R. Mathieu, T. Ogasawara, H. Yamada, M. Kawasaki, Y. Tokura, and K. Terakura, “The anomalous Hall effect and magnetic monopoles in momentum space,” *Science*, vol. 302, no. 5642, p. 92, 2003.
- [76] J. Weischenberg, F. Freimuth, J. Sinova, S. Blügel, and Y. Mokrousov, “Ab initio theory of the scattering-independent anomalous Hall effect,” *Physical Review Letters*, vol. 107, no. 10, p. 106601, 2011.
- [77] R. Karplus and J. M. Luttinger, “Hall effect in ferromagnetics,” *Physical Review*, vol. 95, no. 5, p. 1154, 1954.
- [78] J. M. Luttinger, “Theory of the Hall effect in ferromagnetic substances,” *Physical Review*, vol. 112, no. 3, p. 739, 1958.
- [79] V. T. Volkov, V. I. Levashov, V. N. Matveev, and V. A. Berezin, “Peculiarities of the extraordinary Hall effect of planar arrays Fe nanoparticles embedded in an ultrathin Pt film,” *Applied Physics Letters*, vol. 91, no. 26, p. 262511, 2007.
- [80] A. K. Majumdar and L. Berger, “Hall effect and magnetoresistance in pure iron, lead, Fe-Co, and Fe-Cr dilute alloys,” *Physical Review B*, vol. 7, no. 9, p. 4203, 1973.
- [81] J. E. A. Alderson and C. M. Hurd, “Spin component of the Hall effect and transverse magnetoresistance in dilute alloys containing magnetic solutes,” *Journal of Physics and Chemistry of Solids*, vol. 32, no. 9, p. 2075, 1971.
- [82] B. Zimmermann, K. Chadova, D. Ködderitzsch, S. Blügel, H. Ebert, D. V. Fedorov, N. H. Long, P. Mavropoulos, I. Mertig, Y. Mokrousov, and M. Gradhand, “Skew scattering in dilute ferromagnetic alloys,” *Physical Review B*, vol. 90, no. 22, p. 220403, 2014.

## REFERENCES

---

- [83] K. Tauber, A. Hönemann, D. V. Fedorov, M. Gradhand, and I. Mertig, “Enhancement of the anomalous Hall effect in ternary alloys,” *Physical Review B*, vol. 91, no. 22, p. 220404, 2015.
- [84] F. Töpler, A. Hönemann, K. Tauber, D. V. Fedorov, M. Gradhand, I. Mertig, and A. Fert, “Nonlocal anomalous Hall effect in ternary alloys based on noble metals,” *Physical Review B*, vol. 94, no. 14, p. 140413, 2016.
- [85] Y. M. Lu, J. W. Cai, H. Y. Pan, and L. Sun, “Ultrasensitive anomalous Hall effect in SiO<sub>2</sub>/Fe-Pt/SiO<sub>2</sub> sandwich structure films,” *Applied Physics Letters*, vol. 100, no. 2, p. 022404, 2012.
- [86] S. Shimizu, K. S. Takahashi, T. Hatano, M. Kawasaki, Y. Tokura, and Y. Iwasa, “Electrically tunable anomalous Hall effect in Pt thin films,” *Physical Review Letters*, vol. 111, no. 21, p. 216803, 2013.
- [87] M. T. Béal-Monod and R. A. Weiner, “Negative magnetoresistivity in dilute alloys,” *Physical Review*, vol. 170, no. 2, p. 552, 1968.
- [88] M. T. Béal-Monod and R. A. Weiner, “Field dependence of the anomalous Hall coefficient in dilute magnetic alloys,” *Physical Review B*, vol. 3, no. 9, p. 3056, 1971.
- [89] S. P. McAlister, “The Hall effect in spin glasses,” *Journal of Applied Physics*, vol. 49, no. 3, p. 1616, 1978.
- [90] T. Seki, Y. Hasegawa, S. Mitani, S. Takahashi, H. Immamura, S. Maekawa, J. Nitta, and K. Takanashi, “Giant spin Hall effect in perpendicularly spin-polarized FePt/Au devices,” *Nature Materials*, vol. 7, p. 125, 2008.
- [91] C. Stamm, C. Murer, M. Berritta, J. Feng, M. Gabureac, P. M. Oppeneer, and P. Gambardella, “Magneto-optical detection of the spin Hall effect in Pt and W thin films,” *Physical Review Letters*, vol. 119, no. 8, p. 087203, 2017.
- [92] J. Sinova, D. Culcer, Q. Niu, N. A. Sinitsyn, T. Jungwirth, and A. H. MacDonald, “Universal intrinsic spin Hall effect,” *Physical Review Letters*, vol. 92, no. 12, p. 126603, 2004.

## REFERENCES

---

- [93] G. Y. Guo, S. Murakami, T.-W. Chen, and N. Nagaosa, “Intrinsic spin Hall effect in platinum: first-principles calculations,” *Physical Review Letters*, vol. 100, no. 9, p. 096401, 2008.
- [94] H. Kontani, M. Naito, D. S. Hirashima, K. Yamada, and J.-i. Inoue, “Study of intrinsic spin and orbital Hall effects in Pt based on a ( $6s$ ,  $6p$ ,  $5d$ ) tight-binding model,” *Journal of the Physical Society of Japan*, vol. 76, no. 10, p. 103702, 2007.
- [95] Y. Yao and Z. Fang, “Sign changes of intrinsic spin Hall effect in semiconductors and simple metals: first-principles calculations,” *Physical Review Letters*, vol. 95, no. 15, p. 156601, 2005.
- [96] H. Kontani, T. Tanaka, D. S. Hirashima, K. Yamada, and J. Inoue, “Giant intrinsic spin and orbital Hall effects in  $\text{Sr}_2\text{mO}_4$  ( $m = \text{Ru}, \text{Rh}, \text{Mo}$ ),” *Physical Review Letters*, vol. 100, no. 9, p. 096601, 2008.
- [97] H. Kontani, T. Tanaka, D. S. Hirashima, K. Yamada, and J. Inoue, “Giant orbital Hall effect in transition metals: origin of large spin and anomalous Hall effects,” *Physical Review Letters*, vol. 102, no. 1, p. 016601, 2009.
- [98] J. T. Batley, M. C. Rosamond, M. Ali, E. H. Linfield, G. Burnell, and B. J. Hickey, “Spin relaxation through Kondo scattering in Cu/Py lateral spin valves,” *Physical Review B*, vol. 92, no. 22, p. 220420, 2015.
- [99] A. Friederich, A. Fert, and J. Sierro, “Skew scattering by rare-earth impurities in silver,” *Solid State Communications*, vol. 13, no. 7, p. 997, 1973.
- [100] K. Chadova, D. V. Fedorov, C. Herschbach, M. Gradhand, I. Mertig, D. Ködderitzsch, and H. Ebert, “Separation of the individual contributions to the spin Hall effect in dilute alloys within the first-principles kubo-středa approach,” *Physical Review B*, vol. 92, no. 4, p. 045120, 2015.
- [101] E. Sagasta, Y. Omori, M. Isasa, M. Gradhand, L. E. Hueso, Y. Niimi, Y. Otani, and F. Casanova, “Tuning the spin Hall effect of Pt from the moderately dirty to the superclean regime,” *Physical Review B*, vol. 94, no. 6, p. 060412, 2016.

## REFERENCES

---

- [102] M. Isasa, E. Villamor, L. E. Hueso, M. Gradhand, and F. Casanova, “Temperature dependence of spin diffusion length and spin Hall angle in Au and Pt,” *Physical Review B*, vol. 91, no. 2, p. 024402, 2015.
- [103] M. Isasa, E. Villamor, L. E. Hueso, M. Gradhand, and F. Casanova, “Erratum: Temperature dependence of spin diffusion length and spin Hall angle in Au and Pt,” *Physical Review B*, vol. 92, no. 1, p. 019905, 2016.
- [104] D. T. Dekadjevi, P. A. Ryan, B. J. Hickey, B. D. Fulthorpe, and B. K. Tanner, “Experimental evidence for electron channelling in Fe/Au (100) superlattices,” *Physical Review Letters*, vol. 86, no. 25, p. 5787, 2001.
- [105] A. V. Akimov, S. A. Cavill, A. J. Kent, N. M. Stanton, T. Wang, and S. Sakai, “Phonon emission by photoexcited carriers in InGaN/GaN multiple quantum wells,” *Journal of Physics: Condensed Matter*, vol. 14, no. 13, p. 3445, 2002.
- [106] C. H. Marrows and B. J. Hickey, “Impurity scattering from  $\delta$ -layers in giant magnetoresistance systems,” *Physical Review B*, vol. 63, no. 22, p. 220405, 2001.
- [107] J.-i. Inoue, G. E. W. Bauer, and L. W. Molenkamp, “Suppression of the persistent spin Hall current by defect scattering,” *Physical Review B*, vol. 70, no. 4, p. 041303, 2004.
- [108] Y. Niimi, M. Kimata, Y. Omori, B. Gu, T. Ziman, S. Maekawa, A. Fert, and Y. Otani, “Strong suppression of the spin Hall effect in the spin glass state,” *Physical Review Letters*, vol. 115, no. 19, p. 196602, 2015.
- [109] W. Zhang, M. B. Jungfleisch, W. Jiang, Y. Liu, J. E. Pearson, S. G. E. te Velthuis, A. Hoffmann, F. Freimuth, and Y. Mokrousov, “Reduced spin-Hall effects from magnetic proximity,” *Physical Review B*, vol. 91, no. 11, p. 115316, 2015.
- [110] S. R. Marmion, M. Ali, M. McLaren, D. A. Williams, and B. J. Hickey, “Temperature dependence of spin Hall magnetoresistance in thin YIG/Pt films,” *Physical Review B*, vol. 89, no. 22, p. 220404, 2014.

## REFERENCES

---

- [111] O. d'Allivy Kelly, A. Anane, R. Bernard, J. Ben Youssef, C. Hahn, A. H. Molpeceres, C. Carrétéro, E. Jacquet, C. Deranlot, P. Bortolotti, R. Lebourgeois, J.-C. Mage, G. de Loubens, O. Klein, V. Cros, and A. Fert, "Inverse spin Hall effect in nanometer-thick yttrium iron garnet/Pt system," *Applied Physics Letters*, vol. 103, no. 8, p. 082408, 2013.
- [112] Y. Shiomi, T. Ohtani, S. Iguchi, T. Sasaki, Z. Qiu, H. Nakayama, K. Uchida, and E. Saitoh, "Interface-dependent magnetotransport properties for thin Pt films on ferrimagnetic  $Y_3Fe_5O_{12}$ ," *Applied Physics Letters*, vol. 104, no. 24, p. 242406, 2014.
- [113] Y.-T. Chen, S. Takahashi, H. Nakayama, M. Althammer, S. T. B. Goennenwein, E. Saitoh, and G. E. W. Bauer, "Theory of spin Hall magnetoresistance," *Physical Review B*, vol. 87, no. 14, p. 144411, 2013.
- [114] C. Hahn, G. de Loubens, O. Klein, M. Viret, V. V. Naletov, and J. Ben Youssef, "Comparative measurements of inverse spin Hall effects and magnetoresistance in YIG/Pt and YIG/Ta," *Physical Review B*, vol. 87, no. 17, p. 174417, 2013.
- [115] S. Wang, L. Zou, X. Zhang, J. Cai, S. Wang, B. Shen, and J. Sun, "Spin Seebeck effect and spin Hall magnetoresistance at high temperatures for a Pt/yttrium iron garnet hybrid structure," *Nanoscale*, vol. 7, no. 42, p. 17812, 2015.
- [116] T. Shang, Q. F. Zhan, L. Ma, H. L. Yang, Z. H. Zuo, Y. L. Xie, H. H. Li, L. P. Liu, B. M. Wang, Y. H. Wu, S. Zhang, and R.-W. Li, "Pure spin-Hall magnetoresistance in Rh/ $Y_3Fe_5O_{12}$  hybrid," *Scientific Reports*, vol. 5, p. 17734, 2015.
- [117] X. Zhang and L. K. Zou, "Planar Hall effect in  $Y_3Fe_5O_{12}$ /IrMn films," *Applied Physics Letters*, vol. 105, no. 26, p. 262401, 2014.
- [118] T. Lin, C. Tang, H. M. Alyahyaei, and J. Shi, "Experimental investigation of the nature of the magnetoresistance effects in Pd-YIG hybrid structures," *Physical Review Letters*, vol. 113, no. 3, p. 037203, 2014.

## REFERENCES

---

- [119] H. Wang, D. Hou, Z. Qiu, T. Kikkawa, E. Saitoh, and X. Jin, “Antiferromagnetic anisotropy determination by spin Hall magnetoresistance,” *Journal of Applied Physics*, vol. 122, no. 8, p. 083907, 2017.
- [120] M. Kaveh and N. Wiser, “Electron-electron scattering in conducting materials,” *Advances in Physics*, vol. 33, no. 4, p. 257, 1984.
- [121] G. Bergmann, “Physical interpretation of weak localization: a time-of-flight experiment with conduction electrons,” *Physical Review B*, vol. 28, no. 6, p. 2914, 1983.
- [122] G. Bergmann, “Consistent temperature and field dependence in weak localization,” *Physical Review B*, vol. 28, no. 2, p. 515, 1983.
- [123] G. Bergmann, “Weak localization in thin films: a time-of-flight experiment with conduction electrons,” *Physics Reports*, vol. 107, no. 1, p. 1, 1984.
- [124] E. Abrahams, P. W. Anderson, D. C. Licciardello, and T. V. Ramakrishnan, “Scaling theory of localization: absence of quantum diffusion in two dimensions,” *Physical Review Letters*, vol. 42, no. 10, p. 673, 1979.
- [125] B. L. Altshuler, D. Khmel’nitzkii, and A. I. Larkin, “Magnetoresistance and Hall effect in a disordered two-dimensional electron gas,” *Physical Review B*, vol. 22, no. 11, p. 5142, 1980.
- [126] S. Hikami, A. I. Larkin, and Y. Nagaoka, “Spin-orbit interaction and magnetoresistance in the two dimensional random system,” *Progress of Theoretical Physics*, vol. 63, no. 2, p. 707, 1980.
- [127] P. W. Anderson, E. Abrahams, and T. V. Ramakrishnan, “Possible explanation of nonlinear conductivity in thin-film metal wires,” *Physical Review Letters*, vol. 43, no. 10, p. 718, 1979.
- [128] L. P. Gor’kov, A. I. Larkin, and D. E. Khmel’nitskii, “Particle conductivity in a two-dimensional random potential,” *Soviet Physics Journal of Experimental and Theoretical Physics Letters*, vol. 30, no. 4, p. 228, 1979.

## REFERENCES

---

- [129] S. Maekawa and H. Fukuyama, “Magnetoresistance in two-dimensional disordered systems: effects of Zeeman splitting and spin-orbit scattering,” *Journal of the Physical Society of Japan*, vol. 50, no. 8, p. 2516, 1981.
- [130] D. Abraham and R. Rosenbaum, “Localization in thin copper films,” *Physical Review B*, vol. 27, no. 2, p. 1409, 1983.
- [131] B. L. Altshuler, A. G. Aronov, and P. A. Lee, “Interaction effects in disordered Fermi systems in two dimensions,” *Physical Review Letters*, vol. 44, no. 19, p. 1288, 1980.
- [132] A. C. Sacharoff and R. M. Westervelt, “Localization and interaction effects in thin titanium films,” *Physical Review B*, vol. 32, no. 2, p. 662, 1985.
- [133] E. Abrahams, P. W. Anderson, P. A. Lee, and T. V. Ramakrishnan, “Quasiparticle lifetime in disordered two-dimensional metals,” *Physical Review B*, vol. 24, no. 12, p. 6783, 1981.
- [134] L. Landau, I. Pomeranchuk, and D. Ter Haar, *Collected papers of L. D. Landau*. Pergamon Press, 1965.
- [135] J. T. Masden and N. Giordano, “Localization and electron-electron interaction effects in thin Pt wires,” *Physical Review B*, vol. 31, no. 10, p. 6395, 1985.
- [136] J. J. Lin and N. Giordano, “Electron scattering times from weak localization studies of Au-Pd films,” *Physical Review B*, vol. 35, no. 3, p. 1071, 1987.
- [137] P. A. Lee and T. V. Ramakrishnan, “Magnetoresistance of weakly disordered electrons,” *Physical Review B*, vol. 26, no. 8, p. 4009, 1982.
- [138] P. Mitra, R. Misra, A. F. Hebard, K. A. Muttalib, and P. Wölfle, “Weak-localization correction to the anomalous Hall effect in polycrystalline Fe films,” *Physical Review Letters*, vol. 99, no. 4, p. 046804, 2007.
- [139] X. Zhang, W. Wang, K. Wang, W. Niu, B. Lai, N. Maltby, M. Yang, M. Gao, W. Liu, L. He, R. Zhang, and Y. Xu, “Universal scaling of the anomalous Hall effect,” *Journal of Physics D: Applied Physics*, vol. 50, no. 15, p. 155002, 2017.

## REFERENCES

---

- [140] H. Fukuyama, "Hall effect in two-dimensional disordered systems," *Journal of the Physical Society of Japan*, vol. 49, no. 10, p. 644, 1980.
- [141] J. Crangle, "Ferromagnetism in Pd-rich palladium-iron alloys," *The Philosophical Magazine: A Journal of Theoretical Experimental and Applied Physics*, vol. 5, no. 52, p. 335, 1960.
- [142] J. J. Hauser, "Magnetic proximity effect," *Physical Review*, vol. 187, no. 2, p. 580, 1969.
- [143] F. Wilhelm, P. Poupoulos, G. Ceballos, H. Wende, K. Baberschke, P. Srivastava, D. Benes, H. Ebert, M. Angelakeris, N. K. Flevaris, D. Niarchos, A. Rogalev, and N. B. Brookes, "Layer-resolved magnetic moments in Ni/Pt multilayers," *Physical Review Letters*, vol. 85, no. 2, p. 413, 2000.
- [144] E. C. Stoner, "Collective electron ferromagnetism," *Proceedings of the Royal Society of London Series A, Mathematical and Physical Sciences*, vol. 165, no. 922, p. 372, 1938.
- [145] E. C. Stoner, "Collective electron ferromagnetism II. Energy and specific heat," *Proceedings of the Royal Society of London Series A, Mathematical and Physical Sciences*, vol. 169, no. 938, p. 339, 1939.
- [146] J. Kondo, "Resistance minimum in dilute magnetic alloys," *Progress of Theoretical Physics*, vol. 32, no. 1, p. 37, 1964.
- [147] J. Kondo, *The Physics of Dilute Magnetic Alloys*. Cambridge University Press, 2012.
- [148] N. W. Ashcroft and N. D. Mermin, *Solid state physics*. Brooks/Cole, 1976.
- [149] P. W. Anderson, "Localized magnetic states in metals," *Physical Review*, vol. 124, no. 1, p. 41, 1961.
- [150] C. Kittel, *Introduction to Solid State Physics, Seventh Edition*. John Wiley and Sons, 1996.

## REFERENCES

---

- [151] J. S. Loomis and W. R. Hudson, “Low-temperature resistance minimum and magnetoresistance for dilute alloys of iron in copper,” *NASA Technical Note*, vol. TN, pp. D-4626, 1968.
- [152] D. Goldhaber-Gordon, J. Göres, M. A. Kastner, H. Shtrikman, D. Mahalu, and U. Meirav, “From the Kondo regime to the mixed-valence regime in a single-electron transistor,” *Physical Review Letters*, vol. 81, no. 23, p. 5225, 1998.
- [153] L. O’Brien, M. J. Erickson, D. Spivak, H. Ambaye, R. J. Goyette, V. Lauter, P. A. Crowell, and C. Leighton, “Kondo physics in non-local metallic spin transport devices,” *Nature Communications*, vol. 5, p. 3927, 2014.
- [154] T. Gang, M. Deniz Yilmaz, D. Ata, S. K. Bose, E. Strambini, A. H. Velders, M. P. de Jong, J. Huskens, and W. G. van der Wiel, “Tunable doping of a metal with molecular spins,” *Nature Nanotechnology*, vol. 7, no. 4, p. 232, 2012.
- [155] T. A. Costi, A. C. Hewson, and V. Zlatić, “Transport coefficients of the Anderson model via the numerical renormalization group,” *Journal of Physics Condensed Matter*, vol. 6, no. 13, pp. 2519–2558, 1994.
- [156] C. Bäuerle, F. m. c. Mallet, F. Schopfer, D. Mailly, G. Eska, and L. Saminadayar, “Experimental test of the numerical renormalization-group theory for inelastic scattering from magnetic impurities,” *Physical Review Letters*, vol. 95, no. 26, p. 266805, 2005.
- [157] F. Mallet, J. Ericsson, D. Mailly, S. Ünlübayir, D. Reuter, A. Melnikov, A. D. Wieck, T. Micklitz, A. Rosch, T. A. Costi, L. Saminadayar, and C. Bäuerle, “Scaling of the low-temperature dephasing rate in Kondo systems,” *Physical Review Letters*, vol. 97, no. 22, p. 226804, 2006.
- [158] B. R. Coles, “Low-temperature resistivity behaviour of molybdenum-iron, niobium-iron and palladium-iron alloys,” *Philosophical Magazine*, vol. 8, no. 86, p. 335, 1963.
- [159] J. W. Loram, R. J. White, and A. D. C. Grassie, “Spin-fluctuation effects in the resistivity of dilute PtFe alloys,” *Physical Review B*, vol. 5, no. 9, p. 3659, 1972.

## REFERENCES

---

- [160] M. Althammer, S. Meyer, H. Nakayama, M. Schreier, S. Altmannshofer, M. Weiler, H. Huebl, S. Geprägs, M. Opel, R. Gross, D. Meier, C. Kiewe, T. Kuschel, J.-M. Schmalhorst, G. Reiss, L. Shen, A. Gupta, Y.-T. Chen, G. E. W. Bauer, E. Saitoh, and S. T. B. Goennenwein, “Quantitative study of the spin Hall magnetoresistance in ferromagnetic insulator/normal metal hybrids,” *Physical Review B*, vol. 87, no. 22, p. 224401, 2013.
- [161] S. R. Marmion, *Comparison of Spin Hall Magnetoresistance Temperature Dependence in YIG/Metal Systems*. PhD thesis, School of Physics & Astronomy, University of Leeds, 2016.
- [162] S. Vélez, A. Bedoya-Pinto, W. Yan, L. E. Hueso, and F. Casanova, “Competing effects at Pt/YIG interfaces: spin Hall magnetoresistance, magnon excitations, and magnetic frustration,” *Physical Review B*, vol. 94, no. 17, p. 174405, 2016.
- [163] Y. M. Lu, Y. Choi, C. M. Ortega, X. M. Cheng, J. W. Cai, S. Y. Huang, L. SUn, and C. L. Chien, “Pt magnetic polarization on  $Y_3Fe_5O_{12}$  and magnetotransport characteristics,” *Physical Review Letters*, vol. 110, no. 14, p. 147207, 2013.
- [164] Y. Yang, B. Wu, K. Yao, S. Shannigrahi, B. Zong, and Y. Wu, “Investigation of magnetic proximity effect in Ta/YIG bilayer Hall bar structure,” *Journal of Applied Physics*, vol. 115, no. 17, p. 17C509, 2014.
- [165] A. Mitra, O. Cespedes, Q. Ramasse, M. Ali, S. Marmion, M. Ward, R. M. D. Brydson, C. J. Kinane, J. F. K. Cooper, S. Langridge, and B. J. Hickey, “Interfacial origin of the magnetisation suppression of thin film yttrium iron garnet,” *Scientific Reports*, vol. 7, p. 11774, 2017.
- [166] A. Mitra, *Structural and magnetic properties of YIG thin films and interfacial origin of magnetisation suppression*. PhD thesis, School of Physics & Astronomy, University of Leeds, 2017.
- [167] H. Arend and J. Hulliger, *Crystal Growth in Science and Technology*. Springer US, 2012.
- [168] M. Alyami, M. Ali, and B. J. Hickey, “The formation of non-stoichiometric yig at the yag/yig interface.” unpublished work, 2017.

## REFERENCES

---

- [169] J. Als-Nielsen and D. McMorrow, *Elements of modern x-ray physics*. Wiley, 2001.
- [170] M. M. Woolfson, *An introduction to x-ray crystallography*. Cambridge University Press, 1997.
- [171] N. Stribeck, *X-ray scattering of soft matter*. Springer, 2007.
- [172] W. H. Bragg and W. L. Bragg, “The reflection of x-rays by crystals,” *Proceedings of the Royal Society A*, vol. 88, no. 605, p. 428, 1913.
- [173] W. L. Bragg, “The analysis of crystals by the x-ray spectrometer,” *Proceedings of the Royal Society A*, vol. 89, no. 613, p. 468, 1914.
- [174] P. Scherrer, “Bestimmung der grosse und der inneren struktur von kolloidteilchen mittels rontgenstrahlen,” *Nachrichten von der Gesellschaft der Wissenschaften, Gottingen*, vol. 2, p. 98, 1918.
- [175] A. L. Patterson, “The Scherrer formula for x-ray particle size determination,” *Physical Review*, vol. 56, no. 10, p. 978, 1939.
- [176] P. F. Fewster, “X-ray analysis of thin films and multilayers,” *Reports on Progress of Physics*, vol. 96, p. 1339, 1996.
- [177] T. Tanaka, H. Kontani, M. Naito, T. Naito, D. S. Hirashima, K. Yamada, and J. Inoue, “Intrinsic spin Hall effect and orbital Hall effect in 4d and 5d transition metals,” *Physical Review B*, vol. 77, no. 16, p. 165117, 2008.
- [178] J. Rumble, ed., *CRC Handbook of Chemistry and Physics*. Taylor & Francis Ltd., 2019.
- [179] C. Yue, X.-J. Weng, G. Gao, A. R. Oganov, X. Dong, X. Shao, X. Wang, J. Sun, B. Xu, H.-T. Wang, X.-F. Zhou, and Y. Tian, “Formation of copper boride on Cu(111),” *Fundamental Research*, vol. 10, no. 4, p. 1016, 2021.
- [180] G. A. Swallow, G. Williams, A. D. C. Grassie, and J. W. Loram, “Magnetoresistance of a dilute PtFe alloy,” *Journal of Physics F: Metal Physics*, vol. 1, p. 511, 1971.

## REFERENCES

---

- [181] Y. M. Lu, J. W. Cai, S. Y. Huang, D. Qu, B. F. Miao, and C. L. Chien, “Hybrid magnetoresistance in the proximity of a ferromagnet,” *Physical Review B*, vol. 87, no. 22, p. 220409, 2013.
- [182] G. Fischer, H. Hoffmann, and J. Vancea, “Mean free path and density of conductance electrons in platinum determined by the size effect in extremely thin films,” *Physical Review B*, vol. 22, no. 12, p. 6065, 1980.
- [183] G. S. Knapp, “Phenomenological theory of the resistivity and susceptibility of dilute Rh-Fe and Ir-Fe alloys,” *Physics Letters*, vol. 25A, no. 2, p. 114, 1967.
- [184] J. S. Agustsson, U. B. Arnalds, A. S. Ingason, K. B. Gylfason, K. Johnsen, S. Olafsson, and J. T. Gudmundsson, “Electrical resistivity and morphology of ultra thin Pt films grown by dc magnetron sputtering on SiO<sub>2</sub>,” *Journal of Physics: Conference Series*, vol. 100, no. 8, p. 082006, 2008.
- [185] J. Adams, G. Stefanou, M. Ali, and B. J. Hickey, “The Kondo effect in thin film of Ag.” unpublished work, 2019.
- [186] W. Zhang, V. Vlaminck, J. E. Pearson, R. Divan, S. D. Bader, and A. Hoffmann, “Determination of the Pt spin diffusion length by spin-pumping and spin Hall effect,” *Applied Physics Letters*, vol. 103, no. 24, p. 242414, 2013.
- [187] H. B. Peacock, “Hall effect in evaporated films of iron, cobalt, nickel, palladium, and platinum,” *Physical Review*, vol. 27, no. 4, p. 474, 1926.
- [188] V. Frank, “Hall coefficient of technically pure metals from 80 °K to 800 °K,” *Applied Scientific Research, Section B*, vol. 6, no. 1, p. 379, 1957.
- [189] O. A. Panchenko, P. P. Lutsishin, and Y. G. Ptushinskii, “Galvanomagnetic effects in thin films of some transition metals,” *Soviet Physics Journal of Experimental and Theoretical Physics*, vol. 29, no. 1, p. 76, 1969.
- [190] R. Wang, D. Guo, G. Xie, and G. Pan, “Atomic step formation on sapphiric surface in ultra-precision manufacturing,” *Scientific Reports*, vol. 6, p. 29964, 2016.

## REFERENCES

---

- [191] N. Giordano, “Magnetoresistance of small Kondo systems,” *Physical Review B*, vol. 53, no. 5, p. 2487, 1996.
- [192] W.-L. Lee, S. Watauchi, V. L. Miller, R. J. Cava, and N. P. Ong, “Dissipationless anomalous Hall current in the ferromagnetic spinel  $\text{CuCr}_2\text{Se}_{4-x}\text{Br}_x$ ,” *Science*, vol. 303, no. 5664, p. 1647, 2004.
- [193] K. S. Takahashi, M. Onoda, M. Kawasaki, N. Nagaosa, and Y. Tokura, “Control of the anomalous Hall effect by doping in  $\text{Eu}_{1-x}\text{La}_x\text{TiO}_3$  thin films,” *Physical Review Letters*, vol. 103, no. 5, p. 057204, 2009.
- [194] T. Golod, A. Rydh, P. Svendlindh, and V. M. Krasnov, “Anti-ordinary Hall effect near the ferromagnetic quantum phase transition in  $\text{Ni}_x\text{Pt}_{1-x}$  thin films,” *Physical Review B*, vol. 87, no. 10, p. 104407, 2013.
- [195] A. Talalaevskij, M. Decker, J. Stigloher, A. Mitra, H. S. Koner, O. Cespedes, C. H. Back, and B. J. Hickey, “Magnetic properties of spin waves in thin yttrium iron garnet films,” *Physical Review B*, vol. 95, no. 6, p. 064409, 2017.
- [196] Z. Fang, A. Mitra, A. L. Westerman, M. Ali, C. Ciccarelli, O. Cespedes, B. J. Hickey, and A. J. Ferguson, “Thickness dependence study of current-driven ferromagnetic resonance in  $\text{Y}_3\text{Fe}_5\text{O}_{12}$ /heavy metal bilayers,” *Applied Physics Letters*, vol. 110, no. 9, p. 092403, 2017.
- [197] L. Dobrzycki, E. Bulska, D. A. Pawlak, Z. Frukacz, and K. Woźniak, “Structure of YAG crystals doped/substituted with Erbium and Ytterbium,” *Inorganic Chemistry*, vol. 43, no. 24, p. 7656, 2004.
- [198] S. Geller and M. A. Gilleo, “The crystal structure and ferrimagnetism of yttrium-iron garnet  $\text{Y}_3\text{Fe}_2(\text{FeO}_4)_3$ ,” *Journal of Physics and Chemistry of Solids*, vol. 3, no. 1, p. 30, 1957.
- [199] H. Wang, C. Du, C. Hammel, and F. Yang, “Strain-tunable magnetocrystalline anisotropy in epitaxial  $\text{Y}_3\text{Fe}_5\text{O}_{12}$  thin films,” *Physical Review B*, vol. 89, no. 13, p. 134404, 2014.

## REFERENCES

---

- [200] M. Alyami, M. Ali, and B. J. Hickey, “X-ray diffraction of high quality thick YIG films.” unpublished work, 2017.
- [201] X. Liang, Y. Zhu, B. Peng, L. Deng, J. Xie, H. Lu, M. Wu, and L. Bi, “Influence of interface structure on magnetic proximity effect in Pt/Y<sub>3</sub>Fe<sub>5</sub>O<sub>12</sub> heterostructures,” *Applied Materials and Interfaces*, vol. 8, no. 12, p. 8175, 2016.
- [202] Y. Niimi, D. Wei, H. Idzuchi, T. Wakamura, T. Kato, and Y. Otani, “Experimental verification of comparability between spin-orbit and spin-diffusion lengths,” *Physical Review Letters*, vol. 110, no. 1, p. 016805, 2013.
- [203] D. Wesenberg, T. Liu, D. Balzar, M. Wu, and B. L. Zink, “Long-distance spin transport in a disordered magnetic insulator,” *Nature Physics*, vol. 13, p. 987, 2017.
- [204] O. H. Seeck and B. Murphy, *X-ray diffraction*. Pan Stanford, 2015.
- [205] M. Björck and G. Andersson, “GenX: an extensible x-ray reflectivity refinement program utilizing differential evolution,” *Journal of Applied Crystallography*, vol. 40, no. 6, p. 1174, 2007.
- [206] J. F. K. Cooper, C. J. Kinane, S. Langridge, M. Ali, B. J. Hickey, T. Niizeki, K. Uchida, E. Saitoh, H. Ambaye, and A. Glavic, “Unexpected structural and magnetic depth dependence of YIG thin films,” *Physical Review B*, vol. 96, no. 10, p. 104404, 2017.